



HAL
open science

The equation of state of the Hydrogen-Helium mixture with application to the Sun

David Wendland

► **To cite this version:**

David Wendland. The equation of state of the Hydrogen-Helium mixture with application to the Sun. Astrophysics [astro-ph]. Ecole normale supérieure de lyon - ENS LYON, 2015. English. NNT : 2015ENSL1029 . tel-01237839

HAL Id: tel-01237839

<https://theses.hal.science/tel-01237839v1>

Submitted on 3 Dec 2015

HAL is a multi-disciplinary open access archive for the deposit and dissemination of scientific research documents, whether they are published or not. The documents may come from teaching and research institutions in France or abroad, or from public or private research centers.

L'archive ouverte pluridisciplinaire **HAL**, est destinée au dépôt et à la diffusion de documents scientifiques de niveau recherche, publiés ou non, émanant des établissements d'enseignement et de recherche français ou étrangers, des laboratoires publics ou privés.



THÈSE

en vue de l'obtention du grade de

Docteur de l'Université de Lyon,
délivré par l'École Normale Supérieure de Lyon

Discipline : PHYSIQUE

Laboratoire de Physique de l'ENS de LYON
Institut UTINAM de l'Université de Franche-Comté BESANÇON

École Doctorale de Physique et d'Astrophysique de Lyon

The equation of state of the Hydrogen-Helium mixture with application to the Sun

L'équation d'état du mélange Hydrogène-Hélium avec application au Soleil

par

David Robert Wendland

Directeur de thèse : M. Angel ALASTUEY
Codirecteur de thèse : M. Vincent BALLENEGGER

Présentée et soutenue publiquement le 30 octobre 2015

Après avis de: M. Bernard BERNU Rapporteur
M. Emmanuel TRIZAC Rapporteur

Devant la commission d'examen formée de:

M. Gilles CHABRIER	Président du jury
M. Peter HOLDSWORTH	Membre du jury
M. Sylvain PICAUD	Membre du jury
M. Angel ALASTUEY	Directeur de thèse
M. Vincent BALLENEGGER	Codirecteur de thèse

Contents

1	Introduction	9
2	Review: The partially recombined plasma	15
3	The loop representation and quantum Mayer diagrams	21
3.1	Introduction	21
3.2	The loop representation	22
3.3	Bare quantum Mayer diagrams	24
3.3.1	Symmetry factors and topological structure of the Mayer diagrams	27
3.3.2	From pressure to density	28
3.4	Screened quantum Mayer Diagrams	28
3.4.1	Resummed Mayer diagrams	29
3.4.2	The screened loop-loop potential	33
3.5	Neutrality and the truncated fugacity series	35
3.6	Definition of the κ dependent cluster functions	37
4	Physical implications of the screened potential	41
4.1	Physical effects of the resummation	41
4.2	Numerical calculation of the resummed potential	44
5	Numerical computation of the Cluster-functions	49
5.1	Introduction	49
5.2	A few reminders concerning Monte-Carlo integration	50
5.2.1	Importance sampling	52
5.2.2	The Metropolis-Hastings algorithm	52
5.3	Calculation of cluster functions in vacuum: overview of the article	53
5.3.1	The Importance sampling of the paths	54
5.3.2	Adaptive discretization of path integrals	56
5.3.3	Results	60
5.4	κ -dependent Cluster functions	61
5.4.1	Neutral cluster functions: H and He	62
5.4.2	Charged cluster functions	63
5.4.3	Exchange functions	66

6	Thermodynamics of pure hydrogen at low densities and low temperatures	69
6.1	Scaled-low-temperature limit	69
6.1.1	The Saha-equation	70
6.1.2	The SLT-limit and corrections to the Saha-equation	70
6.1.3	Truncation of Cluster due to screening	71
6.2	Application of the SLT-expansion to the solar adiabat	73
6.3	A simple approximation inspired by the SLT-expansion	76
6.4	Conclusions	78
7	Equation of State of the Hydrogen-Helium Mixture	81
7.1	The implementation of the fugacity expansion	82
7.2	The selection of diagrams	83
7.3	The equation of state of the pure Hydrogen system	85
7.4	The equation of state of the Hydrogen-Helium mixture	88
7.4.1	General considerations	88
7.4.2	The Hydrogen-Helium model with three-body interactions	90
7.4.3	The reduced Hydrogen-Helium model	91
7.4.4	Results	91
7.4.5	Contribution of He^+ ions to screening	93
7.5	Conclusion	98
8	Conclusions	99

Acknowledgements





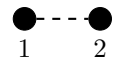
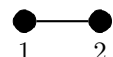
During the time I was working on this thesis I met gentle people and encountered a welcoming environment in both of my laboratories. The working atmosphere was very stimulating not only due to the devotion of my two supervisors, Angel Alastuey and Vincent Ballenegger, but also due to the culture in both institutions. I, therefore, thank both of them for giving me the opportunity to accomplish this work, which they made possible at first. Their efforts were a basic ingredient for the progress I made during the work on this thesis.

I owe a debt of gratitude to the plethora of colleagues where I have to mention especially: Jean-Baptiste Caussin, Julian Bernaud, Timothée Verdier, Joost Weijs, Robin Guichardaz, Maxime Champion, Guillaume Rollin, Timothée Accadia and Ali Dib Mohamad. Furthermore I would like to thank my close friends Tatjana Stoll, Wojtek Kulczycki, Daniel Neumer, Kristijan Sikiric, Felix Mees, Martin Pander, Stefan Mutschke, Jean Sterlin, Jonas Lien and Adrian Petit for their unconditional support and the good time we had and still have together. During my time in Lyon I became an active member of the local university water polo team. I really enjoyed the time with my team not only during the weekly training session but also outside of the water.

Last but not least, it is only due to my family who created the circumstances for me to pursue my interests during my hole life, that this thesis could have been written. I am particularly indebted to my mother for her comprehensive proofreading, which helped me immensely during the writing.

Nomenclature

$\{x_i\}$	Configuration of the x_i , $\{x_i\} = \{x_1, x_2, x_3, \dots, x_n\}$
α	Parameter characterizing the Helium fraction in the Hydrogen-Helium plasma $\alpha = \frac{\rho_\alpha}{\rho_\alpha + \rho_p}$
β	Inverse temperature $\beta = 1/k_B T$
ρ	Total number density
γ	Generally used for an unspecified particle species
c	Speed of sound
N_γ	Particle number of species γ
ρ_γ	Number density of species γ
μ_γ	Chemical potential of species γ
z_γ	Fugacity $z_\gamma = e^{\beta\mu_\gamma}$ of species γ
$z(\mathcal{L})$	Fugacity of a loop (defined in equation (3.14) on page 24)
\tilde{z}_γ	$\tilde{z}_\gamma = \frac{(2\sigma_\gamma + 1)z_\gamma}{(2\pi\lambda_\gamma^2)^{3/2}}$
e_γ	Charge of species γ
m_γ	Mass of species γ
λ_γ	Thermal wavelength of species γ
κ	Debye screening constant
ξ	Shape of a one-particle path
σ	Spin
\mathcal{L}	Loop, a loop contains a specific number of particles (with common spin) and has loop shape η
η	Shape of a loop
q	Number of particles forming a loop
$\mathcal{D}(\mathcal{L})$	Measure of functional integration of loops
$f(\cdot, \cdot)$	The Mayer bond
P	The pressure (throughout this thesis give expressions for βP measured in atomic units a_0^{-3})
a_0	The Bohr radius
S	Symmetry factor of a diagram
Z	Partition function
$C_{\{\gamma\}}$	Cluster function of a certain configuration of particle species

\mathcal{F}	Free energy functional
F	Thermodynamic free energy
Ω	Grand canonical potential
Ξ	Grand canonical partition function
$\delta(s_1, s_2)$	Delta-function
δ_{s_1, s_2}	Kronecker-Delta
$\tilde{\delta}(s_1, s_2)$	Dirac-comb $\tilde{\delta}(s_1, s_2) = \sum_{i=-\infty}^{\infty} \delta(s_1 - s_2 + i)$
V	Coulomb potential
●	Node with fugacity factor z
⊙	Node with fugacity factor $z (e^{IR} - 1)$
○	Node for which no summation over inner degrees of freedom is carried out. This node occurs when the derivative $z_\gamma \frac{\partial}{\partial z_\gamma}$ acts on a black node.
●	Node to be superposed with other gray nodes and blackened after diagram is constructed
	Coulomb interaction of loops $-\beta V(\mathcal{L}_1, \mathcal{L}_2)$
	Screened interaction of loops $-\beta \phi(\mathcal{L}_1, \mathcal{L}_2)$
	$e^{-\beta \phi(\mathcal{L}_1, \mathcal{L}_2)} - 1 + \beta \phi(\mathcal{L}_1, \mathcal{L}_2)$
	$e^{-\beta \phi(\mathcal{L}_1, \mathcal{L}_2)} - 1 + \beta \phi(\mathcal{L}_1, \mathcal{L}_2) - \frac{(\beta \phi(\mathcal{L}_1, \mathcal{L}_2))^2}{2}$
	$\frac{1}{2} \int \mathcal{D}(\mathcal{L}_2) \phi(\mathcal{L}_1, \mathcal{L}_2) V(\mathcal{L}_2, \mathcal{L}_1) z(\mathcal{L}_2)$
	$e^{-\beta V(\mathcal{L}_1, \mathcal{L}_2)} - 1$

Chapter 1

Introduction

Since the earliest times in human history, men were fascinated by the stars lighting up the nightly sky. The understanding of these objects was out of reach for most of our ancestors, so that for centuries astronomical objects were mystified and venerated. The rise of modern physics was primarily initiated by mankind's understanding of the motion of the planets, which led also philosophically to a change of paradigm. The relation of physics and astronomy was eventually clarified by Newton [1], who used mathematical equations to describe his famous laws. A very important insight was that the same physical laws that govern very large distant objects such as stars and planets, are also responsible for the motion of objects on our scale, such as apples falling from a tree.

In modern physics the astronomical observations have been of immense importance not only for the understanding of “their” physics, but they also open the possibility to verify our current physical models in different domains. A prominent example is, of course, the verification of Einstein's theory of general relativity from the observation of bended trajectories of light rays in the presence of large mass concentrations [2].

Astronomical observations, especially those of our nearest star, the Sun, have ever since stimulated development and the understanding of our theoretical models. In recent years, for example, the so-called solar neutrino problem led to an important controversy among scientist and its resolution had even impact on the “Standard Model” of particle physics. At the time, observation of neutrino particles stemming from the Sun, where they are created by fusion were incompatible with contemporary solar models, in particular concerning the core temperature [3]. Helioseismic observations, on the other hand, confirmed the standard solar models. The discrepancy between “direct” observation of the core temperature and the indirect prediction interfered from helioseismic observation of the surface of the Sun, led finally to the conclusion that the neutrinos are not massless, unlike assumed before¹. The first theoretical hypothesis of the neutrino oscillations was given in Reference [4] and the first experimental evidence dates back to the Super-Kamiokande Experiment (see [5] for a review of its experimental results).

Besides these important fundamental experiments and theoretical developments, astronomical objects are important to study systems at, for human experience, extreme conditions and at the same time ideal conditions, from the physics perspective. Again, the Sun is a prominent example: Its sheer size makes it ideal in the physical sense, but incomprehensible on the level of human length scales. The large scale differences of atomic, gravitational and dynamical length scales make it possible to consider each volume element of the Sun to be in thermodynamic equilibrium in a very good approximation. Its composition

¹Even more important the flavor eigenstates of the neutrinos are not equal to the mass eigenstates.

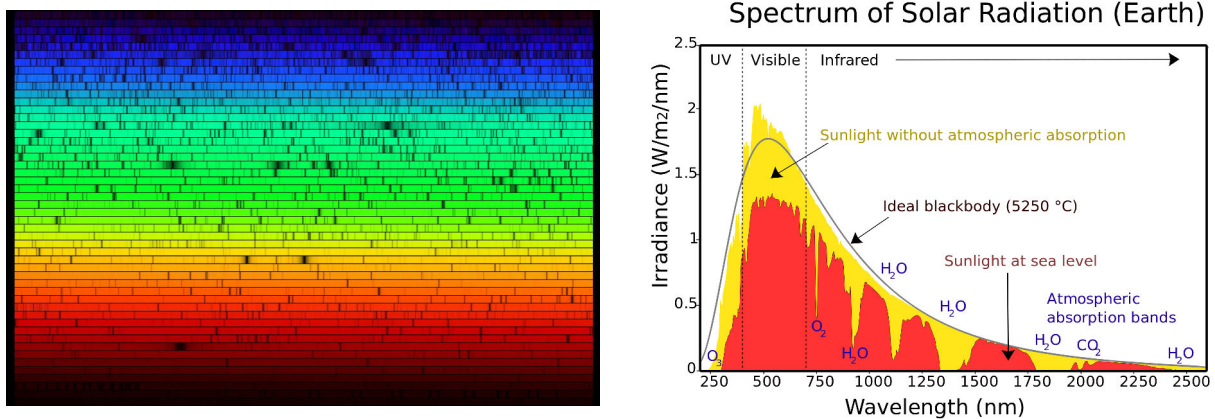


Figure 1.1: The spectrum of sunlight²; Left: Discrete lines for which no light is emitted by the Sun can be clearly seen. Right: The intensity of the spectrum is in good approximation given by the one of a black body.

can be considered to be ideal as well, as its total mass is mainly composed of Hydrogen (74%) and Helium (24%). Heavier elements make up only a very small fraction of the particles present in the Sun, but nevertheless have an important impact on its opacity, for example. The extreme temperatures of the different layers of the Sun are in strong contrast to the temperatures humans are used to, but make it possible to probe this almost ideal Hydrogen-Helium mixture at exactly these temperatures, which are for the system “natural” temperatures.

Spectroscopic experiments with sunlight were of major importance for the understanding of atomic physics, which eventually led to Quantum mechanics, one of the most successful physical theories ever formulated. The young quantum theory was completely compatible with the spectrum of solar light, which shows discrete and continuous features (see figure 1.1) at the same time: For specific wavelengths no light is emitted by the Sun, which is in accordance with the discrete nature of the absorption spectrum of atoms, predicted by Quantum mechanics. Moreover, the continuous part of the spectrum is the one of a black body, an idealized object in thermodynamical equilibrium that emits all radiation it absorbs after having thermalized it. Again, the actual form of the intensity of the spectrum, given by Planck’s law, is one of the breakthrough confirmations of Quantum mechanics.

These two aspects of the spectrum of sunlight have immediate impact on the model of the Hydrogen-Helium mixture studied in this thesis, as they confirm that the Sun is indeed at thermodynamical equilibrium (at least its outer layers), which is manifest in the continuous part of the spectrum. The discrete part of the spectrum, on the other hand, confirms that the notion of composite chemical objects, such as atoms, makes sense under solar conditions. Due to the high temperatures present in stellar objects, the atoms, held together by the Coulomb force, are not the sole constituents of the matter. In contrast to our daily experience, elementary particles, such as electrons, protons and α -particles, are also present in their unrecombined form, due to the extreme conditions found in astronomical objects. We call such a mixture of atoms and their fundamental constituents a partially ionized gas, or equivalently a partially recombined plasma. The physics of this plasma in thermodynamic equilibrium is governed by the interaction between its fundamental particles, the Coulomb interaction. The fact the constituents are partly forming more

²Source left: Nigel Sharp, National Optical Astronomical Observatories/National Solar Observatory at Kitt Peak/Association of Universities for Research in Astronomy, and the National Science Foundation; Source right: Robert A. Rohde / Global Warming Art

complex entities such as Hydrogen or Helium atoms, suggests that a Quantum mechanical treatment of the system is indispensable, due to the fact that only Quantum mechanics ensures the stability of these atoms [6].

In the early 20th century, first theories tried to describe the partially recombined plasma as an ideal mixture of Hydrogen atoms, free protons and free electrons. The chemical equilibrium between these three constituents



provides the famous **Saha-equation** [7, 8]. This simple model, which disregards all non-ideal effects such as charge-charge interactions and treats the atom as if it would only exhibit one state, the ground state, was a fundamental contribution to the understanding of the partially ionized Hydrogen gas. Already such a largely simplified model was able to predict the general pressure profile found in the Sun, and as it globally captures the physical process of recombination present in the plasma, more advanced theories can only aim to give corrections to its predictions.

The **Equation of state** of the partially ionized Hydrogen-Helium mixture, which is essentially the pressure $P(\rho, T)$ as a function of the density ρ and the temperature T , is an important ingredient for the solar models. To test these models, helioseismic observations are of great value, and their current accuracy makes it possible to precisely quantify the difference between model predictions and physical reality. A precise equation of state is, therefore, the first step to a complete understanding of our Sun.

Besides the application to our home star, the equation of state of a partially ionized gas is a basic ingredient for modeling star formation, or the understanding of interstellar nebulae. Due to the timescales on which a star is formed, even slight differences in the used equation of state can lead to important differences in the stellar evolution and eventually in the prediction of properties such as its age or structure.

From a theoretical point of view the equation of state of such a mixture is of interest on its own. Due to the long-range Coulomb interaction even the notion of an atom is non-trivial, as a naively defined partition function describing the thermodynamics of an atom is divergent [9]. As we stated before, recombination immediately suggests that a quantum mechanical treatment of the system is necessary if we want to describe it based on first principles. The operator-structure of Quantum mechanics turns this analysis, besides the many-body effects related to the long-ranged Coulomb potential, into a complicated fundamental problem.

The field has developed enormously since the early studies by Saha and generated many important physical insights. Fundamental questions, as for example, concerning the stability of such a charged partially recombined plasma have been answered [10, 11]. Several different approaches to describe the system quantitatively have been proposed, most prominently the chemical and the physical picture. The chemical picture is fundamentally based on the notion of chemical species and, therefore, strongly influenced by Saha-theory. The physical picture uses basic thermodynamic principles as well as the bare Coulomb interaction between the fundamental particles, as a starting point. Both theories have led to important improvements of our understanding of the thermodynamics of partially ionized gases.

In this thesis, we will study the equation of state of a Hydrogen-Helium mixture based on first principles. We are, thus, going to work within the physical picture and, therefore, describe the system as a gas of electrons, protons and α -particles which interact by the Coulomb potential. The presence of recombined objects such as atoms is merely a consequence of the strong interactions of these particles. Due to the long-ranged Coulomb potential, many-particle effects have a crucial effect on the equation of state. Exact reorganizations of the partition function of the system allow us to take these many-body

effects into account in a systematic and coherent way. The validity of many of the assumptions made in the chemical picture can be quantified and are motivated by the physical picture, which makes it a fruitful subject from the fundamental theoretical perspective.

This thesis is structured as follows: First, we will give a very brief overview of the history of the theoretical treatment of the physics of partially ionized gases. In particular, we will shortly describe the two main frameworks, the chemical and the physical picture.

The third chapter reviews the diagrammatic methods useful to study the physical picture, where we, by a slight modification of already existing formalisms, are able to “modularize” the physical picture. This is an important development since the modular structure of the chemical picture is often perceived as one of its major advantages over the physical picture. Moreover, after performing partial resummations of diagrams present in the diagrammatic series for the pressure, an integrable screened interaction between the basic constituents emerges. The diagrammatic description makes it possible to reduce the equation of state to a series of diagrams where a fixed number of particles is interacting, the so-called clusters.

Chapter 4 is concerned with the basic physical as well as methodical consequences of the diagrammatic described in chapter 3. Most importantly, we will answer the question of how the many-body effects influence the energy states of the present atoms. This question is not only of fundamental relevance for our calculations but also for the chemical picture as it relies on effective partition functions. Thereafter a brief analysis of the resummed screened potential is presented, which builds the basis of our subsequent numerical analysis of the particle clusters.

In chapter 5, we will describe the algorithm we developed to calculate the cluster functions, the basic objects appearing in the series of the pressure, applying numerical path integral techniques. To do so, we had to overcome two main difficulties: The singularity of the Coulomb potential at its origin and the formation of bound states at low temperatures. In this context we propose a new adaptive discretization of the numerical path integral that enables us to capture the features of the few-body Coulomb system very accurately [12]. The introduction of a physically motivated Importance sampling function extends the applicability of numerical path integral calculations, which are typically efficient for high temperatures only, to far lower temperatures. Knowledge of the behavior of the cluster functions was limited to low and high temperature regimes, and a first goal of the present work was precisely to extend this knowledge to the intermediate temperature regime.

In chapter 6 we study the partially ionized Hydrogen gas in the so-called **scaled-low-temperature** (SLT) limit, a mutual low-temperature low-density-limit. First, the theory valid in this limit will be briefly described. Afterwards we use our numerically calculated vacuum cluster functions to improve the existing models of three-particle partition functions, which account for (screened) atom-charge interactions as well as the formation of atom He and molecular ions H_2^+ and H^- in the plasma. We compare the predictions of the SLT expansion to the well accepted OPAL-tables along the solar adiabat, not only for the pressure [13] and internal energy [14], but also for the sound speed. In a second part of this chapter a simple analytical model inspired by the SLT analysis is introduced and its predictions are analyzed briefly. The SLT expansion itself as well as the simple model of the pressure, motivated by it, enjoy complete transparency and can be easily implemented, which makes them ideal equations of state for on-line use.

In chapter 7 we finally use the results of our numerical algorithm for the computation of screened cluster functions to its full extent. First, we again study the partially ionized Hydrogen gas using the screening dependent cluster functions incorporating **all** clusters with up to three particles. The differences between the OPAL, the SLT and these models are analyzed extensively and the effect of the finite density cluster functions is examined. In a second part of chapter 7 we extend this initial test analysis to the

Hydrogen-Helium case, where again all effects up to third order in the number of interacting particles are taken into account. It is shown how we account for the screening provided by charged clusters, in particular the one related to the presence of the charged He^+ ion. We close the chapter by showing our predictions of the pressure profile along the solar adiabat, for which we find excellent agreement with the currently well-established OPAL-tables.

In the final chapter we summarize our results and give ideas for further research.

Chapter 2

Review: The partially recombined plasma

In the past decades, various approaches to the equation of state of a charged plasma have been investigated with great success. These approaches can be separated into two classes, namely the chemical picture and the physical picture, according to the framework they are working with. These two pictures fundamentally differ in the way they describe the plasma.

The chemical picture assumes that the free energy potential of the whole plasma can be split into several phenomenological free energies, which describe the different chemical species present in the system [15, 16]. In the case of a partially ionized Hydrogen-Helium mixture, the corresponding particles are not only electrons, protons and α -particles, but also Hydrogen atoms, Helium atoms, He^+ , H^- and further chemical species that may form. The phenomenological free energy of the whole system is then given by

$$\mathcal{F} = F_e + F_p + F_\alpha + F_H + F_{\text{H}^-} + F_{\text{H}_2^+} + F_{\text{He}} + F_{\text{He}^+} + \dots \quad (2.1)$$

In equation (2.1), F_s is the ideal free energy of species $s = \{e, p, \alpha, \text{H}, \text{H}^-, \text{He}^+, \text{He}, \dots\}$ for N_s particles. Further terms in equation (2.1) would involve ideal contributions of, for example, H_2 molecules as well as the interactions between the several species. The free energy of species s is given by

$$\beta F_s = N_s \left[1 - \ln \left((2\pi\lambda_s^2)^{3/2} N_s / \Lambda \right) - \ln Z_s^{\text{int}} \right], \quad (2.2)$$

where the first term is the free energy of an ideal Maxwell-Boltzmann gas of N_s particles with mass m_s ($\lambda_s^2 = \beta\hbar^2/m_s$), while the second term Z_s^{int} is the internal partition function of “particle” species s . For elementary particles, such as electrons ($\sigma_e = 1/2$), protons ($\sigma_p = 1/2$) and α -particles ($\sigma_\alpha = 0$), this internal partition function merely reduces to the spin degeneracy ($2\sigma_s + 1$). The choice for the internal partition functions of composite particles, on the other hand, is non-trivial and is subject of debate. Historically, composite entities were, for instance, modeled by the famous Plank-Larkin-Brillouin partition function [17]. Another very simple approximation amounts to retain only the ground state contribution $Z_s^{\text{int}} = g_{\sigma_s} e^{-\beta E_s^0}$ of these composite objects. We stress that the inclusion of interactions between the different chemical species in the free energy functional (2.1) is also non-trivial.

At equilibrium the potential \mathcal{F} is minimal with respect to the particle numbers N_s , *i.e.* the chemical composition of the system. This minimization has to be carried out with respect to the chemical

composition only and, therefore, the total number of electrons, protons and α -particles, the volume Λ as well as the temperature T are fixed. We notice that the total number of electron is, for example, given by $N_e^{\text{total}} = N_e + N_H + 2N_{H^-} + N_{H_2^+} + 2N_{He} + N_{He^+}$, if we do not consider more complex species than explicitly given in equation (2.1). We can either add Lagrange-multipliers to the free-energy function in order to enforce these constraints directly on the level of the functional or treat these constraints separately. The famous **Saha-ionization equation** for pure Hydrogen can, for example, be derived by the simple model

$$\beta\mathcal{F}_{\text{Saha}} = N_e \left[1 - \ln \left((2\pi\lambda_e^2)^{3/2} N_e / \Lambda \right) - \ln(2) \right] \quad (2.3)$$

$$+ N_p \left[1 - \ln \left((2\pi\lambda_p^2)^{3/2} N_p / \Lambda \right) - \ln(2) \right] \quad (2.4)$$

$$+ N_H \left[1 - \ln \left((2\pi\lambda_H^2)^{3/2} N_H / \Lambda \right) - \ln(4e^{-\beta E_H}) \right] \quad (2.5)$$

where E_H is the Hydrogen ground state energy. The particle number conservation and the charge neutrality lead to the introduction of the variable x determining the fraction of ionized particles

$$\begin{aligned} N_e &= N x \\ N_p &= N x \\ N_H &= N(1 - x). \end{aligned} \quad (2.6)$$

In these new variables N and x the constraints on the particle numbers of the fundamental species are trivially fulfilled. Minimization of the free energy functional with respect to the fraction of ionized particles

$$\frac{\partial \beta\mathcal{F}(x, N, V, T)}{\partial x} = 0 \quad (2.7)$$

gives rise to the equilibrium energy $\beta F(x_{\min}, N, V, T)$ subject to the imposed conditions. Once the equilibrium free energy βF is found all thermodynamic quantities can be deduced from it by the usual identities. The pressure of the system can be calculated by the fundamental thermodynamic identity

$$\left. \frac{\partial F}{\partial V} \right|_{N, T} = -P. \quad (2.8)$$

Introducing the number density $\rho = N/\Lambda$, the usual form of the Saha-ionization equation of state for the pressure $P(\rho, \beta)$ is found

$$\beta P = \rho + \frac{1}{2}\rho^* \left(\sqrt{1 + 4\rho/\rho^*} - 1 \right) \quad \text{with } \rho^* = (2\pi\lambda_H^2)^{-3/2} e^{\beta E_H}. \quad (2.9)$$

The here described approach is, of course, only the simplest variant of an actual implementation. Refinements of this rather crude approximation have been successfully adopted, the most prominent being the occupation number formalism¹ [18]. Interactions between the chemical species can be modeled by additional terms in the free energy functional [19, 20]. These additional interaction terms can be modeled by the experimentally measured potentials (*e.g.* H_2 - H_2), or they can be determined by *ab initio*-calculations. Additional contributions arising from the Fermi-statistics of the fundamental particles as well as those

¹This approach takes into account excited states by assigning additional variables determining the number of particles occupying a certain state in the internal partition function Z^I .

related to the famous Debye term, describing screening effects of the Coulomb interaction, have been implemented. Nevertheless, the approach remains phenomenological since it is based on the assumption that the actual free energy separates into a sum of independent parts F_s . One can easily imagine that in the case of a plasma interacting by the long-ranged Coulomb potential this assumption is questionable. Further problems arise already by observing that the internal partition function of the Hydrogen atom is divergent by itself [9, 21]. This means that there is no natural choice for the model of the internal partition functions in the chemical picture.

The physical picture describes the plasma in terms of its elementary charged particles, namely electrons, protons and α -particles. This description is in sharp contrast to the chemical picture where the chemical species are introduced by assuming the separability of the free energy. These elementary particles interact with the bare Coulomb potential, unlike in the chemical picture, where often effective ad-hoc expressions for the interspecies potentials are assumed. The central quantity for the analysis of the system in the physical picture is the Grand canonical partition function [22, 23]

$$\Xi(\beta, \{\mu_\gamma\}, V) = \text{Tr} \left[e^{-\beta(H_{\{\gamma\}} - \sum_\gamma \mu_\gamma N_\gamma)} \right] \quad (2.10)$$

where N_γ is the particle number of species γ and μ_γ are the related chemical potentials. The Hamiltonian of this N -particle system is given by²

$$H_{\{N_\gamma\}} = - \sum_{i=1}^N \frac{\hbar^2}{2m_{\gamma_i}} \Delta_i + \frac{1}{2} \sum_{i \neq j}^N \frac{e_{\gamma_i} e_{\gamma_j}}{|\mathbf{x}_i - \mathbf{x}_j|}. \quad (2.11)$$

We stress that no chemical species are introduced a priori. The thermodynamic quantities are derived from the Grand canonical potential

$$-\beta\Omega = \beta P\Lambda = -\ln(\Xi). \quad (2.12)$$

Different exact asymptotic expansions of the Grand canonical potential have been studied in the last century. These expansions cover different physical parameter regimes, where, for example, the system is almost fully ionized in its elementary charged particles, *i.e.* the electrons and the nuclei. The asymptotic expansion in this particular regime corresponds to the famous **virial expansion**, for which the Grand canonical partition function is developed in powers of the density ρ at fixed temperature T . First steps in this direction were taken by Ebeling [24] (order ρ^2), and higher order terms were later calculated by several authors [25, 26, 27, 28, 29]. Interestingly, these calculations were performed using different techniques, such as the effective potential method [30], the path integral representation as well as effective field theory. All these different approaches agree up to order $\rho^{5/2}$ [29] included.

To study the system at finite densities ρ , Rogers introduced the so-called **ACTivity EXpansion** (ACTEX) formalism which takes recombination effects into account. In this approach, the composite particles are identified as associated with the short-range contributions in the usual fugacity expansion of the Grand canonical potential, for which Quantum mechanics has a crucial role. Long-range contributions, which *a priori* diverge are treated classically by replacing the Coulomb potential with the Debye potential. This provides the pressure as an explicit, approximate, function of the fugacities, from which the equation of state can be derived through the standard thermodynamic identities. The ACTEX method was used to build the widely employed **OPAL**-tables, which presents the most prominent incarnation of a physical

² $N = \sum_\gamma N_\gamma$

picture calculation [31]. These tables are freely available on the Internet, and a large community of scientists in various fields employs them as an ingredient for their numerical calculations. As already stated in the Introduction, the equation of state of either a pure Hydrogen system or of the Hydrogen-Helium mixture is of fundamental importance for the modeling of stars as well as the formation of galaxies or the fluid dynamics of interstellar nebulae. One major downside of these tables is that the code used to generate them is not freely available and, therefore, we can only speculate about the actual implementation of the physical processes, which are said to be considered [32]. Even though the physical processes, taken into account in the OPAL-tables are described, no explicit formulas are given. This led even to a thesis dedicated to emulate these tables in order to quantitatively understand the ingredients and physical assumptions of this model [33].

A systematic account for recombination and simultaneously for screening within the plasma has been achieved in Ref. [34]. The authors used the path integral representation of the quantum plasma as basic tool, which leads to the notion of loops, *i.e.* extended objects take the place of the zero-dimensional elementary particles. Using such a representation the quantum plasma of elementary particles is described as a classical gas of loops. In this new formulation, standard Mayer diagrammatics [35] can then be applied and chain resummations, which give rise to the Debye potential in the classical case, can be performed to remove the long-range divergencies. After this resummation, the particle densities are given by a diagrammatic series build with this new screened loop-loop potential, and particle clusters can be associated with chemical species. Such a formalism can be viewed as the proper mathematical formulation of the ideas underlying the ACTEX method.

The so-formulated **Screened-Cluster-Representation** (SCR) has been used to derive exact asymptotic expansions around Saha theory for pure Hydrogen. In fact, Saha theory has been proven to become exact in a double low-temperature low-density limit [10, 11, 36]. The SCR can be used to study this **Scaled-Low-Temperature-limit** (SLT) and provides the proper tool to collect all non-ideal corrections to the Saha equation [13]. Corrections related to charge-charge and charge-atom interactions, to the formation of more complex entities such as H_2^+ and H^- ions as well as H_2 molecules, are accounted for. The authors used phenomenological models, from ground state approximations to more sophisticated models³, to approximate the higher order partition functions [37, 14]. We will numerically evaluate the explicit expressions of the cluster functions in terms of path integrals, given in Ref. [13], to make this phenomenological modeling unnecessary [12]. Compared to the virial expansion, the SLT expansion has a wider range of validity in the phase diagram since it also includes the partially ionized regime.

Besides these approaches the **Path Integral Monte-Carlo** (PIMC) method as well as the **Density Functional Theory** (DFT), constitute numerical techniques to describe the physics of charged plasmas [38, 39, 40, 41]. *Ab initio* methods, well appropriate for high densities, have been applied to the Hydrogen-Helium mixture with great success (Ref. [42] and references therein). These methods allow not only to access the equation of state but also other quantities, as for example, the electrical or the thermal conductivity. The name path integral Monte-Carlo originates from the identification of the fundamental particles with paths, by virtue of the Feynman-Kac formula [43]. In this approach the fundamental particles do interact with the bare Coulomb potential, but for numerical reasons the pair-action approximation is used in combination with exact two-particle actions, in practice [38]. The fermionic nature of the electrons, gives rise to the so-called fermion sign problem⁴. For bosons this sign-problem is not present and, thus, the PIMC-method has been applied extensively to study super-fluidity, for example [44, 45]. Due

³The two proton, one electron cluster describing the H_2^+ -molecule is, for example, described by a rotator-vibrator model

⁴The fermion sign problem is directly related to the anti-symmetry of the overall fermion wave function and, therefore, to the fact that the partition function of a fermion system is given by a Slater determinant.

to poor statistics, the PIMC is not well suited at low densities, but it is appropriate to study the high temperature moderate density regime⁵.

In the following chapter we will present the basics of the physical picture using the well-known Mayer-diagram techniques in combination with the path integral formalism. This chapter will give us the tools to analyze the equation of state of the Hydrogen-Helium mixture, as it is necessary to understand the reasoning that led to the SLT expansion, as well.

⁵The importance of the fermion sign problem is determined by the ratio of the free wavelength λ of the electrons and their mean distance.

Chapter 3

The loop representation and quantum Mayer diagrams

3.1 Introduction

The loop representation is a seemingly classic formulation of Quantum mechanics that enables us to use standard classical many-body techniques in the context of the thermodynamics of a N-particle quantum Coulomb system at equilibrium. Its basis is the Feynman-Kac formula leading to a change in paradigm [43]. The complex operator and Hilbert space structure of the usual wave function picture is replaced by functional integrals over paths between points in space. We will use this formalism to rewrite the Grand canonical potential in terms of path integrals. Elements in the fugacity series are called “quantum Mayer diagrams”, the quantum equivalents of the standard virial coefficients. These objects made from loops of particles, which reflects the quantum nature of the particles. Due to the long-range character of the Coulomb potential each individual Mayer diagram alone is divergent. It is only after partial resummations of the diagrammatic series, which account for collective effects such as screening, that its elements become finite and well defined. The basic interaction between particles does alter after these resummations are considered, removing the large-distance divergence of the Mayer diagrams. We devote a subsection to the properties of this “effective” potential since we will use it later in our numerical calculations. Due to the importance of recombination effects in the partially ionized plasma, the subject of this thesis, we cannot take the potential into account perturbatively. The loop-formalism is well-suited to treat this non-perturbative problem. For a general overview of the variety of applications of the loop-formalism see Ref. [27, 34, 13, 46].

In the following, we will develop and apply the quite general loop-formalism to the fugacity expansion of the Grand canonical potential of a Coulombic system. The computational techniques necessary to evaluate these cluster integrals numerically are presented in chapter 5.

3.2 The loop representation

Two basic requirements have to be fulfilled by the description of the system. We want to be able to consider the thermodynamic limit $V \rightarrow \infty$ and we demand the system to be charge neutral

$$\sum_{\gamma} \rho_{\gamma} e_{\gamma} = 0. \quad (3.1)$$

Here ρ_{γ} is the density of component γ with charge e_{γ} . The first means that we should use a thermodynamic potential where the volume V is a parameter. In the Canonical ensemble the particle number of each species N_{γ} is fixed and a neutral system is only achieved for very specific configurations of those. As shown by Lieb-Liebowitz [11], the neutrality of a system described by the Grand canonical ensemble is automatically assured, which advocates the Grand canonical ensemble as an appropriate choice. We thus assume our system to be coupled to a thermostat which fixes the temperature T of the system and to a particle bath for each plasma component with fixed chemical potential μ_{γ} . These basic considerations lead to the choice of the Grand canonical ensemble $\Omega(T, V, \{\mu_{\gamma}\})$ to describe the macroscopic physics of the Coulomb mixture. The macroscopic description of the system by the Grand canonical ensemble is related to its microscopic description by the Hamiltonian through the Grand canonical partition function

$$\Omega(T, V, \{\mu_{\gamma}\}) = -k_B T \ln \Xi(T, V, \{\mu_{\gamma}\}) \quad (3.2)$$

with

$$\Xi(T, V, \{\mu_{\gamma}\}) = \text{Tr} \left[e^{-\beta H_{\{N_{\gamma}\}} + \beta \sum_{\gamma} \mu_{\gamma} N_{\gamma}} \right], \quad (3.3)$$

where $\beta = 1/k_B T$ is the inverse temperature. The N-body Hamiltonian is given by

$$H_{\{N_{\gamma}\}} = - \sum_{i=1}^N \frac{\nabla_i^2}{2m_{\gamma}} + \sum_{i=1}^N \sum_{j=1}^{i-1} V(\mathbf{x}_i, \mathbf{x}_j), \quad (3.4)$$

where we are interested in the particular case where particles interact via the Coulomb potential

$$V(\mathbf{x}_i, \mathbf{x}_j) = \frac{e_{\gamma_i} e_{\gamma_j}}{|\mathbf{x}_i - \mathbf{x}_j|}. \quad (3.5)$$

Considering a classical ensemble, the trace would run over all classical inner degrees of freedom, the positions of the particles \mathbf{x} , their momenta and, since the system is coupled to a particle reservoir, the number of particles N_{γ} for each species γ .

In Quantum mechanics, the Hamiltonian is not a function, but an operator and the trace is a symmetrized operator trace reflecting the statistics of the particle species. The operator trace in formula (3.3) can be written as a sum of Slater determinants, built from one-body states $|\{\sigma_i, \mathbf{x}_i\}\rangle$ in the basis formed by spin-space eigenstates. Since the particle number is not fixed in the Grand canonical ensemble, it also invokes a summation over this internal degree of freedom of the system. The symmetrization introduced by the Slater determinant, symmetrizes each particle species subspace independently ($\mathcal{P} = \mathcal{P}_e \otimes \mathcal{P}_p \otimes \mathcal{P}_{\alpha}$ in the case of the Hydrogen-Helium mixture, for example). The Grand canonical partition (3.3) function

is written explicitly

$$\Xi = \sum_{\{N_\gamma\}=0}^{\infty} e^{\sum_\gamma \beta N_\gamma \mu_\gamma} \sum_{\mathcal{P}} \epsilon(\mathcal{P}) \sum_{\{\sigma_{e,i}\}, \{\sigma_{p,j}\}, \{\sigma_{\alpha,k}\}} \langle \sigma_{e,\mathcal{P}(i)} | \sigma_{e,i} \rangle \langle \sigma_{p,\mathcal{P}(j)} | \sigma_{p,j} \rangle \langle \sigma_{\alpha,\mathcal{P}(k)} | \sigma_{\alpha,k} \rangle \quad (3.6)$$

$$\prod_i \int d\mathbf{x}_i \langle \mathbf{x}_1, \mathbf{x}_2, \dots, \mathbf{x}_N | \exp(-\beta H_{N_e, N_p, N_\alpha}) | \mathbf{x}_{\mathcal{P}(1)}, \mathbf{x}_{\mathcal{P}(2)}, \dots, \mathbf{x}_{\mathcal{P}(N)} \rangle.$$

In the above formula $\epsilon(\mathcal{P}) = \epsilon(\mathcal{P}_e)\epsilon(\mathcal{P}_p)\epsilon(\mathcal{P}_\alpha) = \pm 1$ is the signature of the permutation \mathcal{P} . Using the Feynman-Kac path integral formalism [43] the matrix element is expressed in terms of functional integrals over all paths $\xi_i(s)$ between the root points \mathbf{x}_i and $\mathbf{x}_{\mathcal{P}(i)}$

$$\langle \{\mathbf{x}_i\} | e^{-\beta H_{\{N_\gamma\}}} | \{\mathbf{x}_{\mathcal{P}(i)}\} \rangle = \prod_i \frac{\exp\left[-\sum_i (\mathbf{x}_i - \mathbf{x}_{\mathcal{P}(i)})^2 / (2\lambda_{\gamma_i}^2)\right]}{(2\pi\lambda_{\gamma_i}^2)^{3/2}} \int \mathcal{D}(\boldsymbol{\xi}_i) \exp\left[\dots \right] \quad (3.7)$$

$$- \sum_{i \neq j} \frac{e_{\gamma_i} e_{\gamma_j} \beta}{2} \int_0^1 ds V\left((1-s)(\mathbf{x}_i - \mathbf{x}_j) + s(\mathbf{x}_{\mathcal{P}(i)} - \mathbf{x}_{\mathcal{P}(j)}) + \lambda_{\gamma_i} \boldsymbol{\xi}_i(s) - \lambda_{\gamma_j} \boldsymbol{\xi}_j(s)\right) \Big]$$

where the potential $V(\mathbf{r}) = 1/|\mathbf{r}|$ is the usual Coulomb potential (3.5) and the thermal wavelength of species γ is defined as $\lambda_\gamma = \sqrt{\hbar^2 \beta / m_\gamma}$. The paths $\boldsymbol{\xi}_i(s)$ are parametrized by a dimensionless fictitious time variable s . The distribution of path shapes is given by the Wiener measure which is, being Gaussian, completely defined by its covariance

$$\int \mathcal{D}(\boldsymbol{\xi}_i) \boldsymbol{\xi}_i(s) \boldsymbol{\xi}_j(t) = \mathbb{1}_{\delta_{i,j}} \inf(s, t) (1 - \sup(s, t)), \quad (3.8)$$

together with the condition $\boldsymbol{\xi}(0) = \boldsymbol{\xi}(1) = 0$. The paths $\mathbf{x}_i(s) = (1-s)\mathbf{x}_i + s\mathbf{x}_{\mathcal{P}(i)} + \lambda_{\gamma_i} \boldsymbol{\xi}_i(s)$ introduced by the Feynman-Kac path integral description are either closed if $\mathcal{P}(i) = i$ or open otherwise. The cyclic permutations of the root points $\mathbf{x}_i, \mathbf{x}_{\mathcal{P}(i)}$ can be exploited to collect open paths to form larger closed paths involving several particles of the same species. The sum over these permutations (3.6) together with the summation over the number of particles leads to the product of all possible combinations of globally closed paths containing an arbitrary number of particles of the same species, the so-called loops. We can, thus, exactly rewrite the Grand canonical partition function (3.3) in terms of these closed loops \mathcal{L} [47]

$$\Xi = \sum_N \frac{1}{N!} \prod_i \sum_{q_i=1}^{\infty} \int \mathcal{D}(\mathcal{L}_i) z(\mathcal{L}_i) \exp\left[-\frac{\beta}{2} \sum_{i \neq j} V(\mathcal{L}_i, \mathcal{L}_j)\right], \quad (3.9)$$

where the Quantum loop-loop potential is given by

$$V(\mathcal{L}_1, \mathcal{L}_2) = e_{\gamma_1} e_{\gamma_2} \int_0^{q_1} ds_1 \int_0^{q_2} ds_2 V(\mathbf{x}_1 - \mathbf{x}_2 + \lambda_{\gamma_1} \boldsymbol{\eta}_1(s_1) - \lambda_{\gamma_2} \boldsymbol{\eta}_2(s_2)) \tilde{\delta}(s_1 - s_2). \quad (3.10)$$

The Dirac comb $\tilde{\delta}$ of period one defined by

$$\tilde{\delta}(s) = \sum_{n=-\infty}^{\infty} \delta(s+n) \quad (3.11)$$

enforces the interaction at same ‘‘times’’ with respect to the original open paths $\boldsymbol{\xi}(s)$. Suppressing the

Dirac comb in formula (3.10) would lead to classical interaction of two charged wires and, thus, its presence reflects the quantum nature of the particles. The inner degrees of freedom of a given loop \mathcal{L} are: its root point chosen arbitrarily among those of the particles forming the loop, the number of particles q involved, the spin common to all exchanged particles and eventually the shape of the loop $\boldsymbol{\eta}(s)$ with $0 < s < q$. The loop shapes are distributed according to the Wiener-measure, which is completely determined by its covariance

$$\int \mathcal{D}(\boldsymbol{\eta}) \boldsymbol{\eta}_i(s) \boldsymbol{\eta}_j(t) = \mathbb{1} \delta_{i,j} \inf(s/q_i, t/q_i) (1 - \sup(s/q_i, t/q_i)). \quad (3.12)$$

The shape-property of the loops implements the inherent quantum fluctuations of the particles in a seemingly classical way. The complex structure of quantum mechanics (commutation relations) is hidden in the functional integration of loop shapes. The integration-measure $\int \mathcal{D}(\mathcal{L})$ is explicitly given by

$$\int \mathcal{D}(\mathcal{L}) F(\mathcal{L}) = \sum_{\gamma=e,p,\alpha} \sum_{\sigma} \sum_{q=1}^{\infty} \int d\mathbf{x} \int \mathcal{D}(\boldsymbol{\eta}) F(\mathbf{x}, \gamma, \sigma, \boldsymbol{\eta}(s)), \quad (3.13)$$

in the Hydrogen-Helium case. The loop-fugacity introduced in equation (3.9) is the bare fugacity z_{γ}^q of q particles of species γ , times additional factors containing the interactions of the particles in the loop itself and combinatorial factors reflecting the collection of several open paths into one closed loop

$$z(\mathcal{L}) = (-1)^{q-1} \frac{z_{\gamma}^q \exp(-\beta U(\mathcal{L}))}{q (2\pi q \lambda_{\gamma}^2)^{3/2}} \quad \text{with} \quad z_{\gamma} = e^{\beta \mu_{\gamma}}. \quad (3.14)$$

The interaction between the q particles inside the loop \mathcal{L} defines the self-energy of the loop

$$U(\mathcal{L}) = \frac{e_{\gamma}^2}{2} \int_0^q ds_1 \int_0^q ds_2 V(|\boldsymbol{\eta}(s_1) - \boldsymbol{\eta}(s_2)|) (1 - \delta_{\lfloor s_1 \rfloor, \lfloor s_2 \rfloor}) \tilde{\delta}(s_1 - s_2), \quad (3.15)$$

where the discrete δ -function avoids self-interaction of particles. The seemingly classic loop-representation of the partition function (3.9) enables us to use the standard statistical mechanics technique of Mayer diagrams to carry out an activity (fugacity) expansion on the level of loops.

3.3 Bare quantum Mayer diagrams

Assuming that the particle density is low the bare fugacities can be expected to be a small parameter in which the Grand Canonical partition function Ξ can be expanded. Historically, this expansion and its diagrammatic representation has been first introduced by Mayer [35, 48] for classical systems. The partition function of the quantum loop gas is analogous to that of a classical system, where the usual point particles are replaced by extended objects called “loops”. These loops are complex classical objects, with shapes describing the quantum fluctuations of the underlying point particles and their statistics. After this identification the quantum nature of the particles is hidden in the functional integration over all loop shapes and the Mayer diagrammatic can be applied in a straight forward manner.

The Quantum loop gas

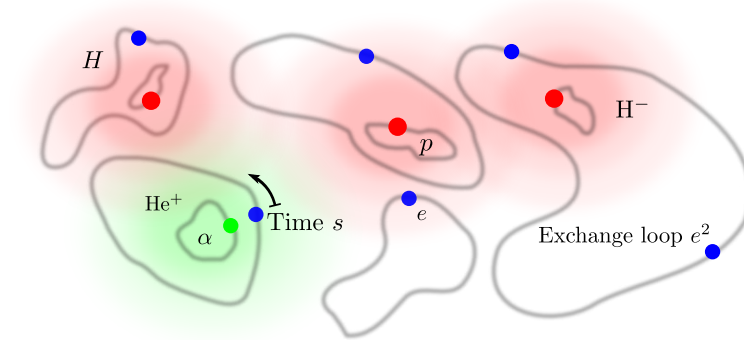


Figure 3.1: In the loop-picture of quantum statistical mechanics, paths are closed but can involve an arbitrary number of particles.

The introduction of the so-called Mayer bond¹

$$f(\mathcal{L}_1, \mathcal{L}_2) = \exp(-\beta V(\mathcal{L}_1, \mathcal{L}_2)) - 1 = \begin{array}{c} \bullet \cdots \bullet \\ 1 \quad 2 \end{array}, \quad (3.16)$$

in equation (3.9) leads to the separation of diagrams in two classes: those for which a path made with f -bonds between all loops can be found and those where it cannot. Taking the logarithm of the so rewritten series of diagrams suppresses all configurations where the loops are not connected by bonds of the Mayer-type (3.16), so that the series for the Grand canonical ensemble can be written as follows:

$$-\beta\Omega = \log(\Xi) = \sum_{N=1} \frac{1}{N!} \left[\prod_i \int \mathcal{D}(\mathcal{L}_i) z(\mathcal{L}_i) \right] \prod_{i < j}^N (f(\mathcal{L}_i, \mathcal{L}_j) + 1) \Big|_{\text{connected}}. \quad (3.17)$$

The product of bonds in equation (3.17) can be represented in a convenient manner using diagrams. Each node in these Mayer diagrams is identified with a loop and, therefore, with a fugacity-factor in equation (3.17), and the product of Mayer bonds $\prod (f + 1)$ is represented by links between the nodes of the diagram. The integration over inner degrees of freedom is implicit if not indicated otherwise. Example diagrams illustrating the class of disconnected and connected diagrams are shown in figure 3.2.

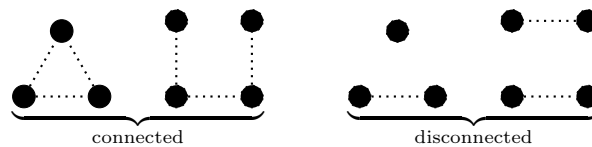


Figure 3.2: Connected and disconnected graphs. The dotted line represents an arbitrary bond.

It should be remembered that in this description the particle species of a loop is an internal degree of

¹Several gray nodes can be superposed to form a diagram, and are afterwards colored black.

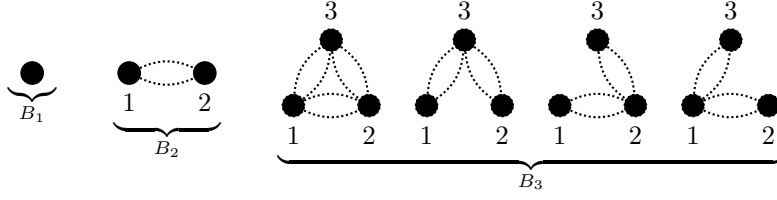


Figure 3.3: The first three virial coefficients

freedom over which the sum is taken in each loop independently. By defining

$$B_N(\{\mathcal{L}\}) = \frac{1}{N!} \prod_{i < j}^N (f(\mathcal{L}_i, \mathcal{L}_j) + 1) \Big|_{\text{connected}}, \quad (3.18)$$

we recover the standard expansion of the Grand canonical ensemble in terms of standard virial coefficients (see figure 3.3)

$$-\beta\Omega = \sum_N \int \left[\prod_i \mathcal{D}(\mathcal{L}_i) z(\mathcal{L}_i) \right] B_N(\{\mathcal{L}_i\}) \quad (3.19)$$

The virial coefficient B_N is the sum of all connected diagrams containing N nodes using the bare Mayer bond (3.16). In the Coulomb case these virial coefficients are divergent due to the long-range non-integrability of the potential. This divergence calls for a resummation in order to be able to assign a finite value to the diagrams, which is briefly presented in the following section. In contrast to the classical virial coefficient the nodes do not represent solely particle positions but do have an additional loop shape degree of freedom and contain an arbitrary number of particles of the same species with the same spin. In addition, the fugacities have gained structure and depend on the loop shape and internal degrees of freedom (see equations (3.14) and (3.15)), too. The number of particles is an inner degree of freedom of each loop in the former formulation. We extract this degree of freedom and make it an explicit parameter of the loop as well as the loop species

$$-\beta\Omega = \sum_N \int \left[\prod_i \sum_{\gamma_i = e, p, \alpha} \sum_{q_i = 0}^{\infty} \mathcal{D}(\mathcal{L}_{i, \gamma_i, q_i}) z(\mathcal{L}_{i, \gamma_i, q_i}) \right] B_N(\{\mathcal{L}_{i, \gamma_i, q_i}\}). \quad (3.20)$$

The first terms in the expansion in bare fugacities are, for example, given by

$$\begin{aligned} -\beta\Omega = & \underbrace{\sum_{\gamma_1} \int \mathcal{D}(\mathcal{L}_{1, \gamma_1, 1}) z(\mathcal{L}_{1, \gamma_1, 1})}_{\text{one particle in one loop}} \underbrace{B_1}_{=1} + \underbrace{\sum_{\gamma_1} \int \mathcal{D}(\mathcal{L}_{1, \gamma_1, 2}) z(\mathcal{L}_{1, \gamma_1, 2})}_{\text{two particles in one loop}} \underbrace{B_1}_{=1} \\ & + \underbrace{\sum_{\gamma_1} \sum_{\gamma_2} \int \mathcal{D}(\mathcal{L}_{1, \gamma_1, 1}) \int \mathcal{D}(\mathcal{L}_{2, \gamma_2, 1}) z(\mathcal{L}_{1, \gamma_1, 1}) z(\mathcal{L}_{2, \gamma_2, 1})}_{\text{two particles in two connected loops}} B_2(\mathcal{L}_{1, \gamma_1, 1}, \mathcal{L}_{2, \gamma_2, 1}) \\ & + \dots, \end{aligned} \quad (3.21)$$

where we recall that the loop fugacity with a fixed number of particles q is proportional to $z(\mathcal{L}_{\gamma, q}) \sim z_{\gamma}^q$.

If we write the first term in this expansion explicitly

$$\sum_{\gamma_1} \int \mathcal{D}(\mathcal{L}_{1,\gamma_1,1}) z(\mathcal{L}_{1,\gamma_1,1}) = \sum_{\gamma_1} \int d\mathbf{r} \underbrace{\int \mathcal{D}(\xi)}_1 \sum_{\sigma_\gamma} \frac{z_\gamma}{(2\pi\lambda_\gamma^2)^{3/2}} \sim \int d\mathbf{r} \sum_{\sigma_\gamma} \frac{z_\gamma}{(2\pi\lambda_\gamma^2)^{3/2}} \quad (3.22)$$

we see immediately that due to the translational invariance we get a result depending on the size of the integration volume. By general thermodynamic considerations the Grand canonical ensemble for a homogeneous (translational invariant) system is given by

$$\Omega = -PV \quad (3.23)$$

so that

$$-\beta\Omega = \beta PV = \text{series of Mayer-type diagrams.} \quad (3.24)$$

Having realized that all diagrams appearing in the series (3.20) are proportional to the volume of the system we can divide it out and find for the pressure

$$\beta P = \frac{1}{V} \text{series of Mayer-type diagrams.} \quad (3.25)$$

Dividing by the volume is equivalent to not integrating over one loop root point, so that we have to integrate over relative distances of the loops, only.

3.3.1 Symmetry factors and topological structure of the Mayer diagrams

The formula (3.17) can be further manipulated to combine all diagrams that have the same topological structure. The last three diagrams in figure 3.3, for instance, can be gathered into one single diagram to which one associates a symmetry factor, due to the fact that they all have the same numerical value [49]. The resulting formula for the Grand canonical ensemble and thereby for the pressure has been derived in Ref. [47, 27]

$$-\beta\Omega = \sum_{\mathcal{G}} \frac{1}{S(\mathcal{G})} \left[\prod_i \int \mathcal{D}(\mathcal{L}_i) z(\mathcal{L}_i) \right] \prod_{i \neq j} (f(\mathcal{L}_i, \mathcal{L}_j) + 1) \Bigg|_{\mathcal{G}}. \quad (3.26)$$

The sum $\sum_{\mathcal{G}}$ runs over all topologically different graphs that are connected. The symmetry factor is given by $N!$ divided by the number of topologically equivalent diagrams in the product $\prod_{i < j}^N (f(\mathcal{L}_i, \mathcal{L}_j) + 1)$, which have the same structure as \mathcal{G}_N . The symmetry factor of a diagram can be easily found by counting the number of permutations of the bonds that leave the product of bonds invariant. To give an example we deduce the symmetry factors of the three loop diagrams

$$\begin{array}{ccc} \begin{array}{c} 3 \\ \bullet \\ \diagup \quad \diagdown \\ \bullet \quad \bullet \\ 1 \quad 2 \end{array} & \rightarrow & S = 2 \\ \begin{array}{c} 3 \\ \bullet \\ \diagup \quad \diagdown \\ \bullet \quad \bullet \\ 1 \quad 2 \end{array} & \rightarrow & S = 6. \end{array} \quad (3.27)$$

In a diagrammatic formalism consisting of several bonds, these bond-types have to be taken into account in the assignment of the symmetry factor to a diagram since only bonds of the same type can be permuted.

Furthermore, if the symmetry of the nodes is broken, for example, by being made of different species or a different number of internal particles the symmetry between the bonds is broken indirectly

$$\begin{array}{ccc}
 \begin{array}{c} 3 \\ \bullet \\ / \quad \backslash \\ \bullet \quad \bullet \\ 1 \quad 2 \end{array} \rightarrow S = 1 &
 \begin{array}{c} 3 \\ \bullet \\ / \quad \backslash \\ \bullet \quad \bullet \\ 1 \quad 2 \end{array} \rightarrow S = 2 &
 \begin{array}{c} 3 \\ \bullet \\ / \quad \backslash \\ \bullet \quad \bullet \\ 1 \quad 2 \end{array} \rightarrow S = 2.
 \end{array} \quad (3.28)$$

To summarize, the symmetry factor is defined as the number of permutations of the bonds that leave the product of bonds invariant.

3.3.2 From pressure to density

Equation (3.21) provides a series expansion of the pressure in terms of fugacities. As we are interested in the pressure as a function of the relative abundances and the density rather than fugacities, we also need the relation for the particle densities ρ_γ in terms of the fugacities z_γ . The definition of the average particle number of species γ in the Grand canonical ensemble is given by

$$N_\gamma = -\frac{\partial \Omega}{\partial \mu_\gamma} = -\frac{\partial \Omega}{\partial z_\gamma} \frac{\partial z_\gamma}{\partial \mu_\gamma} = -z_\gamma \frac{\partial \beta \Omega}{\partial z_\gamma}. \quad (3.29)$$

The densities are, thus, expressible as the derivative of the pressure with respect to z_γ

$$\rho_\gamma = z_\gamma \frac{\partial \beta P}{\partial z_\gamma} = z_\gamma \frac{\partial \text{series of Mayer diagrams}}{\partial z_\gamma}. \quad (3.30)$$

On the level of diagrams, the rule for passing from the pressure to the density is that the derivative acting on a node colors it white

$$z_\gamma \frac{\partial}{\partial z_\gamma} \bullet_\gamma = \circ_\gamma. \quad (3.31)$$

This way the rules for the symmetry factor are completely preserved with one slight modification owed to the quantum statistics of the particles. For the nodes not containing single particles but loops, which are made of q particles, a white point does carry an extra factor of q (from the derivative acting on the bare fugacities of the loop particles $z \frac{\partial z^q}{\partial z} = qz^q$).

In the following, we will first inspect the quantum equivalent of the Debye potential, indispensable due to the long-range nature of the Coulomb potential. Afterwards, we will see how the neutrality of the system is realized on the level of Mayer diagrams.

3.4 Screened quantum Mayer Diagrams

Due to the long-range of the Coulomb potential many-particle effects are of particular importance [34, 46] in the Coulomb gas. The non-integrability of the Coulomb potential at large distances makes it necessary to consider resummations of Quantum-Mayer diagrams. The result is the loop equivalent of the widely known RPA-resummation, which gives rise to the Debye potential. The classical Debye-Hückel

theory leads to an integrable effective potential

$$\beta V_{\text{DH}} = \beta e_i e_j \frac{e^{-\kappa|\mathbf{r}|}}{|\mathbf{r}|} \quad \text{with} \quad \kappa = \sqrt{4\pi\beta \sum_{\gamma} e_{\gamma}^2 \frac{z_{\gamma}}{(2\pi\lambda_{\gamma}^2)^{3/2}}} \quad (3.32)$$

between particles. This potential can be diagrammatically interpreted as a result of the resummation

$$\begin{aligned} -\beta V_{\text{DH}}(\mathbf{r}, \mathbf{r}') &= \text{○} \text{---} \text{○} \\ &= \text{○} \text{---} \text{○} + \text{○} \text{---} \bullet \text{---} \text{○} + \text{○} \text{---} \bullet \text{---} \bullet \text{---} \text{○} + \dots \end{aligned} \quad (3.33)$$

of convolutions of the bare Coulomb bonds

$$-\beta V(\mathbf{r}, \mathbf{r}') = \text{○} \text{---} \text{○}. \quad (3.34)$$

Since the quantum properties are hidden in inner degrees of freedom of the loops, it is tempting to carry out the same type of resummation on the level of loops. The resummation on either classical or quantum level induces double counting rules that prohibit some diagrams appearing in the original series (3.17) and (3.20), which have to be taken into account to preserve consistency. The analysis is presented in [50] in a very pedagogical manner. Therefore, we will present the steps of the calculation only very briefly. Two points have to be examined: First, the influence of the resummation on the series (3.17) and second, the structure of the resummed loop potential itself.

3.4.1 Resummed Mayer diagrams

Due to the long-range character of the Coulomb potential the resummation procedure is essential, since it leads to a loop-loop potential which is integrable and, therefore, assures the finiteness of the quantum virial coefficients. We sketch the ideas behind the resummation procedure and refer the interested reader to Ref. [34] where it is carried out with complete rigorousness². The Mayer bond (3.16), used in the current series (3.26) for the pressure, can be decomposed into powers of the bare loop-loop potential V

$$\begin{aligned} f(\mathcal{L}_1, \mathcal{L}_2) &= \exp(-\beta V(\mathcal{L}_1, \mathcal{L}_2)) - 1 = \text{●} \text{---} \text{●} \\ &= \sum_{n=1}^{\infty} \frac{1}{n!} (-\beta V(\mathcal{L}_1, \mathcal{L}_2))^n = \text{●} \text{---} \text{●} + \text{●} \text{---} \text{---} \text{●} + \text{●} \text{---} \text{---} \text{---} \text{●} + \dots \end{aligned} \quad (3.35)$$

It is instructive to realize that this decomposition does not change the diagrammatic rules due to the combinatorial factor $1/n!$ present in the expansion of the exponential (3.35) which exactly coincides with the symmetry factor of each of the terms in the diagrammatic expansion. In this decomposed diagrammatic we have to consider all diagrams made of the bond V where an arbitrary number of dashed bonds can bridge between two nodes. The symmetry factors of these diagrams can be deduced by applying the usual rule³. For each diagram in which no convolution of the bond V is present, there are topologically equivalent diagrams where the bare bond is replaced by an arbitrary number of convolutions of bonds V

²In this paper resummations are performed for the diagrammatic series of the particle density. The presented resummation for the pressure involve the same combinatorics, except for the ring structures as noticed latter

³The symmetry factor is equal to the number of permutations that leave the product of labeled bonds unchanged.

with intermediate black nodes. For example, the diagrams

$$\text{---} \quad , \quad \text{---} \quad . \quad (3.36)$$

belong to the same class and will be combined. All bridges between the two “end” points can be compactly expressed by introducing the resummed potential

$$\begin{aligned} -\beta\phi(\mathcal{L}_1, \mathcal{L}_2) &= \text{---} \\ &= \text{---} + \text{---} + \text{---} + \dots \end{aligned} \quad (3.37)$$

The overall symmetry of the bridges between the two root nodes is restored and thereby the symmetry factor of the resummed diagram is equal to the original bare one. For specific realizations of convolutions the symmetry factor is actually not necessarily equivalent to the one of the original diagram. Only after considering the sum of all realizations of convolutions the symmetry of the bonds and consequently the symmetry factor is restored

$$\underbrace{\text{---}}_{S=6} + \underbrace{\text{---}}_{S=\text{dependent on specific realization}} = \underbrace{\text{---}}_{S=6} \quad (3.38)$$

After the introduction of the new bond $-\beta\phi$ equation (3.38) the diagrammatic rules have to be changed in order to prevent double counting of diagrams. The set of diagrams permitted is limited to those where no convolutions of the resummed potential ϕ are present. This requirement excludes, for example, the diagram

$$\text{---} \quad , \quad (3.39)$$

which involves a convolution of ϕ and, therefore, double counts diagrams of the original V series⁴. After resumming the diagrams in each class, two nodes can usually be connected by an arbitrary number of bonds $-\beta\phi$ in parallel. An exception is the case that one node is connected to the rest of the diagram by two bonds $-\beta\phi$ in parallel. The diagram

$$\text{---} \quad , \quad (3.40)$$

for instance, does require special treatment due to the fact that it double counts diagrams in the original decomposed series. To correct for this double counting we have to replace one of the two parallel bonds

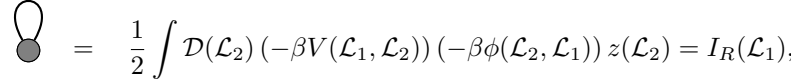
⁴ --- represents an arbitrary bond.

$-\beta\phi$ by the bare potential, giving rise to



$$\text{---} = \text{---} \quad (3.41)$$

where

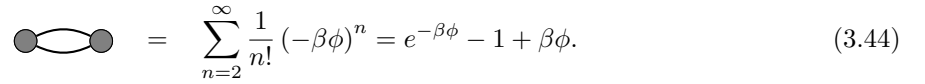


$$\text{---} = \frac{1}{2} \int \mathcal{D}(\mathcal{L}_2) (-\beta V(\mathcal{L}_1, \mathcal{L}_2)) (-\beta\phi(\mathcal{L}_2, \mathcal{L}_1)) z(\mathcal{L}_2) = I_R(\mathcal{L}_1), \quad (3.42)$$

corresponds to all convolutions with at least one intermediate node. The classical estimate for those attached rings is given by

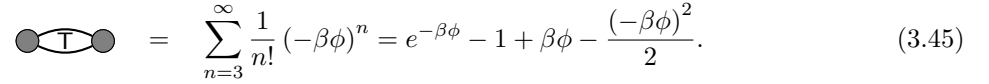
$$I_R(\mathcal{L}) \underset{\text{classic}}{\approx} \frac{e^2 \beta \kappa}{2}. \quad (3.43)$$

Having understood the subtleties arising from the resummation of chain diagrams we can invert the decomposition and collect powers of $-\beta\phi$ in order to form a ‘‘Mayer-like’’ bond. As we have seen, powers of $-\beta\phi$ higher than one are unproblematic when the nodes are not simply connected. We can write



$$\text{---} = \sum_{n=2}^{\infty} \frac{1}{n!} (-\beta\phi)^n = e^{-\beta\phi} - 1 + \beta\phi. \quad (3.44)$$

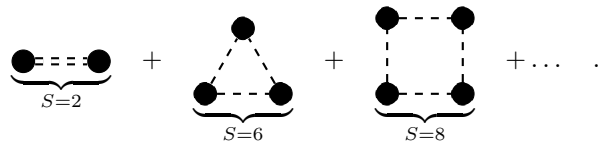
If one node is attached to the rest of the diagram this bond has to be replaced by



$$\text{---} = \sum_{n=3}^{\infty} \frac{1}{n!} (-\beta\phi)^n = e^{-\beta\phi} - 1 + \beta\phi - \frac{(-\beta\phi)^2}{2}. \quad (3.45)$$

to prevent double counting.

The former statements are true for almost all diagrams, but there is one set of diagrams in the whole diagrammatic series of the pressure which is somehow special and needs separate treatment. Namely, it is the set of ‘‘ring’’ diagrams giving rise to the Debye-correction



$$\underbrace{\text{---}}_{S=2} + \underbrace{\text{---}}_{S=6} + \underbrace{\text{---}}_{S=8} + \dots \quad (3.46)$$

In the former considerations we tacitly assumed that we could separate the nodes into two classes: the ‘‘end’’ nodes and those which were intermediate nodes of the convolutions we resummed. This is clearly not the case for the Debye-correction diagrams where an additional rotational symmetry is present leading to a different symmetry factor for each of the diagrams in the set ($S = 2n$ where n is the number of nodes). When replacing the quantum loop potential by the classical Coulomb potential, the value of the

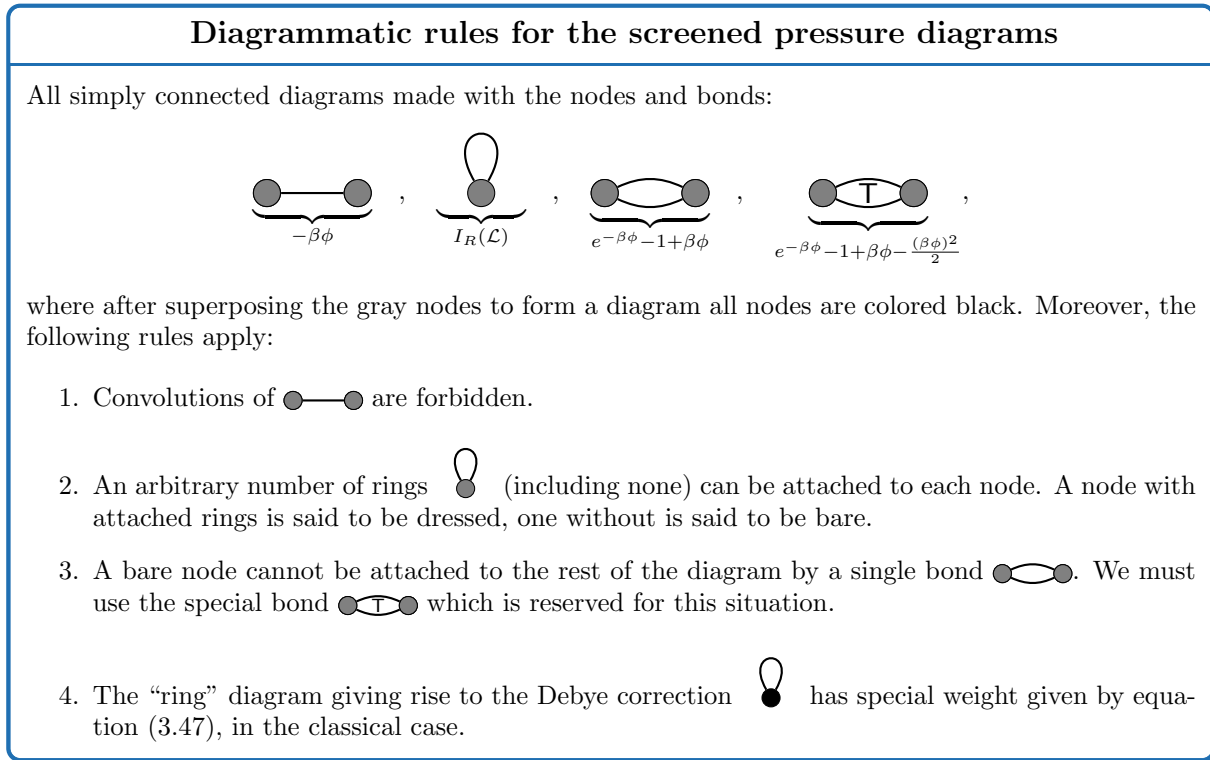


Figure 3.4: Diagrammatic rules for the pressure series

sum of those diagrams is equal to⁵

$$P_{\text{Debye}} = \frac{1}{(2\pi)^3} \int d\mathbf{k} \sum_{n=2}^{\infty} \left(\frac{-\kappa^2}{k^2} \right)^n \frac{1}{2n} = \frac{\kappa^3}{12\pi} \quad \text{with} \quad \kappa = \sqrt{4\pi\beta \sum_i \frac{z_i}{(2\pi\lambda_\gamma^2)^{3/2}} q_i^2}. \quad (3.47)$$

It is important to know that this class of diagrams has to be treated separately. The quantum equivalent of equation (3.47) can be derived in a straightforward manner in Fourier space. However, we only have to concern ourselves with the classical formula (3.47), since it is valid in the parameter regime we consider. We can, thus, conclude that the series of diagrams can be rewritten in terms of the resummed potential where four additional double counting rules have to be taken into account. The rules of the resummed diagrammatic are summarized in figure 3.4.

The diagrammatic series for the densities are then deduced from the pressure diagrams using the relation

$$\rho_\gamma = z_\gamma \frac{\partial \beta P}{\partial z_\gamma}. \quad (3.48)$$

If the bonds did not depend on the fugacities, as is the case for the original Mayer series, the density series would be obtained by successively whitening the black points and keeping only diagrams which are topologically inequivalent. Since the screened potential with which the diagrams are constructed in the resummed pressure series figure 3.4 depends on the fugacities, derivatives acting on the bonds have to be considered, too. The diagrammatic rules to pass from the pressure to the density series are summarized

⁵The complete here presented analysis can be carried out Quantum mechanically. We are, however, mainly concerned with solar conditions, where the classical approximation of the Debye-diagrams is sufficient.

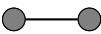
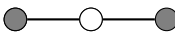



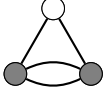
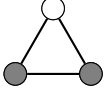

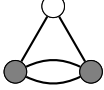

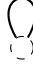
Diagrammatic rules to pass from pressure to densities		
Bond	Description	Derivative
	Replace the bond $-\beta\phi$ by a convolution of two bonds $-\beta\phi$ with an intermediate white point	
	The ring is replaced by a self-convolution with an intermediate white point	
	Replace the bond by $e^{-\beta\phi} - 1$ and add a white point connected to both ends by the bond $-\beta\phi$	 + 
	Replace the bond by $e^{-\beta\phi} - 1 + \beta\phi$ and add a white point connected to both ends by the bond $-\beta\phi$	
	Whiten the black node	

Figure 3.5: Diagrammatic rules for constructing the density series by differentiation of the pressure series

in figure 3.5. Using these rules we recover exactly the same diagrams with the same combinatorial coefficients as Alastuey et al. [34], which confirms the correctness of our considerations. The pressure series defines a model equation of state completely. For our numerical calculations it is advantageous to work with the pressure series and to calculate the densities by taking derivatives.

COMMENT: A particular consequence of these diagrammatic rules is that the convolution of the form

$$\begin{array}{c}
 \text{loop} \\
 | \\
 \bullet \text{---} \bullet \text{---} \bullet
 \end{array}
 \tag{3.49}$$

is allowed. Therefore, the chain resummation has not achieved that convolution diagrams are absent in the series but it only assures the integrability of the appearing cluster coefficients. First we briefly summarize the properties of the resummed potential first calculated by Ballenegger et al. [50].

3.4.2 The screened loop-loop potential

The calculation of the resummed loop-loop potential is presented in Ref. [50] in its full length. Since the resummed potential is a convolution of terms we can Fourier transform the quantum equivalent of equation (3.33). Quantum mechanics solely enters by considering the nodes to be made of loops and by replacing the classical Coulomb potential by the loop-loop potential equation (3.10). Convolutions become,

as for classical interactions, simple multiplications of Fourier transformed potentials. The simultaneity condition of the bare loop-loop potential can be represented by introducing its spectral decomposition $\tilde{\delta}(s_1 - s_2) = \sum_n e^{2\pi i n(s_1 - s_2)}$. After a few manipulations using the time-translational invariance of the Brownian bridges, terms with different n 's decouple. The resummation of all chains with fixed n can be carried out and we can back transform from (\mathbf{k}, s) -space to get

$$\phi(\mathbf{r}_1, \mathbf{r}_2, \boldsymbol{\eta}_1, \boldsymbol{\eta}_2) = e_{\gamma_1} e_{\gamma_2} \int_0^{q_1} ds_1 \int_0^{q_2} ds_2 \int d\mathbf{k} e^{i\mathbf{k}(\mathbf{r}_1 + \lambda_1 \boldsymbol{\eta}_1(s_1) - \mathbf{r}_2 - \lambda_2 \boldsymbol{\eta}_2(s_2))} \dots$$

$$\sum_{n=0}^{\infty} \frac{4\pi}{k^2 + \kappa^2(n, k)} e^{2\pi i n(s_1 - s_2)} \quad (3.50)$$

$$\text{with} \quad \kappa^2(k, n) = 4\pi\beta \sum_{\gamma=\{e,p,\alpha\}} e_{\gamma}^2 \sum_{q=0}^{\infty} q \int_0^q ds \int \mathcal{D}_q(\boldsymbol{\eta}) z_{\gamma}(\boldsymbol{\eta}) e^{i\lambda_{\gamma} \mathbf{k} \boldsymbol{\eta}(s) - 2\pi i s n}. \quad (3.51)$$

We would like to discuss the above equation to gain more insight into this fairly complicated formula (This screened potential will be further studied in section §4.2). First, we can recover the classical Debye potential by taking the limit $\lambda_{\gamma} \rightarrow 0$ first for the particles in the chain

$$\lim_{\lambda \rightarrow 0} \kappa^2(\mathbf{k}, 0) = \kappa^2 \quad (3.52)$$

$$\lim_{\lambda \rightarrow 0} \kappa^2(\mathbf{k}, n \neq 0) = 0.$$

Using the above limits we derive the semi-classical approximation

$$\phi_{sc}(\mathbf{r}_1, \mathbf{r}_2, \boldsymbol{\eta}_1, \boldsymbol{\eta}_2) \approx e_{\gamma_1} e_{\gamma_2} \int_0^{q_1} ds_1 \int_0^{q_2} ds_2 \left[\frac{e^{-\kappa |\mathbf{r}_1 + \lambda_1 \boldsymbol{\eta}_1(s_1) - \mathbf{r}_2 - \lambda_2 \boldsymbol{\eta}_2(s_2)|}}{|\mathbf{r}_1 + \lambda_1 \boldsymbol{\eta}_1(s_1) - \mathbf{r}_2 - \lambda_2 \boldsymbol{\eta}_2(s_2)|} \right. \quad (3.53)$$

$$\left. - \frac{1}{|\mathbf{r}_1 + \lambda_1 \boldsymbol{\eta}_1(s_1) - \mathbf{r}_2 - \lambda_2 \boldsymbol{\eta}_2(s_2)|} + \underbrace{\frac{1}{|\mathbf{r}_1 + \lambda_1 \boldsymbol{\eta}_1(s_1) - \mathbf{r}_2 - \lambda_2 \boldsymbol{\eta}_2(s_2)|} \tilde{\delta}(s_1, s_2)}_{\text{equal times}} \right],$$

where all loops in the chains are classical ($\lambda = 0$) but the external loops do still have finite extensions. Taking the outer loops to be classical too, by setting $\xi_i = 0$, the last two terms cancel each other and the first term reduces to the standard formula, so that we recover the Debye potential. The last two terms in equation (3.53) lead to an algebraic decay ($\sim 1/r^6$) of the potential at large distances. If we further expand the approximation equation (3.53) for short distances we do find that it reduces to the bare Coulomb interaction shifted by κ

$$\phi(\mathbf{r}_1, \mathbf{r}_2, \boldsymbol{\eta}_1, \boldsymbol{\eta}_2) \approx e_{\gamma_1} e_{\gamma_2} \int_0^{q_1} ds_1 \int_0^{q_2} ds_2 \frac{1}{|\mathbf{r}_1 + \lambda_1 \boldsymbol{\eta}_1(s_1) - \mathbf{r}_2 - \lambda_2 \boldsymbol{\eta}_2(s_2)|} \tilde{\delta}(s_1 - s_2) - e_{\gamma_1} e_{\gamma_2} \kappa. \quad (3.54)$$

It is this shift of κ which will generate the first order correction to the Ground state of a few-particle cluster, due to collective effects. At short distances the quantum loop-loop potential reduces to the bare loop-loop potential since

$$\lim_{|\mathbf{k}| \rightarrow \infty} \frac{4\pi}{k^2 + \kappa(k, n)} \approx \frac{4\pi}{k^2} \quad (3.55)$$

only the first order term in the resummed quantum potential (3.38), which represents the direct interaction of the particles, survives

$$\lim_{\mathbf{k} \rightarrow \infty} \phi(\mathbf{r}_1, \mathbf{r}_2, \boldsymbol{\eta}_1, \boldsymbol{\eta}_2) \sim e_{\gamma_1} e_{\gamma_2} \int_0^{q_1} ds_1 \int_0^{q_2} ds_2 \int d\mathbf{k} e^{i\mathbf{k}(\mathbf{r}_1 + \lambda_1 \boldsymbol{\eta}_1(s_1) - \mathbf{r}_2 - \lambda_2 \boldsymbol{\eta}_2(s_2))} \frac{4\pi}{k^2} \tilde{\delta}(s_1 - s_2) \quad (3.56)$$

$$= V(\mathcal{L}_1, \mathcal{L}_2). \quad (3.57)$$

Since we want to use numerical methods to calculate the cluster integrals we need to have a potential which is easy to be evaluated. In practice, double time integration is not feasible in numerical calculations where the path discretization easily reaches 400 discretization points. We have, thus, decided to use a further simplified loop-loop potential which meets all important limits, as discussed in the above text

$$\phi_\kappa(\mathbf{r}_1, \mathbf{r}_2, \boldsymbol{\eta}_1, \boldsymbol{\eta}_2) = e_{\gamma_1} e_{\gamma_2} \int_0^{q_1} ds_1 \int_0^{q_2} ds_2 \frac{e^{-\kappa|\mathbf{r}_1 + \lambda_1 \boldsymbol{\eta}_1(s_1) - \mathbf{r}_2 - \lambda_2 \boldsymbol{\eta}_2(s_2)|}}{|\mathbf{r}_1 + \lambda_1 \boldsymbol{\eta}_1(s_1) - \mathbf{r}_2 - \lambda_2 \boldsymbol{\eta}_2(s_2)|} \tilde{\delta}(s_1, s_2). \quad (3.58)$$

For short distances we do recover the shift of κ together with the bare loop-loop potential. At large distances the potential decays exponentially. By using the approximate potential (3.58) we neglect the algebraic tails present in formula (3.53). These tail corrections of the potential will not have influence on the Ground state terms, which are dominant at low temperatures, and thus we expect the approximation to give good results. In chapter 4 we will more closely investigate the accuracy of this approximation to the loop-loop potential, by comparing it to the calculation with full double-time dependence.

3.5 Neutrality and the truncated fugacity series

The charge neutrality is an essential aspect of the physical system at equilibrium. In absence of an external field a plasma in thermal equilibrium does always fulfill the charge neutrality in the Grand canonical ensemble

$$\sum_{\gamma} e_{\gamma} \rho_{\gamma} = 0, \quad (3.59)$$

which is highly non-trivial and one of the highlights of the Lieb-Lebowitz theorem [11, 46]. When selecting a certain set of diagrams neutrality is not automatically assured and, thus, we have to review which selections of diagrams do fulfill the neutrality condition. In the following, we will see how this translates down to the level of fugacities z_{γ} and diagrams. For the ideal gas the neutrality condition imposed on the level of densities is equivalent to imposing it on the level of fugacities

$$\sum_{\gamma} e_{\gamma} \tilde{z}_{\gamma} = 0 \quad \text{where} \quad \tilde{z}_{\gamma} = \frac{(2\sigma_{\gamma} + 1) z_{\gamma}}{(2\pi \lambda_{\gamma}^2)^{3/2}}, \quad (3.60)$$

since $\rho_\gamma = \tilde{z}_\gamma$ applies when all interactions are neglected. In order to understand the mechanism yielding a neutral system we imagine a charged particle cluster⁶ interacting with the surrounding free particles

$$P_{\mathcal{G}_{\text{dressed}}} = \text{Diagram} \quad (3.61)$$

Diagrams of such a topology are naturally present in the series of Mayer diagrams for the pressure. If we pass to the density series we have to color nodes white and attach a specific species. The contribution to the densities ρ_e, ρ_p and ρ_α arising from the diagram \mathcal{G} are⁷

$$\begin{aligned} \rho_{\mathcal{G}_{\text{dressed},e}} &= \text{Diagram 1} + \text{Diagram 2} \\ \rho_{\mathcal{G}_{\text{dressed},p}} &= \text{Diagram 3} \\ \rho_{\mathcal{G}_{\text{dressed},\alpha}} &= \text{Diagram 4} \end{aligned} \quad (3.62)$$

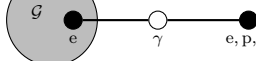
The integration over the attached particle has the classical estimate

$$\text{Diagram} = -\beta e_\gamma e_i \tilde{z}_\gamma \int d\mathbf{r} \frac{e^{-\kappa r}}{r} = -\frac{4\pi\beta e_\gamma e_i \tilde{z}_\gamma}{\kappa^2} = -e_\gamma e_i \frac{\tilde{z}_\gamma}{\sum_j e_j^2 \tilde{z}_j} \quad (3.63)$$

This relation is also verified when using the quantum potential $-\beta\phi$ since the temporal structure of the quantum potential is of no importance [50]⁸. We find that the contributions to the respective densities are thus

$$\begin{aligned} \rho_{\mathcal{G}_{\text{dressed},e}} &= \text{Diagram 1} \cdot \underbrace{\left(-\sum_\gamma e_\gamma e_e \frac{\tilde{z}_\gamma}{\sum_j e_j^2 \tilde{z}_j} \right)}_{=0 \text{ due to } \sum e_\gamma \tilde{z}_\gamma = 0} + \text{Diagram 2} \cdot \left(-e_e^2 \frac{\tilde{z}_e}{\sum_j e_j^2 \tilde{z}_j} \right) \\ \rho_{\mathcal{G}_{\text{dressed},p}} &= \text{Diagram 3} \cdot \left(-e_p e_e \frac{\tilde{z}_p}{\sum_j e_j^2 \tilde{z}_j} \right) \\ \rho_{\mathcal{G}_{\text{dressed},\alpha}} &= \text{Diagram 4} \cdot \left(-e_\alpha e_e \frac{\tilde{z}_\alpha}{\sum_j e_j^2 \tilde{z}_j} \right), \end{aligned} \quad (3.64)$$

⁶Here a particle cluster is an arbitrary diagram permitted by the diagrammatic rules for the pressure 3.4

⁷The diagrams originating from the derivative acting on the bond  do vanish after imposing

the pseudo-neutrality, equation (3.60).

⁸The fictitious time s for which the interaction between the particles takes place, can be taken $s = 0$ by time-rotational symmetry of the attached loop. The result of the integration is shape-independent and hereby classical.

so that the contribution to the charge density becomes

$$\begin{aligned}
 \sum_{\gamma} e_{\gamma} \rho_{\mathcal{G}_{\text{dressed},\gamma}} &= \left(\text{Diagram: Circle } \mathcal{G} \text{ with a black dot } e \text{ inside} \right) \cdot \sum_{\gamma} e_{\gamma} \left(-e_{\gamma} e_e \frac{\tilde{z}_{\gamma}}{\sum_j e_j^2 z_j} \right) \\
 &= -e_e \left(\text{Diagram: Circle } \mathcal{G} \text{ with a black dot } e \text{ inside} \right).
 \end{aligned} \tag{3.65}$$

This cancels exactly the contribution

$$e_e \rho_{\mathcal{G},e} = e_e \left(\text{Diagram: Circle } \mathcal{G} \text{ with a white dot } e \text{ inside} \right), \tag{3.66}$$

of the bare diagram associated to the dressed diagram that appears in equation (3.61). Therefore, the sum of the bare and the dressed diagrams in the pressure series

$$P_{\mathcal{G}} = \left(\text{Diagram: Circle } \mathcal{G} \text{ with a black dot } e \text{ inside} \right) + \left(\text{Diagram: Circle } \mathcal{G} \text{ with a black dot } e \text{ inside, connected to a black dot } e, p, \alpha \text{ outside} \right) \tag{3.67}$$

leads to particle densities fulfilling the neutrality condition.

Consequently, we conclude that each node z_{γ} in a diagram has to be dressed with a neutrality bond in order to guarantee neutrality. Since the screened cluster functions do depend on κ and thereby on the fugacities z_{γ} , also those should be dressed in order to assure neutrality. It is important to recognize that the second diagram in equation (3.67) is actually zero when applying the neutrality in the pressure series. Nevertheless, the dressed diagrams generate important contributions in the density series, assuring neutrality of the system. The selection of diagrams being neutral for all choices of the fugacities allows us to impose the pseudo-neutrality condition

$$\sum_{\gamma} e_{\gamma} \frac{(2\sigma_{\gamma} + 1)z_{\gamma}}{(2\pi\lambda_{\gamma}^2)^{3/2}} = 0, \tag{3.68}$$

without loss of generality. Due to the interdependence of the fugacities (3.68) the number of degrees of freedom z_{γ} that have to be considered is reduced by one, in agreement with the Lieb-Lebowitz theorem [11]. We have thus seen that, when starting from the pressure series, we should take the neutrality condition into account only **after** we have first dressed all fugacity factors by the neutrality bond and afterwards deduced the related density series.

3.6 Definition of the κ dependent cluster functions

The resummation procedure led to two changes in the diagrammatic series for the pressure: the replacement of the bare Coulomb potential by an integrable loop-loop potential and the need to introduce double counting rules suppressing convolutions of the new resummed bond. The two particle cluster

function (the equivalent of the second virial coefficient) is, therefore, given by

$$\mathcal{G}_2 = \frac{1}{2} \text{Diagram} \tag{3.69}$$

The truncation (3.69) arises completely naturally and, thus, this object is exactly the one appearing in the resummed pressure series. At large distances the cluster behaves as $1/r^3$ giving rise to a logarithmic dependence on κ . In the case that the two particle system develops a bound state, this logarithmic dependence on κ will become invisible for sufficiently low temperatures, for the value of the integral being dominated by this bound state. The three-particle cluster function is given by

$$\mathcal{G}_3 = \frac{1}{6} \left(\text{Diagram 1} + \text{Diagram 2} + \text{Diagram 3} + \text{Diagram 4} + \text{Diagram 5} + \text{Diagram 6} + \text{Diagram 7} + \text{Diagram 8} \right) \tag{3.70}$$

In formula (3.70) no convolutions of $-\beta\phi$ are present due to the diagrammatic rules listed in figure 3.4. Analyzing the large-distance behavior of the three particle cluster function as given in equation (3.70) we recognize that the diagrams of the form

$$\text{Diagram} \tag{3.71}$$

will result in a contribution proportional to β^5/κ . This is numerically not desirable, since the integration routine would spend too much effort sampling paths at large distances and will not concentrate on the short distance bound states. In the case of a symmetric plasma as, for example, the pure Hydrogen plasma, contributions coming from different particle clusters will cancel out, so that the overall contribution to the equation of state of this diagram is zero. Therefore, we have decided to subtract these diagrams from the three particle cluster (3.70). It is important to remark that the subtracted diagrams (3.71) do not contain any exponential terms and, thus, do not alter the low-temperature asymptotic of the cluster function. In this way the large-distance behavior of the three particle cluster function gives only rise to logarithmic, numerically treatable, corrections as for the two particle cluster. In the two particle case these logarithmic corrections are assessable easily, whereas in the three particle case the situation is more involved as also atom-charge interactions are involved.

The dressing with attached loops gives an important contribution because it compensates the first order correction in κ of the ground state energy, in the case of a neutral cluster (see chapter 4). All

particles present in the cluster functions are thus automatically “dressed” if not indicated otherwise

$$\begin{array}{ccccccc}
 \bullet & \xrightarrow{\text{dressing}} & \bullet & + & \underbrace{\begin{array}{c} \bullet \\ \text{---} \end{array}}_{\bullet \cdot e^{I_R}} & + & \dots \\
 & & & & \begin{array}{c} \bullet \\ \text{---} \end{array} & + & \begin{array}{c} \bullet \\ \text{---} \end{array} & + & \begin{array}{c} \bullet \\ \text{---} \end{array} & + & \dots
 \end{array}
 \tag{3.72}$$

which using the classical approximation is a simple multiplication with the factor $\exp(I_R) \approx \exp(\beta e_\gamma^2 \kappa / 2)$. The shorthand notation $\bullet \circlearrowleft = z (e^{I_R} - 1)$ represents the sum of all diagrams for which at least one ring is attached to the node.

Chapter 4

Physical implications of the screened potential

4.1 Physical effects of the resummation

The resummation of RPA-like chains has led to two main changes in the diagrammatic series. The most obvious effect is the replacement of the bare Coulomb potential containing a temporal delta function by the screened potential (3.50) which shows a non-trivial time dependence. The second effect, which seems less important at first glance, is the appearance of the dressing of fugacity factors by the additional bonds

$$\text{⦿} = \frac{1}{2} \int \mathcal{D}(\mathcal{L}_2) (-\beta e_1 e_2 V(\mathcal{L}_1, \mathcal{L}_2)) (-\beta e_1 e_2 \phi(\mathcal{L}_2, \mathcal{L}_1)) z(\mathcal{L}_2) = I_R(\mathcal{L}_1) \approx \frac{e^2 \beta \kappa}{2}. \quad (4.1)$$

Due to the theoretical rigorousness of the physical picture and the related diagrammatic expansion, we will see that we are able to answer the question of how the screened potential influences the cluster functions and, even more importantly, how it affects the ground state energies. To be more precise we will answer the question which weight (ground state energy) of the particle clusters should be taken in either the chemical picture or in a fugacity expansion method when the particle clusters are approximated by their ground state energies. In Ref. [51] it is argued, for example, that the ground state energies appearing in the free energy F should be the bare ones. The main argument is that in order for the potential between two particles to be screened, the density of particles in-between them should be significant, so that they are able to react dynamically and polarize according to the motion of the two particles. This reasoning is insufficient in the sense that the Coulomb potential is long-ranged. It is not only the density in-between but also the density around them which statistically counteracts the motion of the two basic constituents.

In the following, we argue that the ground state energies are changed by polarization effects implemented in the resummed potential, while at the same time the diagrammatic double counting rules lead to a compensation of these energy corrections for neutral-particle clusters. This is physically intuitive since the ground state wave function of a few-particle cluster lives on a length scale $\sim a_0$. A charged particle in the plasma induces a oppositely charged cloud of particles around it, whose size is given by the length scale $\sim \kappa$. If the screening length $\kappa^{-1} > a_0$ is larger than the length scale of the cluster, thus it appears to the surrounding medium to have an effective charge $\sum_i q_i$. If this effective charge is zero,

we expect no static effect of the plasma on the few particle cluster, so that the first corrections (the shift of the ground state energies) are zero. On the other hand, in the case of a charged cluster the static corrections are of importance as the plasma reacts to this overall charge. We will first present a precise estimation of this compensation in the case of the Hydrogen cluster function and afterwards prove the statement that neutral cluster weights are unaffected by the screening effects.

Weight of the Hydrogen cluster in a particle bath

In several articles (see for example Ref. [22]) it is stated that the low-lying bound states are unaffected when replacing the bare Coulomb potential by a statically screened one. By inspecting the resummed diagrammatic we find on the contrary, that the correction of the ground state energy is essential and that it is only thanks to cancellations of terms that the statement holds at leading order. For the Hydrogen cluster the correction of the ground state is given at leading order in κ , by

$$\Delta E_0 = \int d\mathbf{r} |\psi_0(\mathbf{r})|^2 \left(\frac{e_1 e_2 e^{-\kappa r}}{r} - \frac{e_1 e_2}{r} \right) \approx -e_1 e_2 \kappa, \quad (4.2)$$

so that the partition function at low temperatures can be approximated by

$$Z_H = \text{diagram} \approx e^{-\beta(E_0 + \Delta E_0)} = e^{-\beta(E_0 + e^2 \beta \kappa)}. \quad (4.3)$$

The additional diagrams where rings are attached to the basic cluster

$$\text{diagram}_1 \quad \text{diagram}_2 \quad \text{diagram}_3 \quad \text{diagram}_4 \quad \dots \quad (4.4)$$

are as well present in the diagrammatic series and have same weight, which is given by (4.3) at low temperatures, besides a multiplicative factor arising from the attached rings. Since an infinite number of rings can be attached to each of the two cluster particles, these rings contribute a multiplicative factor of

$$\left(\sum_{n=0}^{\infty} \frac{I_R^n}{n!} \right)^2 = \exp(I_R)^2 \approx \exp\left(\frac{e^2 \beta \kappa}{2}\right), \quad (4.5)$$

where the factor $n!$ accounts for the indistinguishableness of the n rings, which can be attached to each node. Thus, the sum of the former diagrams cancel exactly the first order perturbative correction to the ground state energy and the approximate low-temperature cluster function becomes

$$\mathcal{C}_H \approx e^{-\beta(E_H + e^2 \beta \kappa)} \underbrace{e^{e^2 \beta \kappa}}_{\text{attached rings}} = e^{\beta E_H}, \quad (4.6)$$

confirming the above statement that low-lying states are effectively unaffected. It is important to keep this cancellation in mind when selecting diagrams since it would be incorrect to take the attached rings into account while using a κ -independent cluster function. We note that κ -independent cluster functions are used in the SLT-expansion of the equation of state, but this cancellation has been accounted for in Alastuey and Ballenegger [13] as all contributions at given order in the low-temperature low-density limit have been collected consistently. The latter analysis shows that the first order correction of the ground state of Hydrogen induced by κ gets effectively canceled. It is relevant to state that this cancellation is

incomplete for non-neutral cluster functions. The former analysis can be generalized to show that, at leading order, neutral cluster weights are unaffected by the surrounding plasma.

Weight of an arbitrary few-particle cluster

The first order perturbation of the ground state energy of an arbitrary cluster \mathcal{C} of N particles has the form

$$\delta E = \int d\{\mathbf{r}\} |\psi(\{\mathbf{r}\})|^2 \sum_{i<j} (\phi(\mathbf{r}_i, \mathbf{r}_j) - V(\mathbf{r}_i, \mathbf{r}_j)) \underset{O(\kappa)}{=} - \sum_{i<j} e_i e_j \kappa. \quad (4.7)$$

where we assume a scale separation $a_0 \ll \kappa^{-1}$, so that after developing the difference of the potentials the integration over the wave function yields unity. The attached rings on each of the particles, on the other hand, give a factor

$$\exp\left(\beta \sum_i \frac{e_i^2 \kappa}{2}\right), \quad (4.8)$$

so that the effective cluster weight, where all fugacity factors are dressed by attached rings, becomes

$$Z_N = \exp\left(-\beta E_0 + \underbrace{\beta \sum_{i<j} e_i e_j \kappa}_{\text{GS correction}} + \underbrace{\beta \sum_i \frac{e_i^2 \kappa}{2}}_{\text{attached rings}}\right). \quad (4.9)$$

The two sums can be easily manipulated to show that neutral clusters $\sum_i e_i = 0$ are unaffected by the static first order correction

$$\frac{1}{2} \sum_i e_i^2 + \sum_{i<j} e_i e_j = \frac{1}{2} \sum_i e_i^2 + \frac{1}{2} \sum_{i \neq j} e_i e_j = \frac{1}{2} \sum_{i,j} e_i e_j = \frac{1}{2} \left(\sum_i e_i\right)^2. \quad (4.10)$$

In the case of a neutral cluster the first order correction cancels out, whereas for non-neutral constituents the screening has the expected effect on the cluster weight. Interestingly, the effective correction $\exp\left(\frac{\beta \kappa}{2} (\sum_i e_i)^2\right)$ has the form of a ring attached to an effective particle with charge $\sum_i e_i$, which confirms our physical intuition. The above statements hold also in the case of the full resummed potential (and not only for its Debye version) due to the staticness of the first order correction. To see this, we remember that the integral related to the attached rings can be rewritten

$$\frac{\beta^2}{2} \int d\mathbf{r} V(\mathbf{0}\mathcal{L}, \mathbf{r}\mathcal{L}) \phi(\mathbf{0}\mathcal{L}, \mathbf{r}, \mathcal{L}) z(\mathcal{L}) = -\frac{\beta}{2} \lim_{\mathbf{r} \rightarrow 0} (\phi(\mathbf{0}\mathcal{L}, \mathbf{r}\mathcal{L}) - V(\mathbf{0}\mathcal{L}, \mathbf{r}\mathcal{L})). \quad (4.11)$$

This makes the similarity with equation (4.7) clear and, thus, confirms that the former statements also hold in the case of the full resummed potential (3.50). It is important to emphasize that the former analysis does only hold for the first order correction of the ground state energy. The κ -dependence of the cluster function as a whole will be of major relevance at high temperatures where the cluster function cannot be approximated by its ground state contribution, as the scale separation $a_0 < \kappa^{-1}$ is of less importance in this case. As former considerations are based on the scale separation $a_0 < \kappa^{-1}$ they lose their validity if this condition is not fulfilled. This is the case for a many-body cluster having a spatially

extended ground state for which the inherent length scale is larger the screening length κ^{-1} . Since we are mainly interested in the application of the theory for fairly low densities these special cases are of no concern. Furthermore, we will use the full numerically calculated cluster function and not its ground state approximation in our calculation of the equation of state, so that even if those effects would be present they would be taken into account naturally.

4.2 Numerical calculation of the resummed potential

In order to verify that the effective potential we are using for the computation of the Cluster functions is adequate we numerically calculate the exact resummed potential and compare with our approximation. The resummed potential ϕ is given in terms of a Fourier-series in both, the reciprocal space \mathbf{k} and an auxiliary variable n which is the conjugate variable of the time s (see equation (3.50) on page 34 and Ref. [50]). This formulation is not appropriate for numerical evaluation and, thus, we have to find a description that allows for numerical evaluation. Much in the spirit of the RPA-resummation, giving rise to the Debye potential in Condensed matter physics, we write down a self-consistency equation, which is fulfilled by the resummed time-dependent loop-loop potential. Beyond doubt we can assume that exchange effects in the intermediate loops will be of minor importance and, thus, we fix the number of particles in the loops to $q = 1$. Graphically the self-consistency equation can be visualized as

or written in mathematical terms¹

$$\phi(\mathcal{L}_1, \mathcal{L}_2, s_1, s_2) = V(\mathcal{L}_1, \mathcal{L}_2, s_1, s_2) - \frac{\kappa^2}{4\pi} \int \mathcal{D}(\mathcal{L}_3) \int ds_3 \int ds_4 V(\mathcal{L}_1, \mathcal{L}_3, s_1, s_3) \phi(\mathcal{L}_3, \mathcal{L}_2, s_4, s_2). \quad (4.13)$$

The Fourier-transformation of this expression reads more compactly

$$\phi(\mathbf{k}, s_1, s_2) = V(\mathbf{k})\delta_{s_1, s_2} - \frac{\kappa^2}{4\pi} \int \mathcal{D}(\mathcal{L}_3) \int ds_3 \int ds_4 V(\mathbf{k})\delta_{s_1, s_3} \phi(\mathbf{k}, s_4, s_2) e^{i\lambda\mathbf{k}(\xi_3(s_3) - \xi_3(s_4))} \quad (4.14)$$

$$\phi(\mathbf{k}, s_1, s_2) = V(\mathbf{k})\delta_{s_1, s_2} - \frac{\kappa^2}{4\pi} \int ds_4 V(\mathbf{k})\phi(\mathbf{k}, s_4, s_2) \underbrace{e^{-\mathbf{k}^2 \lambda^2 (g_{s_1, s_1} + g_{s_4, s_4} - 2g_{s_1, s_4})}}_{T(\mathbf{k}, s_1, s_4)}, \quad (4.15)$$

where $g_{s,t} = \min(s, t)(1 - \max(s, t))$ is the Greens function of the operator $\frac{\partial^2}{\partial s^2}$

$$\frac{\partial^2}{\partial s^2} g_{s,t} = \delta_{s,t} \quad (4.16)$$

with the Dirichlet boundary conditions $g_{0,0} = g_{1,1} = 0$.

As the term $VT\phi$ is of convolution type in the time variables, we could Fourier transform to find the result given in Ref. [50] The above equation completely determines the function $\phi(\mathbf{k}, s_1, s_2)$ and can be

¹Numerical prefactors of $e_{\gamma_1} e_{\gamma_2}$ are absorbed in the definitions of the potentials in this section, to lighten the nomenclature.

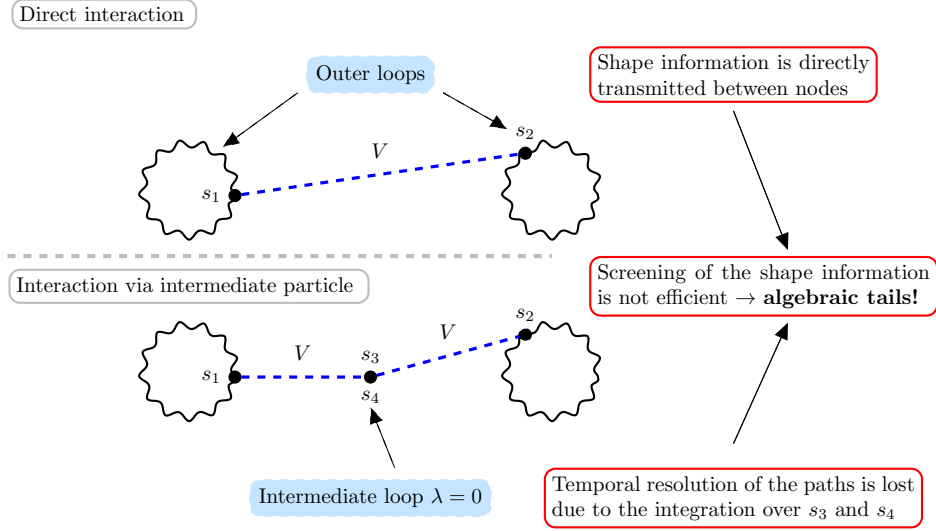


Figure 4.1: The algebraic tail are directly related to the shape of the **outer** particle paths. Due to the intermediate particles in the chains, this shape information is lost in higher order diagrams (chains involving at least one intermediate particle). The screening is not effective, since the contribution of the direct interaction diagram cannot be compensated by the higher order diagrams. Only the monopole part of the loop-loop interaction, *i.e.* the shape independent modes $n = 0$ in formula (3.50), are screened exponentially.

solved numerically. To do so, we discretize the integral equation and solve the related matrix-equation for each \mathbf{k} numerically (we have $N - 1$ summation terms since $\phi_{s,t} = \phi_{s,t+1} = \phi_{s+1,t}$ and the boundary terms of the discretized integral are appearing with a prefactor of $\frac{1}{2}$ (Trapezoidal rule)):

$$\phi_{s_1, s_2}(\mathbf{k}) = V(\mathbf{k})\delta_{s_1, s_2} - \kappa^2 V(\mathbf{k}) \frac{1}{N+1} \sum_{t=0}^{N-1} \mathbf{T}_{s_1, t}(\mathbf{k}) \phi_{t, s_2}(\mathbf{k}) \quad (4.17)$$

Due to the time rotational symmetry we can further simplify to

$$\phi_s(\mathbf{k}) = V(\mathbf{k}) \left(\delta_{s,0} - \frac{\kappa^2}{4\pi} \frac{1}{N+1} \sum_{t=0}^{N-1} \mathbf{T}_{s,t}(\mathbf{k}) \phi_t(\mathbf{k}) \right). \quad (4.18)$$

This matrix-equation can be solved numerically for each $|\mathbf{k}|$ yielding the resummed potential. We could also iterate the matrix-equation, which turns out to converge only if $\kappa^2/k^2 < 1$ since the related series is geometric. It is well known that

$$y = \sum_{n=0}^{\infty} c(-cx)^n = \frac{c}{1+cx} \quad \text{solves} \quad y = c - cy \quad (4.19)$$

even though the series converges only for $|cx| < 1$. The same happens when trying to iterate the matrix equation: The series does not converge even though a solution of the self-consistency equation exists. For $\lambda \rightarrow 0$ the transition matrix becomes independent of the times and we obtain:

$$\phi_{sc}(\mathbf{k}, s_1, s_2) = V(\mathbf{k})\delta_{s_1, s_2} - \frac{\kappa^2}{4\pi} V(\mathbf{k}) \int dt \phi_{sc}(\mathbf{k}, t, s_2). \quad (4.20)$$

We can actually show that this equation is solved by the potential:

$$\phi_{\text{sc}}(\mathbf{k}, s_1, s_2) = \frac{4\pi}{k^2} \delta_{s_1, s_2} - \frac{\kappa^2}{k^2} \frac{4\pi}{k^2 + \kappa^2} \quad (4.21)$$

which re-transformed to ξ, r -space

$$\phi_{\text{sc}}(r_1, \xi_1, r_2, \xi_2, s_1, s_2) = \frac{\exp(-\kappa |r_1 + \lambda \xi(s_1) - r_2 - \lambda \xi(s_2)|) - 1}{|r_1 + \lambda \xi(s_1) - r_2 - \lambda \xi(s_2)|} + \frac{1}{|r_1 + \lambda \xi(s_1) - r_2 - \lambda \xi(s_2)|} \delta_{s_1, s_2} \quad (4.22)$$

yields the term dominant, in the limit $\kappa \rightarrow 0$ [50]. The semi-classical approximation (4.22) shows a special feature of the full quantum resummation, which, in contrast to the usual exponential decay of the Debye-potential, are the algebraic tails of the potential. These algebraic corrections to the Debye potential are related to the fact that by the additional time dimension² of the intermediate loops the shape information of the two interacting loops is smeared out, leading to less effective screening (see figure 4.1). The approximation used in the current implementation is

$$\phi_{\kappa}(\mathbf{k}, s_1, s_2) = \frac{4\pi}{k^2 + \kappa^2} \delta_{s_1, s_2} \quad (4.23)$$

whose Fourier-transform is equal to

$$\phi_{\kappa}(r_1, \xi_1, s_1, r_2, \xi_2, s_2) = \frac{\exp(-\kappa |r_1 + \lambda \xi(s_1) - r_2 - \lambda \xi(s_2)|)}{|r_1 + \lambda \xi(s_1) - r_2 - \lambda \xi(s_2)|} \delta_{s_1, s_2}. \quad (4.24)$$

To check whether the approximation used for the numerical computation of the cluster functions is good, we compare the exact solution of the discretized integral equation with the semi-classical approximation. For this purpose we calculate

$$\epsilon(|k|, s) = \phi_{\text{num}}(|k|, s) - \underbrace{\left(\frac{4\pi}{k^2} \delta_{s,0} - \frac{1}{\Delta s} \frac{4\pi}{k^2} \frac{\kappa^2}{k^2 + \kappa^2} \right)}_{\phi_{\text{sc}}} \quad (4.25)$$

the difference of $\phi_{\text{num}}(s)$, the numerically calculated solution of the integral equation (4.18), and the semi-classical approximation (see equation (4.21))³. The difference of the numerical result and the semi-classical approximation should be compared to the bare Coulomb potential, thus we plot $\frac{\epsilon(s)}{4\pi/k^2}$.

In this way the curves shown in figure 4.2 can be interpreted as the strength of these correction terms with respect to the Coulomb potential. We can see that the magnitude of those terms is negligible in the range of parameters realized in the Sun ($\kappa a_0 < 10^{-1}$). Only if $\lambda \kappa$ is large the diffraction effects are not negligible, even at large distances ($k \rightarrow 0$). Based on these considerations the use of the approximation ϕ_{κ} for the calculation of the cluster functions is justified, at least when considering solar conditions. Since the low density approximation still involves an integration over two times, which is numerically expensive, we want to go even one step further. The difference of the two potentials ϕ_{κ} and ϕ_{sc} can easily be seen to be controlled by dimensionless parameter $\lambda \kappa$ when considering their Fourier transformations (equations (4.24) and (4.22)). By symmetry the first order corrections do vanish when integrating over the shapes of the external loops if no further correlations are involved, so that the first corrective terms

²The extension of the path is not necessary since the algebraic tails survive the $\lambda \rightarrow 0$ limit

³The factor $1/\Delta s$ has to be introduced due to the discrete nature of the ϕ_{num} (ds becomes $\frac{1}{\Delta s}$ when discretizing an integral)

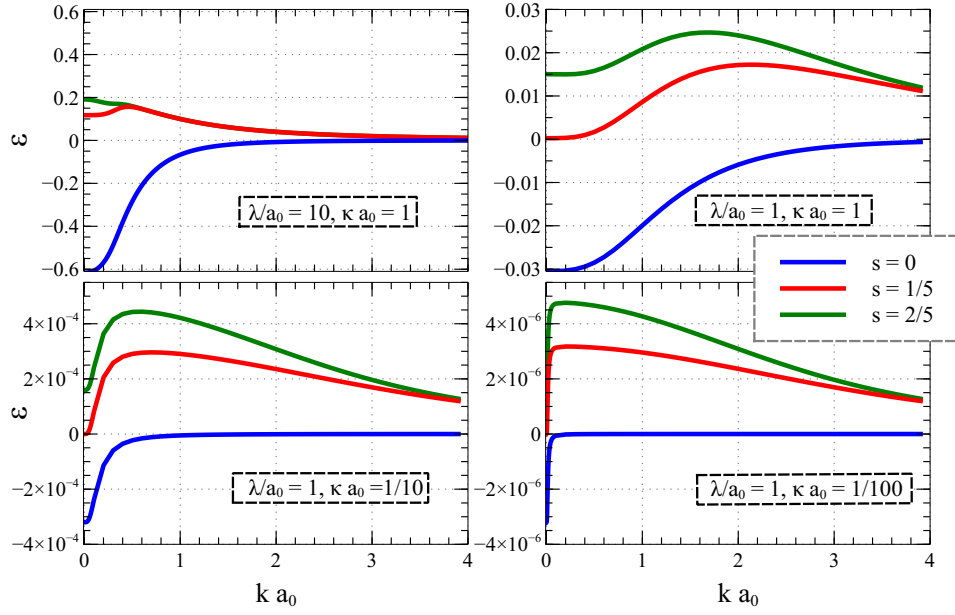


Figure 4.2: The quantity $\frac{\epsilon(s)}{4\pi/k^2}$ for different choices of λ and κ . The magnitude can be identified with the strength of those correction terms with respect to the Coulomb potential. Therefore, we conclude that for the adiabat of the Sun these λ -dependent corrections are negligible.

will be proportional to $1/r^6$ at large distances [52, 53, 27, 50], and thus very small. At small distances both approximations become the unscreened Coulomb potential and the first corrective term is equal to κ .

Hence, we conclude that the use of the approximation (4.24) is justified for our purposes and the correction terms ought to be completely negligible in comparison to other many-particle effects like bound states, which are dominant at low temperatures.

Chapter 5

Numerical computation of the Cluster-functions

5.1 Introduction

In chapter 3 we have seen that the series of thermodynamic functions, such as pressure and density, are given in terms of Quantum virial coefficients. The two-body quantum virial coefficients are known analytically since the pioneering work of Ebeling [24, 54, 55]. The behavior of Quantum cluster functions which involve more than two particles is currently known only at temperatures for which these clusters are dominated by their ground state contribution $Z_{\{N,\gamma\}}(\beta) \sim e^{-\beta E_{0,\{N,\gamma\}}}$.

Our primary objective is to calculate these functions numerically for temperatures where the ground state approximation is not valid, and to connect our numerical results to the analytic low-temperature behavior. To achieve this we need to be able to calculate the cluster functions with high accuracy in a fairly large temperature regime.

The Quantum virial coefficients are expressed by functional integrals which correspond to infinite dimensional ordinary integrals. Numerically these infinite dimensional integrals are approximated by finite dimensional versions (discretized path integrals). The challenge is, therefore, to calculate high dimensional integrals where the integrand is the quantum equivalent of the virial coefficients (see section §3.6 and figure 3.3). The approximation of the continuous path integral by a finite dimensional version has been a major subject of research [38, 56, 57, 58] as it is crucial for convergence and consistency. Having discretized the continuous path integral the remaining problem is its actual evaluation. A technique, that has been used to a great extent, is the Metropolis-algorithm which enables to calculate expectation values over a probability distribution such as, for example, the mean energy [59]. Since we need to calculate virial coefficients, which are “pseudo” partition functions and not expectation values, we cannot apply the Metropolis-Hastings algorithm in a straight forward manner. The thermodynamic integration approach, applied to the integrand in question, runs into complications, as well. The integrand is not a pure exponential but a product of truncated exponentials and as such not positive defined, so that we cannot relate a probability density to it. Thus, we have chosen to calculate these high dimensional integrals by direct sampling, which poses a difficult problem in the temperature regime where partial ionization occurs. For deterministic methods such as the rectangle-rule, the error of the estimator of the integral depends exponentially on the dimensionality of the integrand. The general idea of Monte-Carlo integration is

to evaluate the integrand at points chosen in a certain random fashion and to identify the value of the integral with the mean value of these function evaluations. It can be shown that the standard-deviation of the ensemble of function evaluations, which in this stochastic context is the equivalent of the error for deterministic methods decreases as $\sim \frac{\sigma_0}{\sqrt{N}}$, where N is the number of function evaluations. This way the error of the integral (the standard deviation) does not depend on the dimensionality of the integrand, which makes Monte-Carlo techniques suitable for high-dimensional integrands. The prefactor σ_0 , on the contrary, heavily depends on the specific integrand and on the fashion the points are chosen, where the function is evaluated. To have a precise estimation of the integral we can either evaluate the function at a large number of points N or choose the evaluation points in such a manner that σ_0 is small.

In the following, we will explain in more depth how Monte-Carlo integration is implemented and what its relation to the Metropolis-Hastings algorithm is. After these introductory sections we are going to focus on the specific ideas used in our calculation of the cluster functions (see section §3.6 for their definitions). We will introduce a physically motivated choice of the Importance sampling function and the adaptive path sampling scheme which both turn out to be numerically efficient for our application to few particle Coulomb cluster functions. After the publication of Ref. [12], we became aware of the later work Ref. [60]. In this work, essentially the same Importance sampling approach is proposed in the context of quantum simulations in real time and in one dimension, but not in the imaginary-time domain in which we are working. The second part of this chapter is meant to be an introduction and an overview of the paper [12], where a more detailed discussion of the algorithm and of our numerical results is given. The cluster functions shown in Ref. [12] are truncated according to the SLT-expansion. For historical reasons, we first calculated these cluster functions to improve the SLT-equation of state. The numerical results for the κ -dependent cluster functions, which enjoy the “natural” truncation, are given in section §5.4.

5.2 A few reminders concerning Monte-Carlo integration

The main idea of Monte-Carlo integration is to replace the deterministic method of choosing the integration points by a non-deterministic procedure. For deterministic methods the error of the integration procedure does in general scale as c^D , where D is the number of dimensions of the integration. This is very unfavorable in the case of high-dimensional integrals, and Monte-Carlo integration, which is a stochastic approach, is able to push this boundary. The advantages of the random choice of integration points can be visualized by imagining a two-dimensional function $f(x_1, x_2)$ (for example a Gaussian) which cannot be written as $f(x_1, x_2) = f_1(x_1)f_2(x_2)$. In such a case the deterministic discretization along the axis x_1, x_2 is not natural in view of the correlation between x_1 and x_2 which is present in $f(x_1, x_2)$. Thence, the integration procedure will require a large discretization¹ in order for the algorithm to capture the features of the function. On the other hand, the non-deterministic choice of integration points in the integration region does not have any preferred axis and is thus in some respect more generic². Neverthe-

¹For each additional discretization in one direction, one additional discretization is needed in the other in the case of perfect (anti)-correlation

²The entropy of a state where points are distributed on an “implicit” grid is very low, since it is a very special ordered state. At the same time the number of functions, that this certain choice of integration points integrates exactly, is confined to a certain class of functions (sharing the same symmetries as the grid). In this sense one can expect the randomly distributed points (higher entropy, less symmetries, more probable macrostate) to present a better integration scheme than the “implicit” deterministic grid for a larger class of functions than those accurately integrated by the grid. In simple words: It is more probable to encounter an integrand which is better sampled by randomly distributed points than by a grid, than the other way around. This reasoning is, of course, hand waving but the author thinks that intuition may confirm it.

less, an efficient deterministic procedure is able to “find the contribution” of the integral and puts more effort where the integrand is varying rapidly. We will see that similar adaptive techniques can also be implemented in the context of Monte-Carlo integration.

To introduce the basic concepts we confine ourselves to a one-dimensional example knowing that the generalization to an arbitrary number of dimensions is straight forward. If we would integrate the function $F(x)$ within the boundaries $[a, b]$

$$I = \int_a^b dx F(x), \quad (5.1)$$

a numerical approximation, with a fixed number M of equally spaced discretization points x_i , would be written

$$I_M = \underbrace{\frac{b-a}{M}}_{\Delta x} \sum_{i=1}^M f(x_i). \quad (5.2)$$

If we would choose the points x_i at random, the spacing $\Delta x \neq \frac{b-a}{M}$ would be irregular but in the limit of a large number of points the spacing would be $\langle \Delta x \rangle = \frac{b-a}{M}$ on average. Based on these premises the value of the integral can be identified with an average of the function f over a probability density P which is the uniform density

$$P(x) = \frac{1}{b-a} \Theta(x-a) \Theta(b-x) = \frac{1}{N_P} \Theta(x-a) \Theta(b-x), \quad (5.3)$$

where N_P is the normalization of the function. The Monte-Carlo estimation of the integral becomes simply the mean of the integration points (so-called “sampling points” in the Monte-Carlo context)

$$\langle I \rangle = \frac{1}{M} N_P \sum_{i=1}^M F(x_i) \Big|_{x_i \in P} = \langle N_P F(x) \rangle_{x \in P}. \quad (5.4)$$

Since we have identified the value of the integral with the mean of a function over a probability distribution, we can use all techniques developed in the context of probability theory and calculate, for example, the variance of this expectation value, the equivalent of the error in deterministic numerical integration

$$\sigma_I^2 = \left\langle (N_P F(x))^2 \right\rangle_{x \in P} - \langle I \rangle^2. \quad (5.5)$$

It can be seen from this expression that the variance constant σ_I can be larger than the value of the estimator $\langle I \rangle$ itself. This would lead to a poorly defined value of the integral, and the need of a large number of evaluation points N in order to give it meaning.³ Over the past decades, several techniques have been developed in order to reduce the variance of the estimator of an integral depending on the specific position of the problem. We will mainly focus on the so-called “Importance sampling” since we have decided to use this technique for our numerical calculations.

³Remember that the standard deviation of the mean is decaying like $\sim \frac{\sigma_I}{\sqrt{N}}$

5.2.1 Importance sampling

One possibility to reduce the variance σ_I of the expectation value of the integral is to apply a coordinate transformation that flattens the integrand. This coordinate transformation has the same effect as sampling the integration points from a changed probability density. This can be formally achieved by introducing a so-called Importance sampling function $P(x)$ by virtue of the trivial identity

$$I = \int dx F(x) = \int dx \frac{P(x)}{P(x)} F(x), \quad (5.6)$$

where $P(x)$ is a probability density. In the Monte-Carlo sense this integral can be interpreted as an expectation value of the function $\frac{F(x)}{P(x)}$ where the points of evaluation are chosen from the distribution $P(x)$

$$\langle I \rangle = \left\langle \frac{F(x)}{P(x)} \right\rangle_{x \in P}. \quad (5.7)$$

The variance constant of such an estimator is equal to

$$\sigma_I^2 = \left\langle \left(\frac{F(x)}{P(x)} \right)^2 \right\rangle_{x \in P} - \langle I \rangle^2, \quad (5.8)$$

so that the variance constant becomes zero when the probability density is chosen to mimic the function exactly upon a multiplicative constant (which is the value of the integral itself). A reduction of variance can be achieved by choosing the Importance sampling in such a manner that the function $\frac{F}{P}$ is flatter than the original function F itself.

In summary, we would like to choose the probability density $P(x)$ from which we sample, so that it resembles the integrand $F(x)$. One has to be careful to avoid encountering the case where the function $\frac{F(x)}{P(x)}$ becomes very large for points with a small probability of sampling. Therefore, the Importance sampling function does not necessarily result in a variance decrease and, thus, it has to be chosen carefully to meet the demands.

5.2.2 The Metropolis-Hastings algorithm

The Metropolis-Hastings algorithm enables to calculate expectation values over probability distributions and, thus, integrals of the form

$$\langle O \rangle_F = \frac{\int dx O(x) F(x)}{\int dx F(x)}. \quad (5.9)$$

Using the function $F(x)$ (which does not have to be normalized) as an Importance sampling function we can write

$$\langle O \rangle_F = \int dx O(x) \frac{F(x)}{N_F} \quad (5.10)$$

where $\frac{F(x)}{N_F}$ automatically is a probability density (given that $F(x)$ is positive definite), from which we can sample. The main difference between an ordinary integral and an expectation value is that the latter is evaluated over a probability distribution, whereas for an ordinary integral the integrand does not necessarily contain a normalized probability density. The Metropolis-Hastings algorithm makes use

of this fact and samples directly from any normalized distribution function $\frac{F(x)}{N_F}$. In this sense, the Metropolis-Hastings algorithm is an Importance sampling algorithm where the Importance sampling function is chosen to be $\frac{F(x)}{N_F}$. In a physical context the function $F(x)$, for example, would be the Boltzmann distribution $F(\{x\}) = e^{-\beta H(\{x\})}$. Keeping this in mind we do see immediately that by using the Boltzmann factor $e^{-\beta H(\{x\})}$ as Importance sampling function, the variance reduction is enormous since F is exponential, whereas O is only polynomial in H . The Metropolis-Hastings algorithm, which will be described next, enables sampling from a positive defined function, where the normalization does not need to be known.

The Metropolis-Hastings algorithm constructs a Markov-chain whose distribution of sampled points x_i converges to the distribution $F(x)$ in the limit of a large number of iterations. A Markov-chain is a transition amplitude model where the transition amplitude only depends on the current state and not on previous realizations. The rules for the construction of the Metropolis-Hastings Markov-chain are as follows: The algorithm is initiated by choosing an arbitrary point x_0 and evaluating the function at that point $F(x_0)$ ($i = 0$). An new random point x_{i+1} is generated around the point x_i in a certain way, known as the Metropolis-Hastings step, and the function is evaluated $F(x_{i+1})$. Next, the ratio $r = \frac{F(x_{i+1})}{F(x_i)}$ is calculated and the new point is accepted ($x_{i+1} \rightarrow x_{i+1}$) with a probability $\min(r, 1)$ and rejected otherwise ($x_{i+1} \rightarrow x_i$). The manner how the new points x_{i+1} are generated fulfills the detailed balance condition $F(x)T(x \rightarrow x') = F(x')T(x' \rightarrow x)$. For a large number of iterations of this algorithm, the distribution of the successively chosen points x_i converges to $F(x)$. The most important step in this algorithm is the choice of the Metropolis-Hastings step, the way how proposal points are generated. The simplest approach would be to sample the proposal point from $x_{i+1} = x_i + \epsilon$ where ϵ is an arbitrary translation of maximum amplitude λ . If λ is smaller than the variation of the function to sample from the acceptance ratio is very large, but the phase space is explored only slowly. If, on the other hand, λ is chosen too large, the acceptance ratio drops to a small value and, again, the exploration of phase space is insufficient. The literature argues for a target acceptance ratio of around $1/2$, which can be achieved by tuning λ adaptively. Since the Metropolis-Hastings algorithm can be used to sample from an arbitrary positive definite function we use such a Markov-chain to sample from the Importance sampling function.

5.3 Calculation of cluster functions in vacuum: overview of the article

The cluster functions, which are necessary to derive the equation of state in the activity expansion, and which as well appear in the SLT-expansion, are given in terms of function integrals in path integral language. A numerical approach to calculate these objects must overcome two major difficulties: The divergence of the Coulomb-potential at the origin and the high-dimensionality of the integrand leading in general to poor sampling. A third difficulty, the long-range divergence is naturally taken care of by the use of the screened potential as described in chapter 3.

First, we will present the physical insight that has historically led to the introduction of the physically motivated choice of the Importance sampling function addressing the problem of undersampling, which manifests itself by a large variance of the path integral estimator. Afterwards we will present the idea that has led to the adaptive sampling procedure by briefly reminding the reader of the derivation of the path-integral formulation of matrix elements [43, 61]. Here we focus our attention on the case of a potential that has integrable singularities. These two subjects are major concerns of Ref. [12], together

with the numerical results concluding the chapter. The numerical results presented in this paper are the calculations of the truncated cluster functions appearing naturally at low-temperatures and low densities, the so-called “scaled-low-temperature” limit (see chapter 6). Nevertheless, the approach is independent of the specific form of the integrand and can, therefore, be easily applied to the full κ -dependent cluster functions, too. Again, further information can be found in Ref. [12], where the approach is explained in detail.

5.3.1 The Importance sampling of the paths

To address the first problem, the high-dimensionality of the discretized functional integral and the related poor exploration of phase space, especially when using free particle sampling at low temperatures, we introduced an Importance sampling function. This Importance sampling function is chosen in such a manner that the sampling is focused on the contributing regions of phase space (bound state paths for low temperatures). The insufficiency of free particle sampling can be seen in figure 5.1, where the numerical results for the truncated density matrix⁴

$$\begin{aligned} \rho_{\lambda_{e,p}}^T(\mathbf{r}, \mathbf{r}, \beta) &= \langle \mathbf{r} | e^{-\beta H_{e,p}} - 1 - \dots | \mathbf{r} \rangle \\ &= \int \mathcal{D}(\boldsymbol{\xi}) \left[e^{e^2 \beta \int_0^1 V(\mathbf{r} + \lambda_{e,p} \boldsymbol{\xi}(s))} - 1 - e^2 \beta \int_0^1 V(\mathbf{r} + \lambda_{e,p} \boldsymbol{\xi}(s)) - \dots \right] \end{aligned} \quad (5.11)$$

of the $e-p$ -cluster are shown. The different values of M correspond to different discrete approximations of the continuous path integral (formula (28) of Ref. [12]). The spatial integral of this function gives the value of the truncated cluster function, which we aim to calculate. To generate this plot we used a standard approach called free particle sampling, where the paths are generated by a Levy-construction using the free-particle (Gaussian) part of the integrand [62]. For the potential V_{eff} evaluated along the path, we have chosen the so-called “cumulant” or “effective” potential [38, 57](see equation 33 of Ref. [12]). At high temperatures the so calculated numerical density matrix converges to the analytical result when increasing the (uniform) discretization M of the path integral. For low temperatures, on the other hand, large fluctuations due to undersampling, make its consistent numerical evaluation impossible. The problem can be understood by remembering that the average extension of a Brownian bridge path

⁴For the complete expression see equation (9) of Ref. [12]

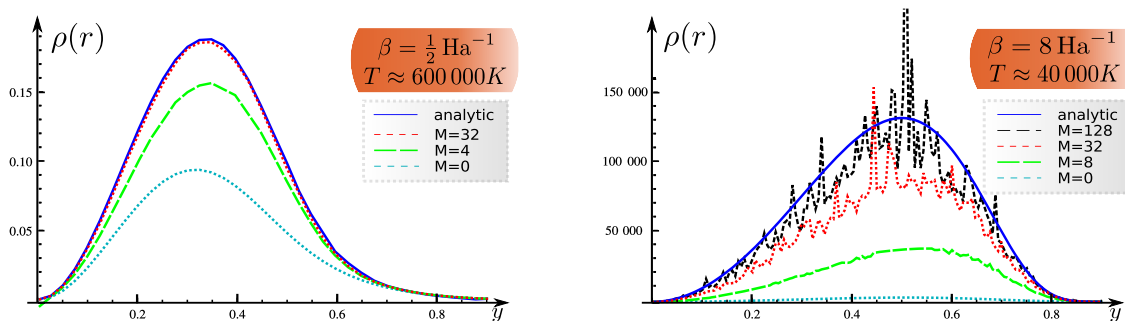


Figure 5.1: The density matrix of the Hydrogen atom is calculated for two temperatures by free particle sampling and using a fixed discretization M and 1 000 000 paths. Free particle sampling gives reliable results for high temperatures (here $T \approx 600\,000\text{K}$). For lower temperature (here $T \approx 40\,000\text{K}$) the increasing variance of the density matrix’s estimator, makes the proper estimation impossible.

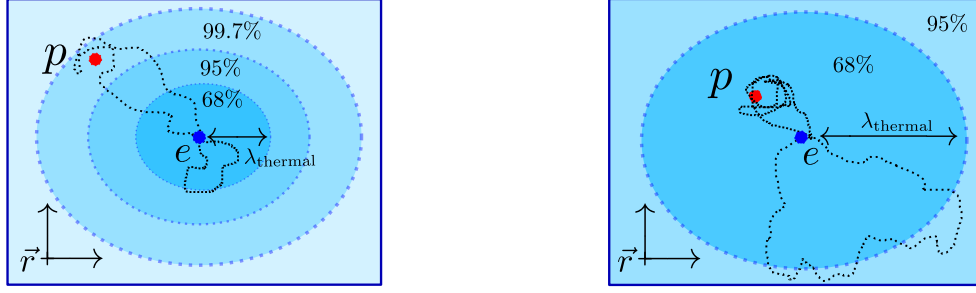


Figure 5.2: Left: At high temperatures free particle sampling works sufficiently well since the large contribution of the potential gets compensated by the small probability to probe the region around the proton. Right: For low temperatures most of the paths will disperse away from the contributing region in space and, thus, the integrand is undersampled.

is proportional to $\lambda \sim \sqrt{\beta}$, the temperature-dependent wavelength, so that the free paths become very extended for low temperatures.

The ground state which is “hidden” in the matrix element and which dominates the latter at low temperatures, has a fixed extension of the Bohr-radius a_B independent of the inverse temperature β . Therefore, when using free-particle paths to sample the integrand, the contributing paths (ground state paths) are rarely sampled and the integrand is undersampled as illustrated in figure 5.2. In the following, we briefly present the general idea of the here proposed solution to this undersampling problem. A more detailed discussion can be found in Ref. [12].

To find an adequate Importance sampling function we analyze the matrix element between two points $\mathbf{x}_1, \mathbf{x}_2$ at a given discretization level $L = \log_2(M)$, to be bisected

$$\left\langle \mathbf{x}_1 \left| e^{\frac{\beta H}{2^{L-1}}} \right| \mathbf{x}_2 \right\rangle \xrightarrow{\text{bisection}} T_{\mathbf{x}_1, \mathbf{x}_2, L}^*(\mathbf{r}) = \left\langle \mathbf{x}_1 \left| e^{-\beta H/2^L} \right| \mathbf{r} \right\rangle \left\langle \mathbf{r} \left| e^{-\beta H/2^L} \right| \mathbf{x}_2 \right\rangle. \quad (5.12)$$

and ask the question how the point \mathbf{r} has to be chosen so that the ground state, dominating the matrix element, is correctly sampled. Inserting closure relations $\sum_n |\psi_n\rangle\langle\psi_n|$ and disregarding all states but the ground state, we find that the bisection points should be distributed according to

$$T_{\mathbf{x}_1, \mathbf{x}_2, L}^*(\mathbf{r}) \propto e^{-\frac{\beta E_0}{2^{L-1}}} |\Psi_0(\mathbf{r})|^2, \quad \beta \rightarrow \infty. \quad (5.13)$$

For high temperatures or equivalently a high discretization level L , the optimal sampling distribution is the free particle distribution

$$T_{\mathbf{x}_1, \mathbf{x}_2, L}^*(\mathbf{r}) \propto e^{-\frac{(\mathbf{x}_m - \mathbf{r})^2}{\lambda^2/(2^L)}}, \quad \beta \rightarrow 0, \quad (5.14)$$

where $\mathbf{x}_m = (\mathbf{x}_1 + \mathbf{x}_2)/2$ is the “center of mass”. With this knowledge we can construct an Importance sampling distribution which captures both limits and whose normalization can be calculated analytically

$$T^* \approx T_{\mathbf{x}_1, \mathbf{x}_2, L}(\mathbf{r}) = \frac{1}{N} e^{-\frac{(\mathbf{x}_m - \mathbf{r})^2}{\lambda^2/(2^L)}} \left(1 + e^{-\frac{\beta E_0}{2^{L-1}}} |\Psi_0(\mathbf{r})|^2 \right). \quad (5.15)$$

For high temperatures, high discretization level L or large mean distances \mathbf{x}_m , the first term is dominant and we mainly sample from the free particle distribution. In the case of low temperature, on the other hand, the free particle distribution does not constrain the \mathbf{r} -dependence and the dominant term is the ground state wave function, so that points are generated mainly according to it. Since the Importance

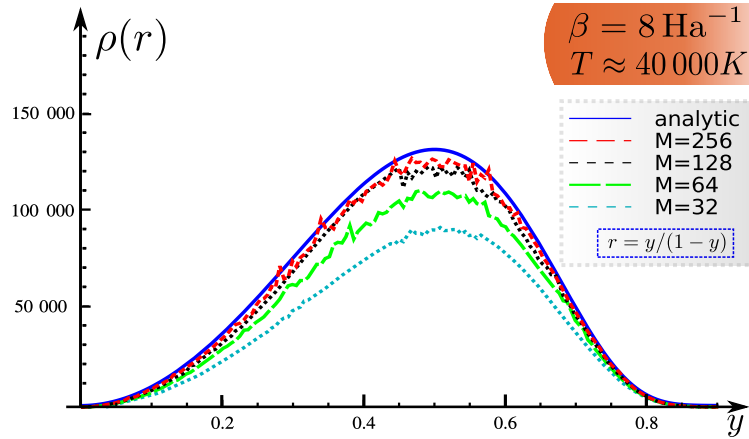


Figure 5.3: The density matrix of Hydrogen calculated using the Importance sampling function $T_{\mathbf{x}_1, \mathbf{x}_2, L}(\mathbf{r}) = \frac{1}{N} e^{-\frac{(\mathbf{x}_m - \mathbf{r})^2}{\lambda^2/(2^L)}} e^{-\frac{\beta E_0}{2^{L-1}}} |\Psi_0(\mathbf{r})|^2$ for different discretization depth M for a temperature of $T \approx 40\,000\text{K}$. As can be seen in comparison with figure 5.1, the variance of the integrand is reduced by the use of the Importance sampling function.

sampling function mimics by construction the bisected matrix element (the exact pair action) it will achieve an important variance reduction by guiding the generated path to the most contributing regions. The effect of this Importance sampling function can be seen in figure 5.3. The Importance sampling of the paths leads to a dramatic decrease of the fluctuations of the numerical density matrix, which is achieved by directing the paths to the contributing region in phase space⁵. In the former plots the discretization level is a parameter of the calculation and its choice has a substantial impact on the actual estimate of the integral. The answer to the question how discretization level has to be chosen to assure a correctly converged result is one aspect of the adaptive discretization scheme, which will be described in the following subsection.

5.3.2 Adaptive discretization of path integrals

There are several reasons why an adaptive discretization procedure is advantageous and even necessary. Firstly, the discretization has to be chosen sufficiently fine for the discrete path integral to be converged to its continuous version (see figure 5.3). Furthermore, the Coulomb singularity which is present in the discretized path integral signals that special care is required, when passing from the continuous to the discrete path integral. Eventually, an adaptive discretization directs the numerical effort to where it is really needed, to regions in phase space for which correlations of the paths have to be considered, and, therefore, it is numerically desirable. In the following, we will retrace the derivation of the relation between the matrix element and the path integral, which is given by the Feynmann-Kac formula. Since the firm mathematical formulation of the path integral is still a subject of active research, we restrict ourselves to a physicist way of reasoning and do not claim mathematical rigorosness.

We want to calculate matrix elements for a certain Hamiltonian $H = -D^2 + V$, where $-D^2$ is the

⁵For historical reasons the Importance sampling function used to generate the plot 5.3 differs from the currently used one (5.15). The difference lies in the absence of the free part (the $1 + \dots$ in formula equation (5.15)). When taking this free term into account, fluctuations diminish further, since only then the Importance sampling function reduces to the free particle sampling for high discretization levels. We include this “antique” plot nevertheless, as it shows the genuine impact of the physically motivated choice of paths.

kinetic part and V the potential. We make use of the Trotter-formula which is valid in the limit $M \rightarrow \infty$

$$\langle \mathbf{x}_1 | e^{-\beta H} | \mathbf{x}_2 \rangle = \langle \mathbf{x}_1 | e^{\beta(D^2 - V)} | \mathbf{x}_2 \rangle = \lim_{M \rightarrow \infty} \langle \mathbf{x}_1 | \left(e^{\frac{\beta}{M} D^2} e^{-\frac{\beta}{M} V} \right)^M | \mathbf{x}_2 \rangle. \quad (5.16)$$

In order to arrive at the Feynman-Kac formula, closure relations in between the M -terms of the product in equation (5.16) are inserted, and afterwards the limit $M \rightarrow \infty$ is considered

$$\langle \mathbf{x}_1 | e^{-\beta H} | \mathbf{x}_2 \rangle = \int \mathcal{D}(\boldsymbol{\xi}) e^{-\beta \int_0^1 ds V((1-s)\mathbf{x}_1 + s\mathbf{x}_2 + \lambda \boldsymbol{\xi}(s))}. \quad (5.17)$$

The measure $\int \mathcal{D}(\boldsymbol{\xi})$ is called the Wiener measure and is defined by its covariance

$$\int \mathcal{D}(\boldsymbol{\xi}) \boldsymbol{\xi}(s_1) \boldsymbol{\xi}(s_2) = \mathbb{1} \min(s_1, s_2) (1 - \max(s_1, s_2)). \quad (5.18)$$

To make use of the path integral numerically, which is based on the equivalence (5.17), the path integral is usually evaluated at finite discretization depth M

$$\langle \mathbf{x}_1 | e^{-\beta H} | \mathbf{x}_2 \rangle \approx \int \mathcal{D}_{\text{disc}}(\boldsymbol{\xi}) e^{-\frac{\beta}{M} \sum_{i=1}^M V((1-s_i)\mathbf{x}_1 + s_i\mathbf{x}_2 + \lambda \boldsymbol{\xi}(s_i))}. \quad (5.19)$$

Hence, the ‘‘time’’ interval $s \in [0, 1)$ is discretized in M slices. This is the crucial transition from an infinite dimensional integral (5.17) to a numerically evaluable finite dimensional one (5.19). The discretized Wiener measure has the same covariance as its continuous version with the times restricted to its discrete values. The explicit formula for the discretized measure is

$$\int \mathcal{D}_{\text{disc}}(\boldsymbol{\xi}) = \prod_{i=1}^M \int d\boldsymbol{\xi}_i \exp \left(-\frac{M}{2} \sum_{i=0}^M (\boldsymbol{\xi}_i - \boldsymbol{\xi}_{i+1})^2 \right) \quad \text{with } \boldsymbol{\xi}_0 = \boldsymbol{\xi}_{M+1} = 0. \quad (5.20)$$

In the case of a regular potential this discretized version is not problematic, whereas in the case of a potential V that has a singularity, this discretized path integral is infinite for every finite value of M , even though its continuous equivalent has a finite value. In the discretized version the Coulomb potential is exponentiated $e^{\frac{\beta}{M|\mathbf{x}(s_i)|}}$, giving rise to a non-integrable singularity at the origin of the potential. Usually this non-integrability problem is solved by either the use of the exact pair-action, which is finite at the origin, or by the use of the cumulant potential, a bound, partially averaged version of the original Coulomb potential [38, 58]. Our insights on the rediscritization procedure will give rise to a new approach, that treats the Coulomb singularity like it is suggested by the continuous path integral. This way the infinities related to the Coulomb singularity present in equation (5.19) are avoided from the start. To understand this subtlety we have to go back to the Trotter formula (5.16) and keep in mind that it only holds in the limit $m \rightarrow \infty$. Since only linear terms will survive the limit $M \rightarrow \infty$, we may also write

$$\langle \mathbf{x}_1 | e^{-\beta H} | \mathbf{x}_2 \rangle = \langle \mathbf{x}_1 | e^{\beta(D^2 - V)} | \mathbf{x}_2 \rangle = \left\langle \mathbf{x}_1 \left| \lim_{M \rightarrow \infty} \left(e^{\frac{\beta}{M} D^2} \left(1 - \frac{\beta}{M} V \right) \right)^M \right| \mathbf{x}_2 \right\rangle. \quad (5.21)$$

Inserting closure relations we derive the corresponding discretized path integral formula

$$\langle \mathbf{x}_1 | e^{-\beta H} | \mathbf{x}_2 \rangle = \int \mathcal{D}_{\text{disc}}(\boldsymbol{\xi}) \prod_{i=1}^M \left[1 - \frac{\beta}{M} V_{\text{cum}}(\mathbf{x}(s_i) + \lambda \boldsymbol{\xi}(s_i), \mathbf{x}(s_i) + \lambda \boldsymbol{\xi}(s_i + 1), \lambda_M) \right]. \quad (5.22)$$

with $\mathbf{x}(s) = (1-s)\mathbf{x}_1 + s\mathbf{x}_2$, $\lambda_M = \lambda/\sqrt{M}$ and the so-called cumulant potential

$$V_{\text{cum}}(\mathbf{x}_1, \mathbf{x}_2, \lambda) = \int \mathcal{D}(\boldsymbol{\xi}) \int ds V((1-s)\mathbf{x}_1 + s\mathbf{x}_2 + \lambda\boldsymbol{\xi}). \quad (5.23)$$

The above formula converges to the continuous path integral in the limit $M \rightarrow \infty$. In fact, the above given discretized path integral (5.22) is the natural choice of discretization if the original continuous path integral is interpreted as a product integral [63]. The main advantage of the formula (5.22) is that it takes finite value for a fixed discretization depth M , even if we would replace the cumulant potential by the bare Coulomb potential. Furthermore, we learn from the product integral interpretation of the discretized path integral (5.22) how the collapse of the path can be avoided in the case of the Coulomb potential, even when using equation (5.19): We should make sure that a path is discretized in such a manner that the artificial terms $V(\mathbf{x}(s_i) + \lambda\boldsymbol{\xi}(s_i), \mathbf{x}(s_i) + \lambda\boldsymbol{\xi}(s_{i+1}))^n$ with $n > 1$ for a given time s are not present. This is the essence of the adaptive discretization proposed in Ref. [12], which bisects a path until the action for each sub-path element is small

$$\left| \frac{\beta}{M} V(\mathbf{x}(s_i), \mathbf{x}(s_{i+1})) \right| < \epsilon < 1 \quad (5.24)$$

compared to a tuning parameter ϵ . In this way terms beyond the linear one in the expansion of $e^{\beta V}$ are suppressed for each submatrix element. If the breakup condition is fulfilled for each time slice separately, equation (5.19) enjoys the same convergence properties as equation (5.22) and thereby, establishes the approximate equivalence between the two discretized path integral formula equations (5.19) and (5.22). The algorithm is strongly influenced by the discussion of Kleinert [61] of how the collapse of the path is prevented by the entropy associated with highly discretized paths. In the two-particle case this discretization scheme is, of course, superseded by the use of the analytically known exact action S_{γ_1, γ_2} which can be deduced from the solution of the two-particle Coulomb problem [64, 38, 65]

$$\begin{aligned} e^{-\beta S_{\gamma_1, \gamma_2}(\mathbf{x}_1, \mathbf{x}_2)} &= \langle \mathbf{x}_1 | e^{-\beta H_{\gamma_1, \gamma_2}} | \mathbf{x}_2 \rangle \\ &= \int \mathcal{D}(\boldsymbol{\xi}) e^{\beta \int_0^1 ds V((1-s)\mathbf{x}_1 + s\boldsymbol{\xi}_2 + \lambda_{\gamma_1, \gamma_2} \boldsymbol{\xi}(s))}. \end{aligned} \quad (5.25)$$

In the references [38, 66, 67, 68] efficient numerical algorithms for the computation of these exact two-body Coulomb density matrices are given. In the many-body case, on the other hand, paths have to be finely discretized to capture the correlations between the particles, even when relying on the pair exact action and the advantages of its use are lost.

This is illustrated in figure 5.4, which shows that paths contained in the exact actions of the electron-proton (in red) and electron-electron (in blue) exact pair actions show opposite behavior. The electron paths contained in the electron-proton pair-action are mainly concentrated around the proton, so that the electrons come close to each other. The electron-electron pair action, on the contrary, mostly contains paths where the electrons disperse away from each other. Thus, the correlations between the paths present in the exact three-body action are not properly accounted for when using the pair-product approximation (unless the effective temperature of the “time”-slice is high)⁶. Mathematically this reasoning can be based on the non-commutativity of the different pair action Hamiltonians, present in the few-body case. In the case of three particles, for each submatrix element, its pair-product action approximation using the

⁶In operator language the Hamiltonians related to the different exact pair-actions do not commute.

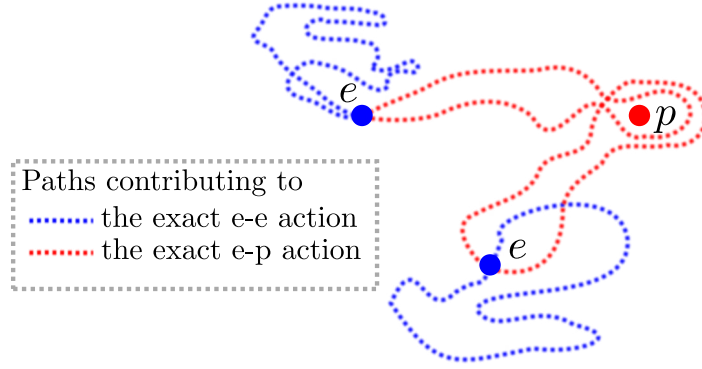


Figure 5.4: The path contained in the exact actions of e-e and e-p pairs are incompatible and demand for a high discretization (or equivalently high effective temperature of the “time”-slice) in order to capture their correlations adequately.

exact pair action, leads to sub-matrix elements that are not equivalent to the matrix element of the three particle Hamiltonian

$$e^{-\frac{\beta}{2L}(S_{\gamma_1,\gamma_2}(\vec{x}_1,\vec{x}_2)+S_{\gamma_1,\gamma_3}(\vec{x}_1,\vec{x}_2)+S_{\gamma_2,\gamma_3}(\vec{x}_1,\vec{x}_2))} = \langle \vec{x}_1 | e^{-\frac{\beta}{2L}H_{\gamma_1,\gamma_2}} | \vec{x}_2 \rangle \cdot \langle \vec{x}_1 | e^{-\frac{\beta}{2L}H_{\gamma_1,\gamma_3}} | \vec{x}_2 \rangle \cdot \langle \vec{x}_1 | e^{-\frac{\beta}{2L}H_{\gamma_2,\gamma_3}} | \vec{x}_2 \rangle \quad (5.26)$$

$$\neq \langle \vec{x}_1 | e^{-\frac{\beta}{2L}H_{\gamma_1,\gamma_2}} e^{-\frac{\beta}{2L}H_{\gamma_1,\gamma_3}} e^{-\frac{\beta}{2L}H_{\gamma_2,\gamma_3}} | \vec{x}_2 \rangle \quad (5.27)$$

$$\neq \langle \vec{x}_1 | e^{-\frac{\beta}{2L}H_{\gamma_1,\gamma_2,\gamma_3}} | \vec{x}_2 \rangle \quad (5.28)$$

Here $\vec{x} = \{\mathbf{r}_1, \mathbf{r}_2, \mathbf{R}_3\}$ is the combined vector of particle positions. The Hamiltonians describing different pair actions do not commute, and additional terms would occur when trying to combine the different exponentiated Hamiltonians. These additional terms would be related to those of the Baker-Hausdorff formula, but they would not be equivalent since even equation (5.26) and equation (5.27) are not equal. The fact that the Hamiltonians do not commute and cannot be separated is directly related to the fact that the paths contained in each exact two-body action are uncorrelated with respect to each other and can in general not be reconciled. When using the pair-action approximation with the exact pair action the error is, therefore, proportional to the commutator of the Hamiltonians $\left[\frac{\beta}{2L}H_{\gamma_1,\gamma_2}, \frac{\beta}{2L}H_{\gamma_1,\gamma_3} \right]^7$. This commutator becomes small in the limit of a large discretization of the particle paths ($L \rightarrow \infty$), where the exact action becomes the cumulant action (5.23). Due to the harmonicity of the Coulomb potential the cumulant action turns out to have same convergence properties as the straight line action defined by taking the limit $\lambda \rightarrow 0$ of the cumulant potential (5.23)

$$V_{\text{line}}(\mathbf{x}_1, \mathbf{x}_2) = \int ds V((1-s)\mathbf{x}_1 + s\mathbf{x}_2), \quad (5.29)$$

as shown in TABLE I of Ref. [12]. In the calculations of the few-body cluster functions we are using this semi-classical line action to evaluate the action of a given path as well as to check for each line segment if the breakup condition (5.24) is fulfilled. The main advantage of the adaptive discretization scheme is that the computational effort is concentrated on configurations where a high discretization is necessary to

⁷The kinetic terms $[D_{\gamma_1,\gamma_2}^2, D_{\gamma_1,\gamma_3}^2]$ as well as the potentials $[V_{\gamma_1,\gamma_2}, V_{\gamma_1,\gamma_3}]$, commute and only the cross term survives.

capture the correlations between the paths correctly. Furthermore, the Coulomb divergence which is not present in the continuous path integral version, is effectively eradicated even when using an unbounded approximation of the effective potential, such as the straight line action.

5.3.3 Results

The adaptive discretization together with the Importance sampling has been used to calculate the two and three-body cluster functions of which we have made accurate tabulations [12]. One advantage of the adaptive discretization scheme is that the numerical effort is directed towards portions of the paths which have to be discretized finely to capture correlations (regions where the potential is strong). This can be seen by tracing the average discretization as a function of the distance. In FIG.4 of the article we show that, as expected, the numerical effort is concentrated on configurations where the electron and the proton are close. By using the lowest discretization of paths possible, that still captures their correlations, the dimensionality of the integral is effectively minimized and, together with it, the variance of the estimator. In this way the adaptive discretization outperforms the uniform discretization especially for low temperatures, which can be seen in TABLE I of Ref. [12].

The main goal of this paper was to calculate the truncated cluster functions which appear as coefficients in the series for thermodynamic quantities at low temperatures. For low temperatures these functions are dominated by the ground state contribution of the particular particle cluster $Z_{\{N_\gamma\}} \sim e^{-\beta E_{0,\{N_\gamma\}}}$ ⁸. The ground state energy can be determined by fitting an exponential to the cluster function for low temperatures⁹. In the case of the H_2^+ molecule our results are compatible with the Stancil partition function [69], where a Density functional analysis was used to determine the first bound states of the system. We have been able to do this for the four considered cluster functions with good accuracy (error on the ground state energy $\delta E_0 < 1\%$). Even though the calculation of the cluster functions at temperatures so low that only the ground state remains was not the primary aim, it is comforting and shows the numerical accuracy and reliability of our numerical algorithm.

We can conclude that the aim to extend the known low-temperature asymptotes to higher temperatures has been achieved. The uncertainties on the three particle cluster functions 2e-p and e-2p at low temperatures will be, by hindsight, of no importance since these clusters do only contribute in the high/intermediate temperature regime where the path integration gives precise results. One important insight gained from the calculation of the truncated cluster functions of three particles is that, in the low and intermediate temperature regime, the ground state approximation is not valid at all. For the Hydrogen atom cluster, the ground state approximation breaks down for inverse temperatures smaller than $\beta = 10 \text{ Ha}^{-1}$. From the plots in FIG.6 of Ref. [12] or from figure 5.7 we see that even for inverse temperatures as large as $\beta = 40 \text{ Ha}^{-1}$ the ground state approximation for the 2e-1p cluster is not valid.

⁸In the case of H_2^+ the cluster function has a more complex structure due to the small energy separation of vibrational and rotational modes [69]

⁹There is only one free parameter E_0 , the prefactor is fixed

5.4 κ -dependent Cluster functions

The cluster functions appearing in the SLT-approach do not depend on the screening parameter κ and, thus, their use is restrained to the low-density and low-temperature regime by definition. In order to lift this limitation we calculate the genuine κ -dependent cluster functions defined in section §3.6. In contrast to the SLT-cluster functions the κ -dependent cluster functions enjoy the “natural” truncation; the truncation arising naturally from the resummation procedure and the associated double counting rules. We have already seen in the paper [12] that for the non-neutral H_2^+ and H^- cluster functions the truncation has an important impact even on the low-temperature behavior. In the following, we will present to the reader a few selected examples of κ -dependent cluster functions, which can be divided in three separate classes: neutral, charged and exchange clusters. The cluster functions have been calculated for 50 values of κ exponentially spaced in the range $\kappa a_0 \in [1, 10^{-7}]$ and values linearly spaced in $\sqrt{\beta E_0} = \lambda/a_0 \in [0.25, 7.25]$. The shown functions have been interpolated on this $\kappa, \sqrt{\beta}$ grid and, therefore, we do not provide error bars. From the results presented in Ref. [12] we have seen that the error bars are negligibly small in the high and intermediate temperature regime.

The explicit formulas for these two and three loop cluster functions in diagrammatic language are given by (see section §3.6)

$$C_{\gamma_1, \gamma_2} = \begin{array}{c} \text{---} \circ \text{---} \circ \text{---} \\ \text{---} \text{---} \text{---} \\ \gamma_1 \quad \gamma_2 \end{array} \cdot \underbrace{\exp\left(\frac{(\sum_i e_{\gamma_i}^2)\beta\kappa}{2}\right)}_{\text{dressing factor}} \quad (5.30)$$

and

$$C_{\gamma_1, \gamma_2, \gamma_3} = \frac{1}{6} \left(\begin{array}{cccc} \begin{array}{c} \gamma_3 \\ \circ \\ \text{---} \circ \text{---} \circ \text{---} \\ \text{---} \text{---} \text{---} \\ \gamma_1 \quad \gamma_2 \end{array} & + & \begin{array}{c} \gamma_3 \\ \circ \\ \text{---} \circ \text{---} \circ \text{---} \\ \text{---} \text{---} \text{---} \\ \gamma_1 \quad \gamma_2 \end{array} & + & \begin{array}{c} \gamma_3 \\ \circ \\ \text{---} \circ \text{---} \circ \text{---} \\ \text{---} \text{---} \text{---} \\ \gamma_1 \quad \gamma_2 \end{array} & + & \begin{array}{c} \gamma_3 \\ \circ \\ \text{---} \circ \text{---} \circ \text{---} \\ \text{---} \text{---} \text{---} \\ \gamma_1 \quad \gamma_2 \end{array} \\ \\ \begin{array}{c} \gamma_3 \\ \circ \\ \text{---} \circ \text{---} \circ \text{---} \\ \text{---} \text{---} \text{---} \\ \gamma_1 \quad \gamma_2 \end{array} & + & \begin{array}{c} \gamma_3 \\ \circ \\ \text{---} \circ \text{---} \circ \text{---} \\ \text{---} \text{---} \text{---} \\ \gamma_1 \quad \gamma_2 \end{array} & + & \begin{array}{c} \gamma_3 \\ \circ \\ \text{---} \circ \text{---} \circ \text{---} \\ \text{---} \text{---} \text{---} \\ \gamma_1 \quad \gamma_2 \end{array} \\ \\ \begin{array}{c} \gamma_3 \\ \circ \\ \text{---} \circ \text{---} \circ \text{---} \\ \text{---} \text{---} \text{---} \\ \gamma_1 \quad \gamma_2 \end{array} & - & \begin{array}{c} \gamma_3 \\ \circ \\ \text{---} \circ \text{---} \circ \text{---} \\ \text{---} \text{---} \text{---} \\ \gamma_1 \quad \gamma_2 \end{array} & - & \begin{array}{c} \gamma_3 \\ \circ \\ \text{---} \circ \text{---} \circ \text{---} \\ \text{---} \text{---} \text{---} \\ \gamma_1 \quad \gamma_2 \end{array} & - & \begin{array}{c} \gamma_3 \\ \circ \\ \text{---} \circ \text{---} \circ \text{---} \\ \text{---} \text{---} \text{---} \\ \gamma_1 \quad \gamma_2 \end{array} \end{array} \right) \cdot \exp\left(\frac{(\sum_i e_{\gamma_i}^2)\beta\kappa}{2}\right) \quad (5.31)$$

In both cases we multiply by the respective dressing factors which cancel out the first order correction in κ (see discussion in section §4.1) These diagrams are used for all two and three loop clusters respectively. The diagrammatic expressions for the different particle clusters differ only by dressing factors related to the attached rings.

5.4.1 Neutral cluster functions: H and He

In figure 5.5 we plot the Hydrogen cluster function¹⁰ together with the direct term of the Helium cluster function¹¹ for different values of the screening constant κ . In both cases the numerical cluster function is divided by the respective ground state partition function. The ground state energy of the Helium cluster is taken to be the experimental value $E_0 = 2.9034$ Ha.

The fact that the Hydrogen cluster function grows faster than the ground state partition function when $\kappa a_0 < 10^{-1}$, can be understood as follows: The attached loops provide a multiplicative factor $e^{\beta\kappa}$ which usually cancels the first order correction of the ground state energy. For large values of κ this multiplicative factor then simply grows faster than the ground state energy diminishes. This effect is an indicator that, for these parameters the classical approximation of the attached loops breaks down since $\kappa\lambda > 1$ and, secondly that the classical approximation of the used loop-loop potential is not valid, neither. In order to make precise predictions for such conditions, all quantum effects present in the full loop-loop potential should be taken into account, so that our calculations are insufficient here.

Since our numerical calculation, even though accurate, are afflicted with numerical errors, especially at very low temperatures, we use the analytically known low-temperature asymptote from a certain point on (as marked in the plots). To understand the numerical precision achieved by using the Importance

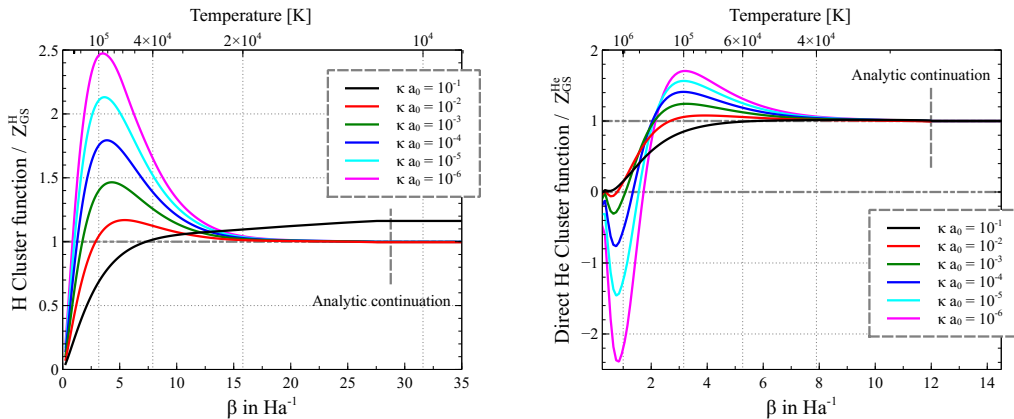


Figure 5.5: The numerical results for the Hydrogen and the Helium cluster functions. For low temperatures our numerical calculations are recovering the ground state partition functions. In the high-temperature regime the κ -dependent parts of the cluster function are dominant and give important contributions. We choose a certain temperature from which on we use the ground state partition function in our further calculations. For screening constant larger than $\kappa a_0 > 10^{-1}$, the result can not be trusted for the reason explained in the main text.

sampling together with the adaptive discretization, we plot the Helium Cluster function but not divided by the partition function computed with the experimental value of the energy but with $E'_0 = 2.9000$ Ha instead (see figure 5.6). The offset at the continuation point is clearly visible, showing that our approach leads to very reasonable results. It could be objected that in the case of the Hydrogen cluster the numerical precision is built in as we are using part of the analytical solution, namely the ground state wave function, for the Importance sampling of the paths. In the case of the Helium cluster function this concern is certainly not tenable, since the electron-electron repulsion plays a major role.

¹⁰Remember that each particle in the cluster is dressed.

¹¹Due to the quantum statistics of the fundamental particles an exchange cluster function appears in the diagrammatic series, too. The respective exchange cluster function is discussed later and shown in figure 5.11

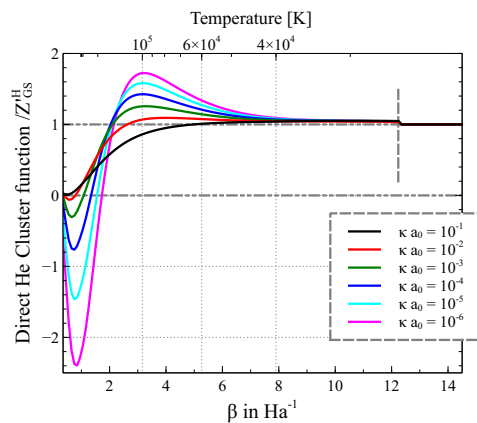


Figure 5.6: The way the cluster functions are plotted makes it possible to see even small deviations of the ground state energy. For this plot we used $E_{\text{He}} = 2.9 \text{ Ha}$.

5.4.2 Charged cluster functions

The three-body cluster functions shown in Ref. [12] were calculated using the SLT truncation. We found that the truncation plays a major role even for low temperatures. It was not adequate to separate the full truncated cluster function, in an atom cluster function (explicitly called $Z_{2e,p}, Z_{e,2p}$ in [12]) and atom-charge interactions W as it has been suggested in [13]. These two contributions cancel each other to a great extent, which suggests that in order to obtain an accurate result for the third order virial the natural truncation should be used, since only this truncation is completely unambiguous¹² In figure 5.7 the cluster functions of the H^- and H_2^+ Clusters¹⁰ (normalized by the Hydrogen ground state) are shown for several values of κ . The κ -dependent cluster functions are negative for a large range of temperatures. In the case of the H_2^+ the cluster function is even negative in the whole temperature regime shown here. When comparing these two cluster functions as shown for $\kappa = 10^{-5} a_0^{-1}$ in figure 5.8, we recognize their similarity, which is caused by the fact that both are dominated by atom-charge interactions for these temperatures. Figure 5.8 shows the low-temperature behavior of the H^- cluster function, where this time we divided by the Boltzmann factor using the experimental value of the ground state energy $E_0^{\text{H}^-} = 0.527 \text{ Ha}$. This leads to the conclusion that even for temperatures as low as $\beta = 40 \text{ Ha}^{-1}$ the

¹²The SLT-truncation is also unambiguous but it is only of significance in the SLT-limit, thus at low temperatures.

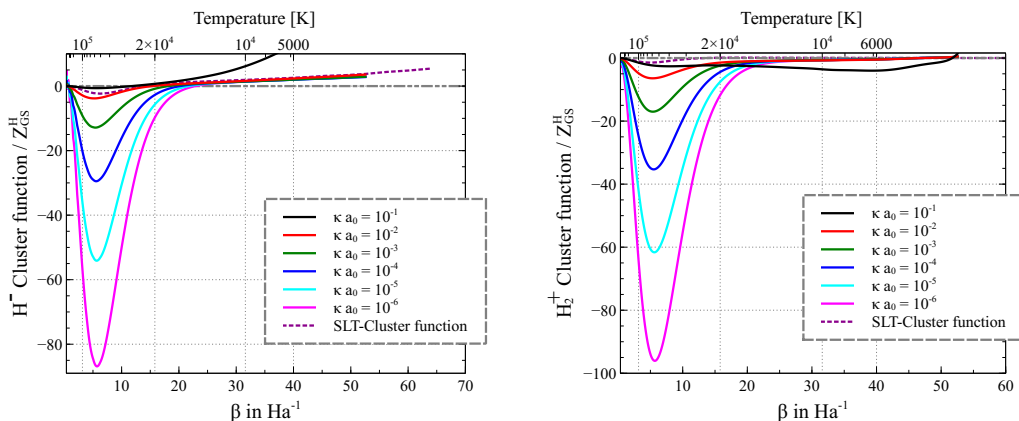


Figure 5.7: The H^- and H_2^+ cluster functions for different values of κ .

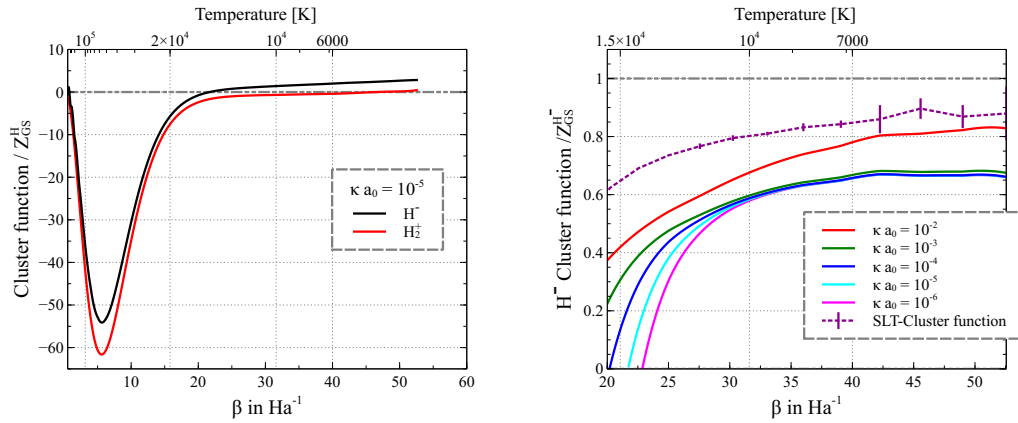


Figure 5.8: Left: The H^- and H_2^+ cluster functions shown in comparison for a small value of κ . Both functions are negative in almost the whole regime here shown and are not dominated by their ground state contribution. This indicates that charge-charge and atom-charge interaction are dominant. Right: Zooming into the low-temperature regime we see clear deviations of the cluster function and the ground state asymptotic value of 1. When comparing to the SLT-cluster function we have to remember that the truncation is different.

ground state approximation of the cluster function is not valid. At the same time, the cluster function shows no evidence for a κ -dependence anymore, which reflects the fact that their value is determined by short-distance interactions. The H^- cluster function using the SLT-truncation, is shown for comparison and develops the same very slow crossover to the ground state approximation for low temperatures. We have to admit that we are, at the moment, not able to make precise predictions for temperatures lower than $\beta = 40 \text{Ha}^{-1}$ ¹³. We do not deem this problematic, since the SLT analysis has shown [13] that the contribution to the equation of state of the three-particle cluster functions is limited to intermediate temperatures.

Our results show that the H_2^+ and H^- cluster function are dominated by diffusive states for intermediate temperatures.

We show the $3e$ and $3p$ functions in figure 5.9. These cluster functions are again normalized by the Hydrogen ground state partition function to facilitate comparison. They show the same “bump” in the high-temperature regime, which will compensate for the negative parts of the H^- and H_2^+ cluster functions. Figure 5.10 shows the combination of these cluster functions as it appears in the equation of state of a pure Hydrogen system

$$B_3 = \frac{1}{6} \left(\begin{array}{c} \text{3e} \\ \text{3p} \\ \text{2e, 1p} \\ \text{1e, 2p} \end{array} \right) \quad (5.32)$$

for different values of κ . At first glance we recognize that a large compensation between the contributions of the different cluster functions has taken place. An important basic information we gather from this plot is that the direct part of the three particle cluster functions is expected to result in a decrease of the pressure, since the combination appearing in the pressure series is positive.

¹³The large discretization level necessary to capture the path correlations makes the numerical calculations very slow and at the same time systematic discretization errors accumulate even when using the exact pair action making the path integral approach unfeasible.

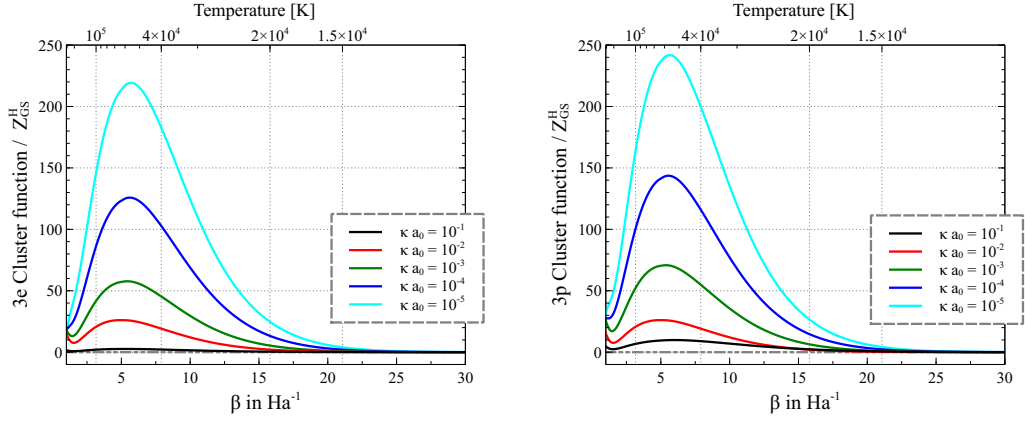


Figure 5.9: The three electron and three proton diagrams are positive and do not contain any relevant exponentially growing terms at low temperatures. Nevertheless their contribution is substantial for high temperatures and cancels to a large amount the negative contributions of the H^- and H_2^+ cluster functions.

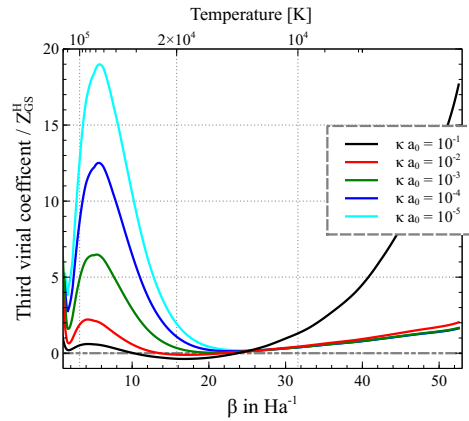


Figure 5.10: We show the combination of three particle cluster functions as they appear in the fugacity series of a neutral e,p-plasma. By the fact that this third virial coefficient is positive, we expect that this contribution leads to a decrease in the pressure.

5.4.3 Exchange functions

In path integral language the Fermi-statistic of the fundamental constituents leads to diagrams, where several particles of the same species are forming one loop. We call diagrams where nodes are not made of single particles but of loops with more than one particle, exchange diagrams. Particles in a loop interact repulsively as given by the loop fugacity factor ((3.14) and (3.15)). Due to this repulsion and the fact that particles in a loop are, on average, separated by a distance λ_γ , it follows that proton and α exchange diagrams are entirely negligible, so that we only have to consider electron exchange diagrams. The Helium atom, for example, contains two electrons and, thus, in addition to the so-called direct cluster function (see figure 5.5) an exchange diagram is present in the quantum Mayer series for the pressure. This diagram will ensure the correct counting factors for the Helium ground state, in \mathbf{r} -space symmetric and anti-symmetric in spin-space.

The diagram which represents the Helium exchange cluster function is given by

$$\alpha, e^2 = \text{diagram 1} + \text{diagram 2} + \text{diagram 3} + \dots, \quad (5.33)$$

where we indicate by e^2 that the two electrons form one loop, so that (5.33) is a two-loop diagram. Furthermore, the loops are dressed multiplied with the factor provided by attached “rings”. The interaction between these loops is given by formula (3.69). The numeric evaluation of these exchange diagrams is straightforward since we only have to specify the correct start end end points for the paths of the two exchanging electrons. After this initialization we can use the same Importance sampling function together with the adaptive discretization scheme as for the direct cluster functions.

Our results for the Helium exchange function are presented in figure 5.11. At low temperatures, the exchange cluster function is determined by the Helium ground state, which ensures the correct multiplicity of the ground wave function in the Mayer series for the pressure. For lower temperatures we use the ground state approximation. Figure 5.11 shows our results for the Helium exchange functions alongside with the H^- exchange function. We see a “bump” in the high-temperature regime and, as for the direct H^- cluster function, the slow crossover to the ground state partition function. In figure 5.11 we have normalized the cluster function by the ground state partition function using the experimental value of the ground state energy $E = 0.5277$ Ha.

To make the reader aware of the accuracy one needs in order to be able to make precise predictions in the crossover regime, we plotted the H^- cluster function divided by the ground state partition function using the value $E_0^{\text{H}^-} = 0.52$ Ha for the energy (see figure 5.13). The very small energy difference $\Delta E = 0.0277$ Ha between the Hydrogen and the H^- ground state makes it very difficult to achieve accurate numerical results. In fact, the two additional interactions present in the H^- cluster, with respect to the Hydrogen cluster function, cause only a small difference in energy ΔE . For most of the sampled paths these two additional interactions cancel to a large extend, so that numerical errors are amplified. This is also the reason why it is easier to make accurate predictions for the Helium atom: The electron-electron interaction is twice smaller than the electron- α interaction, so that this cancellation is incomplete and numerical errors of the path integral relative to the ground state energy are smaller. Even though we are not able to achieve the desired high accuracy in the case of the H_2^+ and H^- ions, these clusters will not contribute to any sizable amount to the equation of state for the considered low-density conditions since they are suppressed by one additional fugacity factor with respect to the Hydrogen cluster function.

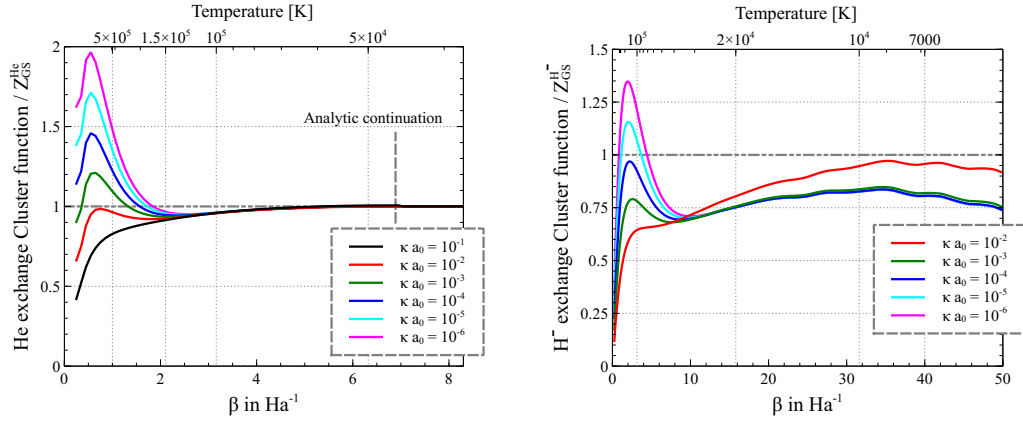


Figure 5.11: Our numerical results for the Helium and the H^- exchange functions for several screening constants κ . These cluster functions ensure the correct multiplicity of the ground state and are of purely Quantum mechanical origin.

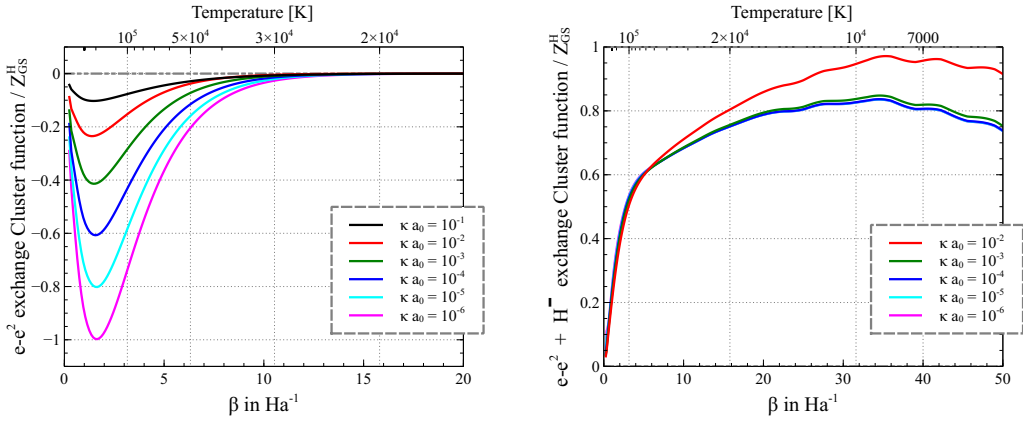


Figure 5.12: Left: The three electron exchange function. Right: For high temperatures the three electron exchange function and the H^- exchange function are of the same order and compensate each other to a large amount.

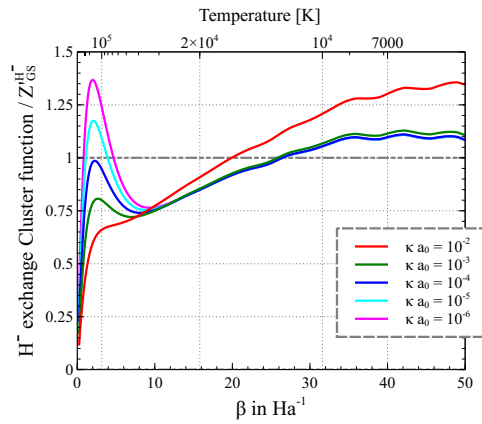


Figure 5.13: The H^- exchange function, where we used a reference ground state partition function with the energy $E = 0.52 \text{ Ha}$.

Chapter 6

Thermodynamics of pure Hydrogen at low densities and low temperatures

6.1 Scaled-low-temperature limit

In this chapter we will use the numerically calculated truncated cluster functions to ameliorate the so-called SLT-equation of state of a pure Hydrogen system by taking into account three body interactions between the basic constituents (e, p).

The equations for the pressure in terms of the density are based on the work in Ref. [13], which contains a profound analysis of corrective terms to the widely known Saha-equation of state. Historically, the Saha-equation has been derived from a chemical picture. As it has been stated before, in the physical picture a model equation of state is completely described by the pressure in terms of the fugacities and the temperature $P(\beta, \{z_\gamma\})$. We are able to find a pressure model in the physical picture that results in the Saha-equation, which enables us to quantify its basic assumptions. In earlier works by the authors of [34, 13], corrective terms to the Saha-equation of state in the scaled low-temperature limit (SLT) have been investigated.

The SLT-equation of state describes the physics of a partially ionized gas at low temperatures and densities. A neutral plasma of charged particles recombines when the temperature is lowered sufficiently for a fixed density. When, on the other hand, the temperature is held fixed and the density is lowered the recombined entities dissociate for entropic reasons. In order to describe a partially recombined phase, these two antagonistic processes have to be in an equilibrium. It is highly non-trivial that the system is thermodynamically stable in the SLT-limit, which has been first proven by Fefferman [10]. The presented results are based on this SLT-analysis presented in full length in Ref. [13]. We use our numerical calculations of the cluster functions to implement corrections due to the clusters H_2^+ and H^- . For several thermodynamic quantities such as the pressure, the sound velocity and the inner energy, we are comparing our results to the OPAL-tables along the solar adiabat.

6.1.1 The Saha-equation

In the physical picture the Saha-equation is derived from the following expression for the pressure:

$$\beta P_{\text{Saha}} = \tilde{z}_e + \tilde{z}_p + \tilde{z}_e \tilde{z}_p (2\pi \lambda_{\text{ep}}^2)^{3/2} e^{-\beta E_{\text{H}}} \quad (6.1)$$

with $\tilde{z}_\gamma = \frac{(2\sigma_\gamma + 1)}{(2\pi \lambda_\gamma^2)^{3/2}} z_\gamma$ and $\lambda_{\text{ep}} = \sqrt{\frac{\hbar^2 \beta}{m_{\text{ep}}}}$,

where m_{ep} is the reduced mass of the electron-proton system. The first two terms correspond to the non-interacting electron/proton gas pressure, whereas the third term contains the recombination effects. We recognize that no κ -dependency whatsoever is present in this description, meaning that the long-range effects of the Coulomb potential are completely absent. The Saha-model neglects all interactions of the basic constituents e and p, apart from the possibility to form a Hydrogen atom in its ground state. We, therefore, cannot expect to deduce reliable results at high temperatures where either charge-charge interactions or excited states of the Hydrogen atom are present. The corresponding densities are derived from the thermodynamic relation $\rho_i = \tilde{z}_i \frac{\partial P}{\partial \tilde{z}_i}$. The neutrality implies that $\tilde{z}_e(\rho, \beta) = \tilde{z}_p(\rho, \beta) = \tilde{z}(\rho, \beta)$ and we can solve the equation of either the electron or the proton density

$$\rho_e = \rho_p = \rho = \underbrace{\tilde{z}}_{\rho_{\text{e,free}}} + \underbrace{\tilde{z}^2 (2\pi \lambda_{\text{e,p}})^{3/2} e^{-\beta E_{\text{H}}}}_{\rho_{\text{H}}} \quad (6.2)$$

for the fugacity \tilde{z} . In this way the Saha-equation is derived

$$\beta P_{\text{Saha}} = \rho + \frac{1}{2} \rho^* \left(\sqrt{1 + 4\rho/\rho^*} - 1 \right) \quad \text{with } \rho^* = (2\pi \lambda_{\text{e,p}}^2)^{-3/2} e^{\beta E_{\text{H}}} \quad (6.3)$$

and we do exactly see which kind of approximation of the full diagrammatic series this equation represents. The Saha-equation is valid if all contributions beyond the Hydrogen ground state are negligible. These conditions are fulfilled in a mutual limit $\rho \rightarrow 0, T \rightarrow 0$ with fixed ratio $\rho/\rho^* = \text{const}$, the so-called scaled-low-temperature limit (SLT), where the desired finite fraction of recombined particles is present. When comparing the two terms in equation (6.2) we see that partial recombination is achieved if

$$\tilde{z} = \gamma (2\pi \lambda_{\text{e,p}}^2)^{-3/2} e^{\beta E_{\text{H}}} = \gamma \rho^*, \quad (6.4)$$

where γ is a free parameter which determines the fraction of recombined particles $\rho_{\text{H}} = \gamma \rho_{\text{e,free}}$.

6.1.2 The SLT-limit and corrections to the Saha-equation

Since the Saha-equation contains the main process of recombination and is valid in the scaled-low temperature limit [36, 10], it is expected to be a good reference point for a subsequent expansion of the diagrammatic series. The SLT-expansion is exactly such a perturbative expansion of the full diagrammatic series around the Saha-equation. In a first step, the diagrams taken into account in the SLT-expansion are chosen carefully depending on their weight along the line of constant ionization. In a second step, the so derived series of diagrams is inverted perturbatively around the Saha solution to access the fugacities $z_e(\rho, \beta)$ for which the pressure is evaluated.

The precise procedure and the selection of diagrams are extensively described in Ref. [34]. During the derivation of the Saha-equation we have supposed that the e, p-cluster can be approximated by its ground state contribution. In general the virial coefficients (see equations (3.69) and (3.70)) depend on

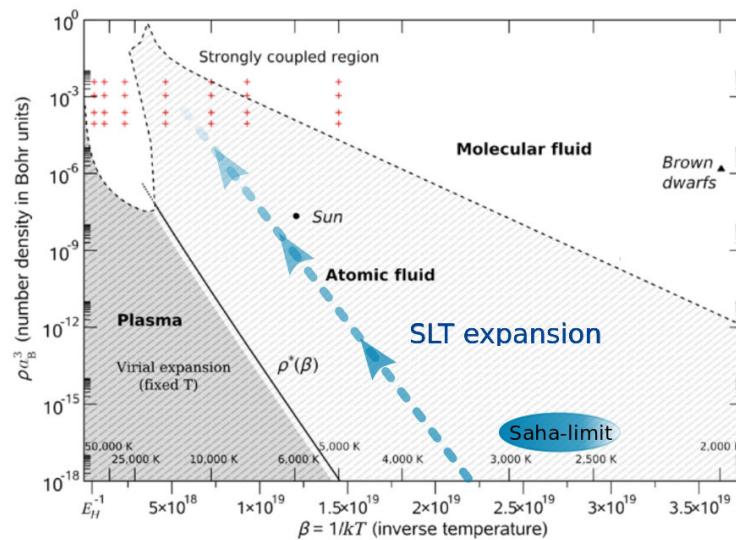


Figure 6.1: The phase diagram of a pure Hydrogen system. In the mutual limit $\rho \rightarrow 0, T \rightarrow 0$ with fixed ρ_e/ρ^* a finite fraction of particles stays recombined and the Saha-equation becomes exact. Corrections to the Saha-equation are derived in the scaled-low-temperature limit. Taking higher order terms in the SLT-expansion into account enables to move along the arrow in the direction of higher temperatures/densities, thus, extending the validity of the so derived equation of state.

the temperature as well as on the fugacities (\sim densities). The fugacity dependence is inherited from the long-range nature of the Coulomb potential which necessitates a RPA-type resummation. The cluster function can be split into a part, known as the truncated cluster function, which stays finite even if the limit $\kappa_D \rightarrow 0$ is considered and a part which diverges. The truncated cluster functions are dominated by their respective ground state contribution in the low-temperature limit. The terms of the genuine cluster function which diverge in the limit $\kappa \rightarrow 0$ are related to the long-range nature of the Coulomb potential. The truncation of the cluster functions, thus, arises naturally when extracting the contribution from a cluster function that dominates in the SLT-limit. We will dedicate the following subsection to clarify this reasoning. The SLT-expansion is an ordering of higher order processes with respect to their importance in the scaled-low-temperature limit. Most importantly, it provides exact expressions for the first corrections to the “ideal” Saha-equation in the SLT-limit.

6.1.3 Truncation of Cluster due to screening

In order to see, which corrections to the Saha-equation arise in the low-temperature low-density limit, we use the simple example of a two particle diagram

$$\begin{array}{c} \bullet \\ \text{e} \end{array} \text{---} \text{---} \begin{array}{c} \bullet \\ \text{p} \end{array} = e^{-\beta\phi} - 1 + \beta\phi - \frac{1}{2}(\beta\phi)^2, \quad (6.5)$$

which accounts for the interactions between electron and proton and, thereby, the formation of Hydrogen atoms. In the derivation of the Saha-equation we assumed that we can represent this cluster by its ground state partition function. The additional truncation present in the diagram $e^{-\beta\phi} - 1 + \beta\phi - 1/2(\beta\phi)^2$ in comparison to the usual virial coefficient $e^{-\beta V} - 1$ appears naturally due to the chain resummation giving rise to the potential ϕ . The only non-integrable term in the expansion of the above expression is the term

$1/6(-\beta\phi)^3$. In the function

$$B_2^T = \text{---} \text{---} \text{---} \text{---} - \text{---} \text{---} \text{---} = e^{-\beta\phi} - 1 + \beta\phi - \frac{1}{2}(\beta\phi)^2 + \frac{1}{6}(\beta\phi)^3 \quad (6.6)$$

we can, therefore, safely take the limit $\kappa \rightarrow 0$. The value of the related integral is dominated by the ground state contribution $e^{-\beta E_H}$ at low temperatures. The term $(-\beta\phi)^3$ has to be treated separately since it remains fugacity-dependent. It provides a contribution roughly given by

$$\tilde{z}^2 \int_0^\infty dr \frac{e^{-3r\kappa}}{|r+\lambda|^3} r^2 \sim \tilde{z}^2 \log(\kappa(z)\lambda). \quad (6.7)$$

Even though this integral, as a function of κ , becomes divergent in the limit $\kappa \rightarrow 0$, its contribution to the equation of state remains finite due to fugacity prefactors which tend to zero. In the above example of the term $(-\beta\phi)^3$, we should compare its weight to the ground state contribution of the Hydrogen cluster

$$\underbrace{\tilde{z}^2 \log(\kappa(\tilde{z})\lambda)}_{\phi^3\text{-Diagram}} \quad \text{to} \quad \underbrace{\tilde{z}^2 e^{-\beta E_H}}_{\text{ground state contribution}} \quad (6.8)$$

where $\kappa \sim \sqrt{\beta\tilde{z}}$ and $\tilde{z} \sim e^{\beta E_H}$ (see equation (6.4)), so that the term $(-\beta\phi)^3$ is sub-dominant in the SLT regime according to

$$e^{2\beta E_H} \beta E_H \ll e^{\beta E_H}, \quad (6.9)$$

i.e. it is exponentially smaller than the ground state contribution by a factor $e^{\beta E_H}$. The current version of the SLT-expansion contains terms up to the order $O(e^{\beta E_H})$, so that this term examined for pedagogical reasons, is actually taken into account. Apart from these estimations, the fact that the plasma is neutral leads to large compensations of these $(-\beta\phi)^3$ interactions between the several species

$$\begin{array}{cccc} \text{---} & \text{---} & \text{---} & \text{---} \\ \text{e} & \text{e} & \text{e} & \text{p} & \text{p} & \text{e} & \text{p} & \text{p} \end{array}, \quad (6.10)$$

which means that the overall contribution of these diagrams is even smaller than estimated above¹.

In summary, the truncated cluster coefficients are the parts of the cluster coefficients which stay finite, even if the screened potential is replaced by the bare Coulomb potential ($\kappa \rightarrow 0$). The so-called counter-terms (the opposite of the subtracted terms, here $1/6(-\beta\phi)^3$), where the limit $\kappa \rightarrow 0$ cannot be directly taken, are related to the long-range nature of the Coulomb potential. In general, the terms beyond Debye-type (maximum divergence in terms of κ allowed by the diagrammatic rules) are expected to be small. The same arguments to select the diagrams which give the first corrections to the Saha-equation in the SLT-limit have been applied in a more general context [34, 13]. The expression for the three particle cluster functions in the SLT are explicitly given in the Ref. [12], where these functions are also calculated numerically.

In the following, we will use these results in combination with the numerical calculation of the truncated three particle cluster coefficients [12] to evaluate the SLT-equation of state explicitly in the case of the Sun's adiabat.

¹In equation (6.10) all logarithmic divergent terms cancel out in the limit $\kappa \rightarrow 0$, due to the charge symmetry of the Hydrogen plasma, and the final contribution is of order $e^{2\beta E_H}$




6.2 Application of the SLT-expansion to the solar adiabat

The second quantum virial coefficient, which is closely related to the truncated two particle cluster coefficients, was first analytically calculated by Ebeling [55]. Higher order coefficients have not been calculated before, although they are needed to have a more precise description. These three particle diagrams account, in particular, for the contributions of the ions H_2^+ and H^- . We have calculated these functions numerically using the path integral formalism (see chapter 3). The prefactors arising from the expansion around the iso-ionization line in (ρ, T) space and the precise estimation and selection of diagrams to be taken into account are given in Ref. [13]. Using the numerically calculated truncated cluster function as well as the formulas given in Ref. [13], we trace the equation of state along the adiabat of the sun. Previous applications of the SLT-expansion [14] used approximations of the few-particle cluster functions and were, therefore, limited to low temperatures, preventing us from applying the theory to the Sun. The new tabulations of these cluster functions lift this restriction. The equation of the SLT-pressure is given by

$$P_{\text{SLT}} = P_{\text{Saha}} + P_1 + P_2 + P_3 + P_4 + P_5 + o(e^{\beta E_{\text{H}}}). \quad (6.11)$$

The explicit expressions for the partial pressures $P_i(\beta, \rho)$ can be found in Ref. [14]. The ordering of the successive corrections to the Saha equation result from the competition of exponentially growing factors associated with the bound states of recombined entities beyond the Hydrogen ground state on one hand, and exponentially decaying factors arising from the fugacities on the other hand.

We content ourselves with stating the physical processes from which the corrections $P_1 \dots P_5$ originate:

- P_1 : Debye plasma polarization 
- P_2 : arises from 4 particle diagrams, in particular H_2 molecules
- P_3 : implements thermal excitations of the Hydrogen cluster and charge-charge interactions 
- P_4 : accounts for the ions H_2^+ , H^- and atom charge interactions
- P_5 : Debye plasma polarization beyond P_1 arising from 

When we compare our data to the OPAL tables, which is shown in figure 6.2, we recognize a good accordance of the SLT and the OPAL-prediction (relative deviations are at most $3 \cdot 10^{-3}$). It can be seen very clearly how the SLT interpolates between the Saha-equation, which is valid for low temperatures, and the virial-expansion, valid in the high-temperature regime. Plotting the different corrections predicted by the SLT-equation of state P_i , we see that the main corrections to the Saha-equation are caused by classical Debye-diagrams (P_1, P_5). The contributions of H_2^+ and H^- (P_4) are confined to a very small region and are in magnitude almost negligible. The speed of sound c , which is essentially given by the adiabatic coefficient Γ , is a key quantity in helioseismology and, thus, it is interesting to compare the SLT and the OPAL prediction for Γ . Using standard thermodynamic relations, we can deduce the internal energy per particle

$$u = \frac{\partial}{\partial \beta} \left(2\beta\mu - \frac{\beta P}{\rho} \right) \Big|_{\rho} \quad (6.12)$$

where $\mu(\beta, \gamma) = E_{\text{H}} + \beta^{-1} \left(\ln(\gamma) + \ln(m_{\text{e}}/m_{\text{e,p}})^{3/4} / 4 \right)$, see equation (6.4). In this manner the formula

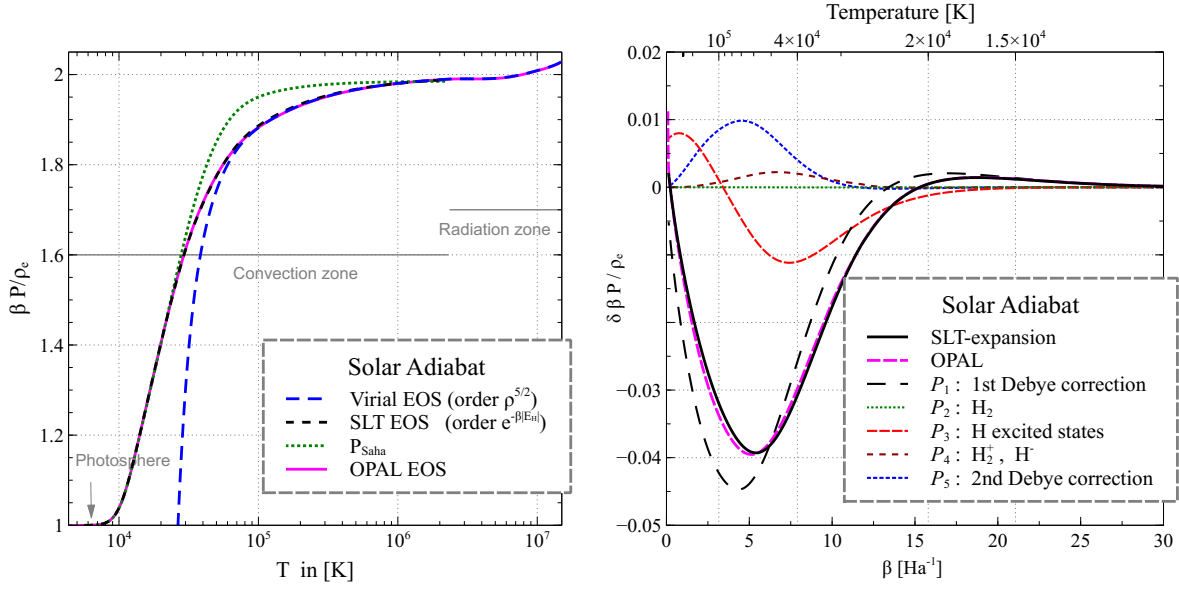


Figure 6.2: Left: The pressure along the adiabat of the Sun. The SLT-expansion interpolates between the Saha-equation and the virial-expansion. Right: The different corrections P_1 - P_5 to the Saha-equation predicted by the SLT-expansion along the adiabat of the Sun. We find a almost perfect accordance with the OPAL-predictions.

for the internal energy

$$u = \left(2 - \frac{\beta P}{\rho}\right) E_H + \frac{3P}{\rho} + 2 \frac{\partial \ln(\gamma)}{\partial \beta} - \frac{\rho^*}{\rho} \frac{\partial \beta P / \rho}{\partial \beta} \quad (6.13)$$

is derived, which can be evaluated for given ρ , for each correction P_i separately, yielding the related corrections of the internal energy u_i [14]. We have performed a similar analysis based on fundamental thermodynamic relations to compute the adiabatic exponent Γ from the knowledge of the function $P(\rho, T)$ and $u(\rho, T)$ via

$$\Gamma = \frac{\rho}{P} \underbrace{\frac{\partial P}{\partial \rho}}_{c^2} \Big|_s = \frac{\rho}{P} \left(\frac{\partial P}{\partial \rho} \Big|_T + \frac{T}{\rho^2 c_V} \left(\frac{\partial P}{\partial T} \Big|_\rho \right)^2 \right) \quad (6.14)$$

with

$$c_V = T \frac{\partial S/N}{\partial T} \Big|_V = \frac{\partial u}{\partial T} \Big|_\rho. \quad (6.15)$$

The adiabatic coefficient and the internal energy per particle are shown in figure 6.4. We see that the corrections u_1 , u_5 and u_3 are dominant as it has been found for the pressure. We, again, remark an almost perfect agreement with the OPAL-table data in the whole temperature regime for both, the adiabatic coefficient Γ and the inner energy u .

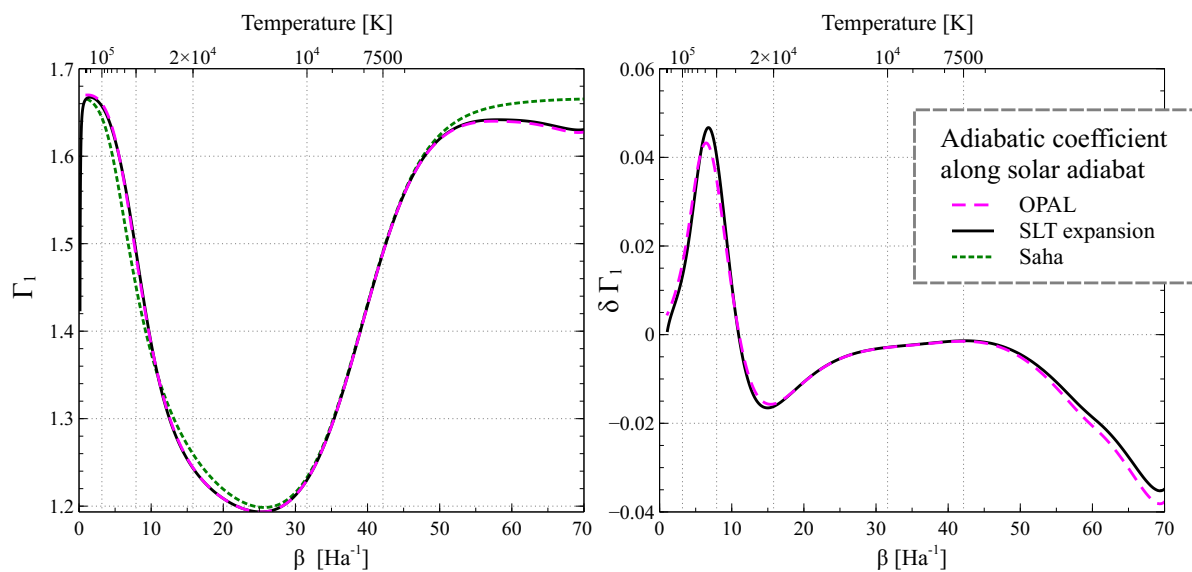


Figure 6.3: Left: The Adiabatic coefficient Γ predicted by the SLT-equation of state along the adiabat. Right: The difference with respect to the Saha-prediction.

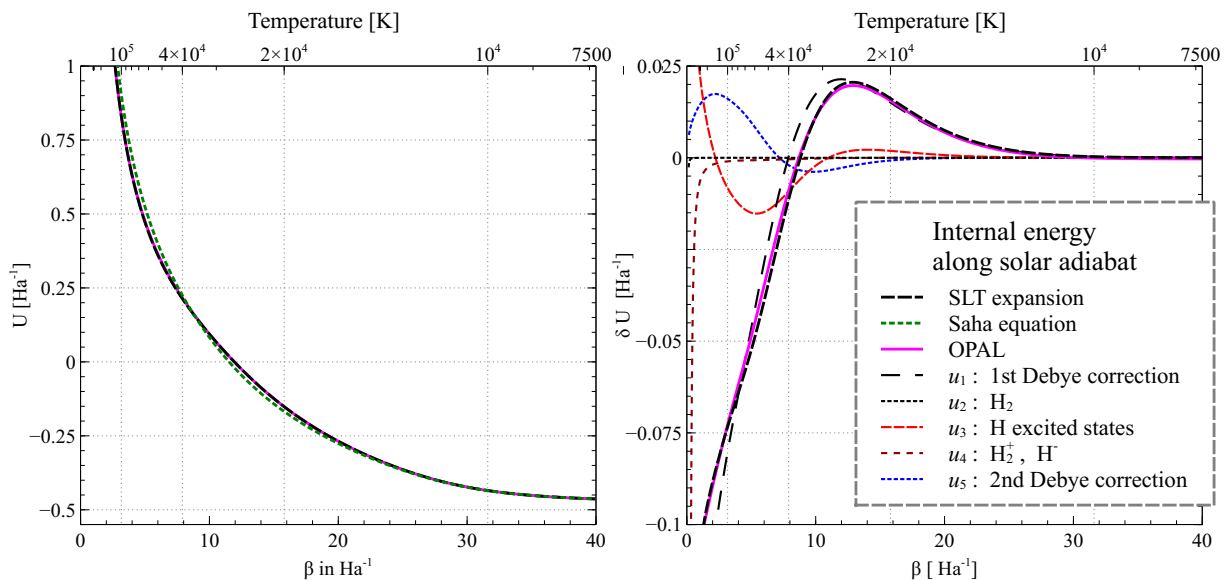



Figure 6.4: Left: The inner energy predicted by the SLT-equation of state along the adiabat. Right: The difference with respect to the Saha-prediction.

6.3 A simple approximation inspired by the SLT-expansion

The derivation of the SLT-expansion starts with a development of the particle densities in terms of fugacities, which afterwards is inverted perturbatively around the Saha-equation. This leads to the SLT-expansion (6.11) of the pressure in terms of the densities. Here, we propose a simple approximation scheme within the diagrammatic series of the pressure in terms of the fugacities, directly inspired by the SLT considerations, but which avoids the perturbative inversion to access the equation of state. The model pressure is given by

$$\beta P^{\text{SLT}_{\text{inv}}} = \tilde{z}_e + \tilde{z}_p + \tilde{z}_e \tilde{z}_p C_{e,p} + \frac{1}{2} \tilde{z}_e^2 C_{2p} + \frac{1}{2} \tilde{z}_e^2 C_{2e} + \underbrace{\frac{\kappa_D^3}{12\pi}}_{\sim(\tilde{z}_e + \tilde{z}_p)^{3/2}} + \underbrace{e^2 \beta \frac{\kappa_D^4}{32\pi}}_{\sim(\tilde{z}_e + \tilde{z}_p)^2} + \frac{1}{4} \tilde{z}_e^2 \tilde{z}_p^2 Z_{\text{H}_2}. \quad (6.16)$$

In this simple model, three particle terms have been neglected since their contributions are expected to be small according to the above analysis, in particular in comparison with the Debye-type corrections. The term $\beta \kappa_D^4$ originates from the diagram . The two-body functions occurring in the SLT-pressure (6.16) are given in terms of Ebeling's functions Q and E [24]. The explicit formulas for the two particle cluster functions in the SLT-limit, are given by

$$C_{ep}(\beta) = (2\pi\lambda_{ep}^2)^{3/2} \left[Q\left(-\sqrt{2m_{ep}/m_e} E_H \beta\right) + \frac{4\pi e^6 \beta^3}{12} \ln(m_{ep}/m_0) \right] \quad (6.17)$$

$$C_{ee}(\beta) = (2\pi\lambda_{ee}^2)^{3/2} \left[Q\left(-\sqrt{2m_{ee}/m_e} E_H \beta\right) - \frac{1}{2} E\left(-\sqrt{2m_{ee}/m_e} E_H \beta\right) - \frac{4\pi e^6 \beta^3}{12} \ln(m_{ee}/m_0) \right] \quad (6.18)$$

$$C_{pp}(\beta) = (2\pi\lambda_{pp}^2)^{3/2} \left[Q\left(-\sqrt{2m_{pp}/m_e} E_H \beta\right) - \frac{1}{2} E\left(-\sqrt{2m_{pp}/m_e} E_H \beta\right) - \frac{4\pi e^6 \beta^3}{12} \ln(m_{pp}/m_0) \right]. \quad (6.19)$$

The last term is related to the divergent integrals (see equation (6.10)) representing ‘‘counter-terms’’ to the truncation². The mass m_0 can be chosen arbitrarily since it cancels out when the proper combination, leading to a neutral plasma, of those $\beta^3 \log(m_\gamma/m_0)$ terms is considered³. To model the presence of the H_2 in the plasma, we have included a phenomenological partition function

$$Z_{\text{H}_2}(\beta) = (2\pi\lambda_e^2)^3 \left(2\pi\lambda_{\text{H}_2}^2\right)^{3/2} e^{-\beta E_{\text{H}_2}} \frac{1}{1 - e^{-\beta E_{\text{vib}}}} \sum_{l=0}^{\infty} (2l+1) e^{-l(l+1)\beta E_{\text{rot}}}, \quad (6.20)$$

given by a simple rotator-vibrator model [14]⁴. The density corresponding to the SLTs pressure model is given by⁵

$$\rho_e^{\text{SLT}_{\text{inv}}} = \tilde{z} + \frac{1}{2} \tilde{z}^2 (C_{ee} + 2C_{ep} + C_{pp}) + \frac{\kappa^3}{8\pi} + \frac{e^2 \beta \kappa^4}{32\pi} + \frac{1}{2} \tilde{z}_e^2 \tilde{z}_p^2 Z_{\text{H}_2}. \quad (6.21)$$

Now, we will invert the equation (6.21) in a non-perturbative manner, *i.e.* we numerically compute $z(\rho, \beta)$. Once this inversion is performed, we evaluate the model pressure for the resulting fugacity $z(\rho, \beta)$, which

²The third order term contained in the function Q does not give any contribution due to cancellations in the occurring combination $2Q_{ep} - Q_{ee} - Q_{pp}$

³This exact cancellation is only present in the case of a symmetric plasma (e, p). When allowing for the α -particles the cancellation will not hold, and the result will be m_0, κ dependent.

⁴The reduced mass of the four particle system is given by $\frac{1}{m_{\text{H}_2}} = \frac{2}{m_e} + \frac{2}{m_p}$.

⁵We remember that the fugacities are dressed by neutrality bond **before** the densities are derived by differentiation and the pseudo-neutrality ($\tilde{z} = \tilde{z}_e = \tilde{z}_p$) is invoked.

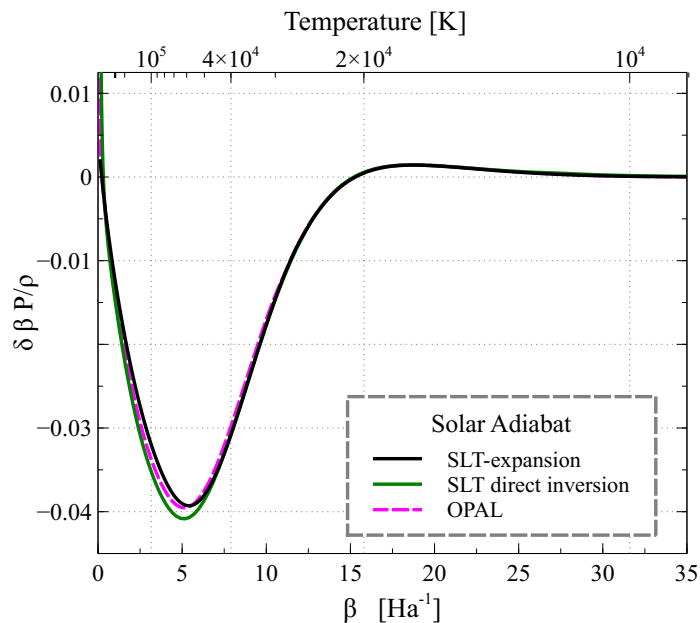


Figure 6.5: The SLT-equation of state together with the direct inversion (in green) result along the adiabat of the sun. The difference of the SLT-expansion and the numeric inversion are negligibly and confirm the accuracy of the SLT-expansion. The deviation from the SAHA-pressure is mainly determined by classical Debye-corrections P_1 and P_5 .

provides the equation of state $P(\rho, \beta)$. It is surely beneficial to exactly solve the equations for the densities without the perturbative inversion around the Saha-equation. When doing so, less approximations are made in contrast to the perturbative inversion around the Saha-equation. This procedure will also enable us to quantify the accuracy of the perturbative inversion around the Saha-equation. Another advantage of this approach is that we can also include terms, which lead to the formation of H_2 . Using the perturbative inversion, this is not immediately achievable due to the fact that for low temperature the recombination to H_2 leads to a large deviation from the Saha equation and, therefore, we would have to include a large number of terms. This approach, *i.e.* direct inversion of the density equations to find the fugacities, will also be used in chapter 7.

Results

The result of the exact inversion is illustrated in figure 6.5, and shows a very good accordance with the SLT-expansion prediction, where three particle effects have been neglected $P = P_1 + P_3 + P_5$. As input data we use the GONG solar model [70], where we assume that only Hydrogen is present. The difference of these two curves can then be attributed to the contribution of higher order terms in the perturbative expansion around the Saha-equation. The accordance with the OPAL-equation of state is, as already expected, striking. The main deviations of the three curves are confined to the intermediate temperature regime where the actual recombination is taking place. In figure 6.6 we plot the equation of state for several isochores for the exact inversion of the SLT-model and the OPAL-tables.

At large densities and high temperatures, on the other hand, the OPAL-equation of state predicts a larger pressure than the Saha-equation of state. For two selected densities we provide the plot of differential pressure (see figure 6.7), to make the reader sensitive to the similarity of the OPAL and the SLT-model. The same accordance is seen in the adiabatic coefficient (see figure 6.8), which essentially

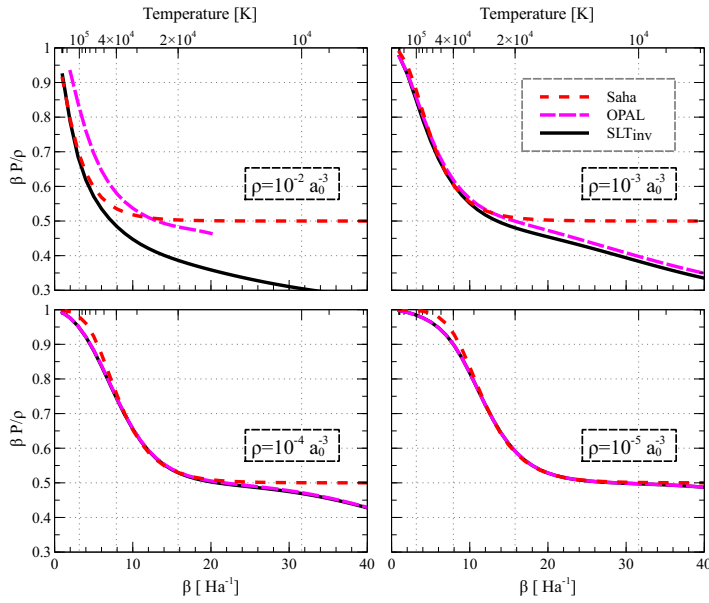


Figure 6.6: The pressure of the different models for several values of ρ . For low densities the models become indistinguishable, whereas for higher densities the differences of the models are visible.

determines the speed of sound

$$c^2 = \left. \frac{\partial P}{\partial \rho} \right|_{S/\rho} = \frac{P}{\rho} \Gamma. \quad (6.22)$$

For low temperatures the recombination of two atoms to a Hydrogen molecule reduces the pressure and has a large impact on the adiabatic coefficient.

We have to admit that for high densities (as for example $\rho = 10^{-2} a_0^{-3}$) the screening constant κ is too large for our low-density for low-temperature expansion to make reliable predictions. The applicability of the equation of state proposed here is based on the assumption of a small value of κ . This assumption is fulfilled in the high temperature regime $\kappa \sim \sqrt{\beta}$ as well as in the low temperature regime where the screening constant is small due to a large fraction of recombined particles. The problematic region is, therefore, the intermediate temperature regime, where the screening constant is neither suppressed by the temperature nor by a low number of free particles.

6.4 Conclusions

The SLT-expansion provides reliable easy-to-use expressions for the equation of state of a pure Hydrogen plasma for reasonably low densities. In this context, the numerically calculated three-body cluster functions have been used to improve the SLT-equation of state. We have not only compared pressure and inner-energy but also the adiabatic coefficient predicted by these models. With the help of the simple model, inspired by the SLT-expansion, where we inverted the density equations numerically, we have verified that the SLT-expansion is reliable for solar conditions. This direct inversion of the SLT-density equation enabled us to probe also the low temperature regime, where the Saha-equation loses its validity

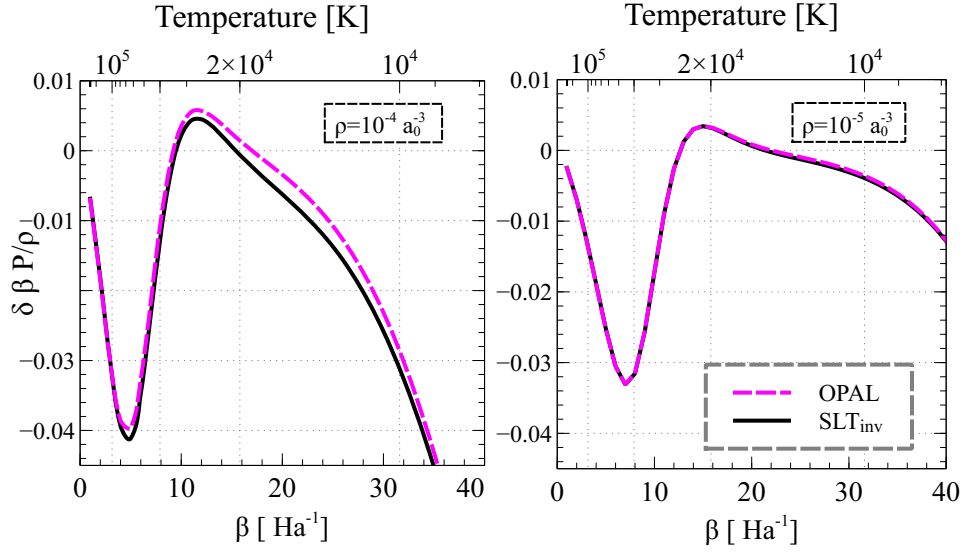


Figure 6.7: The differential pressure shown for the SLT and the OPAL-model for two selected densities. We recognize that the difference of these two models is generally of the order of 1‰.

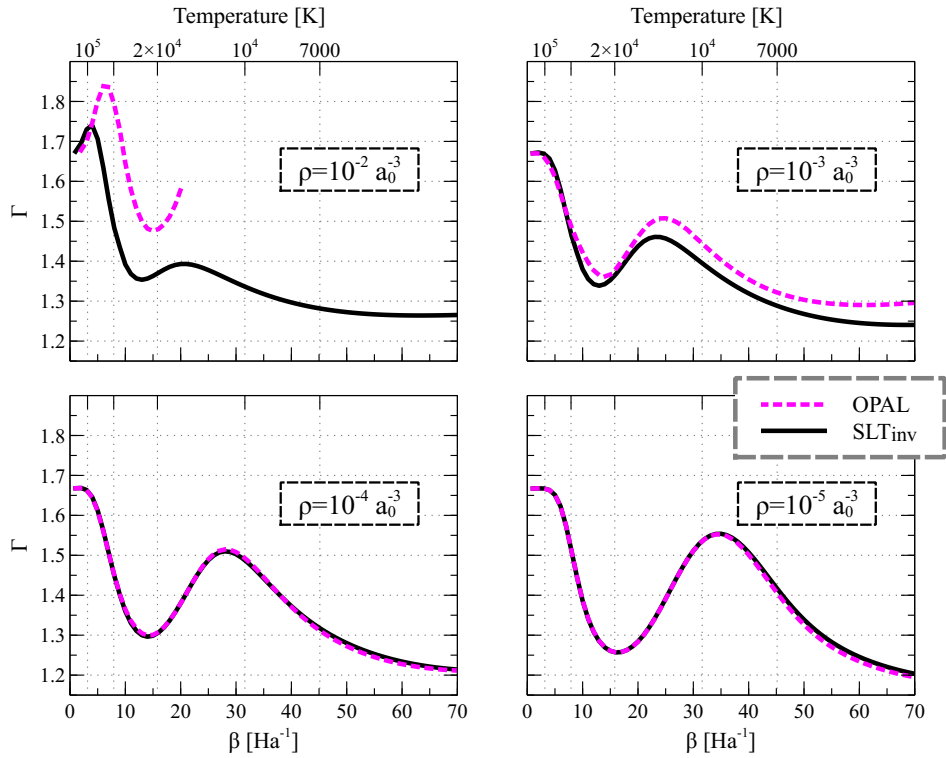


Figure 6.8: The adiabatic coefficient Γ for the different models and several densities. The “kinks” mark the different recombination stages (first Hydrogen atoms then at lower temperatures, then H_2 molecules). The models are in good overall accordance.

due to the fact that Hydrogen atoms recombine to form H_2 ⁶. The numerical inversion of the density equations can be implemented very easily and is numerically not demanding, so that this equation of state is very appropriate for on-line use. The direct calculation of the equation of state has the advantage that grid errors due to the discretization of the OPAL-tables are avoided. Furthermore, the accordance of the equation of state, inspired by the SLT considerations, and the OPAL-tables enables us to better quantify the ingredients used to generate these tables. In the following chapter we will use the numerically calculated κ -dependent cluster functions instead of its vacuum counterparts, arising naturally in the SLT limit, in order to improve our description of the intermediate-temperature regime.

⁶In this regime, the basic assumption of the SLT expansion, namely that we can perturb around the Saha-equation of state, is not valid.

Chapter 7

Equation of State of the Hydrogen-Helium Mixture

In this chapter we will use the numerically calculated cluster functions (see chapter 5) to derive the equation of state in the context of the diagrammatic expansion introduced in chapter 3. In the first part of this chapter we investigate the impact of these numerical cluster functions in the case of a Hydrogen plasma by comparing to the SLT and the OPAL-predictions. The main difference of the approach, extensively discussed in this chapter, and the SLT-expansion is that we do not restrain ourselves to the low-temperature low-density regime. In particular, we will neither consider a low-density limit $\kappa \rightarrow 0$ for the cluster functions nor will we invert the fugacity expansion around the ideal Saha-equation perturbatively. Furthermore, we exactly invert the density equations, so that no small parameter is needed¹. The direct inversion of the density equations is purely of technical nature, whereas the κ -dependence of the cluster functions gives rise to new physical effects. Since the SLT-equation is expected to hold in a large regime, namely when the density and the temperature are sufficiently low, we expect the changes, related to the screened cluster functions, to occur at rather high densities and temperatures.

After first tests on the pure Hydrogen gas we add the α -particles to our system, allowing for the formation of He and He⁺. The inclusion of the α -particles in our equations opens two important additional recombination channels ($e + \alpha \rightarrow \text{He}^+$, $e + \text{He}^+ \rightarrow \text{He}$) and, thus, the equation of state of the Hydrogen-Helium mixture will have more features than the pure Hydrogen equation of state. As a reference model in the Hydrogen-Helium case, we introduce a generalization of the Saha equation, which also accounts for the ideal recombination to He and He⁺, in addition to the ideal recombination to Hydrogen.

In the following, we will gradually improve the equation of state starting from a very simple model. For each introduced correction, we plot the new equation of state along several isochores and the adiabat of the Sun, our primary system of application. We will compare each of these successively introduced models with the OPAL-tables which are widely accepted in the literature. There have been several papers studying the differences of the OPAL-tables and other equations of state, in particular those using the free energy approach (chemical picture). For this reason, and also because the OPAL-equation of state is regarded as the most accurate for solar-like conditions [71], we deliberately compare our results only with the OPAL-tables. We will see that the Sun is an almost ideal system and that the differences between our models and the OPAL-tables along the adiabat of the Sun are small. When increasing the density, non-ideal behavior occurs as the κ -dependence of the cluster functions becomes more important.

¹For the perturbative inversion used in the SLT-expansion the small parameter is the deviation from the Saha-equation.

The fugacity expansion proposed here is thermodynamically consistent in the sense that we can deduce all thermodynamic quantities by their usual thermodynamic identities from the diagrammatic series of the pressure. Consequently, all terms in the pressure series do have their counterpart in the diagrammatic series of such quantities. Due to the usual thermodynamic relations ($\rho_i = z_i^{\partial\beta P/\partial z_i}$ for example), a model is completely specified by its pressure series. We will, therefore, in general only give the diagrammatic series of the pressure.

First, we will explain how this procedure, that uses the κ -dependent cluster functions, can be implemented in practice. Afterwards we present our actual results for several successive approximations of the full pressure series in comparison to the OPAL-tables.

7.1 The implementation of the fugacity expansion

As mentioned before, in the physical picture an equation of state is completely determined by the series for the pressure. In practice, the full pressure series (equation (3.20)) is truncated, and only a finite number of diagrams is taken into consideration. The cluster functions appearing in the pressure series depend through κ on the fugacities. Given a pressure model, the densities are deduced by applying the operator $\rho_i = z_i^{\partial\beta P/\partial z_i}$.

Having calculated the cluster functions by our path-integral Monte-Carlo code (section §5.4 on page 61), we use Mathematica to construct a two-dimensional interpolating function of κ and β . Using these interpolating functions we can generate the function $P(\{z\}, \beta)$ within Mathematica. This function provides the densities via the usual relation. Internally, Mathematica directly evaluates the derivatives and constructs the densities as linear combinations of interpolating functions. Derivatives acting on bonds in the diagrammatic language, will be present through the κ -dependence of the cluster functions.

The interpolation of an exponentially growing function by a polynomial is problematic. Therefore, we divide the raw numerical data representing the cluster function by its exponential asymptote before we interpolate and remultiply the interpolating function by the same exponential afterwards. This procedure leads to easily polynomially interpolable functions and ensures numerical accuracy.

In the next step, the equations for the densities $\rho(\{z\}, \beta)$, which have been deduced from the expression for the pressure of a given model, are inverted for a given configuration of densities in order to find the related fugacities. With the help of these fugacities, we can evaluate the original pressure expression and thereby obtain the equation of state in its usual form $P(\rho, \beta)$.

The advantage of this approach is that thermodynamic consistency is trivially fulfilled. Furthermore, all thermodynamic series beyond the pressure are automatically calculated by Mathematica, which minimizes sources of errors (wrong prefactors, missing terms...) in the rather involved expressions. Once their relation to the pressure is given, expressions for other thermodynamic quantities, such as the sound velocity or the entropy², can be derived in a similar manner. One of the main advantages of this strategy is that the physical picture, which is often considered complicated and inflexible, becomes modular and easily examinable. Once the code implementing the relations between the thermodynamic quantities ($P \rightarrow \rho$, $P \rightarrow \Gamma$, ...) and the inversion of the density equations is written, different models can be easily examined, by solely changing the expression for the pressure.

²We recall that in the Grand canonical ensemble, the pressure is essentially the Grand canonical potential.

7.2 The selection of diagrams

The full diagrammatic series of the pressure involves an infinite number of diagrams from which we have to choose a finite set. We are going to select the diagrams according to the number of particles they contain, where the particles hidden in the resummed potential are not counted. The two and three particle clusters, we defined in section §3.6 and calculated in chapter 5, present only a subset of diagrams made with two or three particles respectively.

The one-body diagrams we have to consider are given by

$$\begin{aligned}
 \mathcal{G}_1 &= \bullet + \underbrace{\text{Debye diagram}} + \text{diagram with two loops} + \text{diagram with three loops} + \dots \\
 &= \tilde{z} \left(e^{\frac{e_\gamma^2 \beta \kappa}{2}} - \frac{e_\gamma^2 \beta \kappa}{2} + \frac{e_\gamma^2 \beta \kappa}{3} \right).
 \end{aligned} \tag{7.1}$$

For our numerical calculations of the cluster functions, we have used the approximation that the intermediate particles of the chain resummation (see equation (3.38)) are classical ($\lambda_\gamma = 0$). To preserve consistency, we have, therefore, to consider the particles in the attached rings to be classical as well. The attached classical rings generally dress the bare fugacities by a factor of $e^{e_\gamma^2 \beta \kappa / 2}$. An exception is the Debye diagram, indicated in equation (7.1), which has a special weight of $\frac{\kappa^3}{12\pi}$ (see equation (3.46) and equation (3.47) on page 32). In the following, we will refer to the diagrams which are not contained in the definition of the cluster function we calculated numerically, as the **Screened Long Range** diagrams (SLR). This class of diagrams strongly depends on the screening constant κ . The diagram which provides the Debye-correction is already contained in the class of diagrams SLR1 (see equation (7.1)).

According to the above definition of the particle number of a diagram, all two particle diagrams are given by

$$\begin{aligned}
 \mathcal{G}_2 &= \text{diagram with two nodes and a ring} + \text{diagram with two nodes and two loops} + \text{diagram with two nodes and three loops} + \dots \\
 &\quad + \text{diagram with two nodes and two loops (different orientation)} + \text{diagram with two nodes and three loops (different orientation)} + \dots \\
 &= \text{diagram with two nodes and a ring} + \text{diagram with two nodes and a ring (different orientation)},
 \end{aligned} \tag{7.2}$$

where we remind the reader that all fugacity factors of the cluster functions are dressed by attached rings as well. The diagram $\bullet \text{---} \bullet$ vanishes due to the pseudo-neutrality condition. The second diagram which is absent in the above series of diagrams, $\bullet \text{=} \bullet$, is suppressed by the demand that no bare node can be part of a convolution. We remind the reader of shorthand notation

$$\begin{aligned}
 \text{diagram with node and ring} &= \text{diagram with node and one loop} + \text{diagram with node and two loops} + \text{diagram with node and three loops} + \dots \\
 &= \tilde{z} \left(e^{\frac{e_\gamma^2 \beta \kappa}{2}} - 1 \right),
 \end{aligned} \tag{7.3}$$

which is very useful in the three body case. The formula for the SLR2 diagrams is explicitly given by

$$\beta P_{\text{SLR2}} = \beta P_{\text{SLR1}} + \frac{1}{2} \tilde{z}_{\gamma_1} \left(e^{\frac{e_{\gamma_1}^2 \beta \kappa}{2}} - 1 \right) \tilde{z}_{\gamma_2} \left(e^{\frac{e_{\gamma_2}^2 \beta \kappa}{2}} - 1 \right) \left(\frac{4\pi e_{\gamma_1} e_{\gamma_2} \beta}{\kappa^2} + \frac{\pi e_{\gamma_1}^2 e_{\gamma_2}^2 \beta^2}{\kappa} \right). \quad (7.4)$$

The three particle clusters are defined by the diagrams

$$\begin{aligned} \mathcal{G}_3 = & \text{[Diagram: Circle with } \mathcal{G}_3 \text{]} + \text{[Diagram: Triangle with 3 nodes]} + \text{[Diagram: Triangle with 2 nodes]} + \text{[Diagram: Triangle with 2 nodes]} \\ & + \text{[Diagram: Triangle with 2 nodes]} + \text{[Diagram: Triangle with 2 nodes]} + \text{[Diagram: Triangle with 2 nodes]} \\ & + \text{[Diagram: Triangle with 2 nodes]} + \text{[Diagram: Triangle with 2 nodes]} \\ & + \text{[Diagram: Triangle with 2 nodes]} + \text{[Diagram: Triangle with 2 nodes]}. \end{aligned} \quad (7.5)$$

$$\begin{aligned} & + \text{[Diagram: Triangle with 2 nodes]} + \text{[Diagram: Triangle with 2 nodes]} \\ & \underbrace{\hspace{10em}}_{\text{Dressing of fugacities in bonds}}. \end{aligned} \quad (7.6)$$

The three particle diagrams shown in equation (7.6) respect the diagrammatic rules given in figure 3.4. The attached rings provide only a multiplicative factor depending on the actual species they are attached to. We can carry out the analysis of the SLR diagrams and find

$$\begin{aligned} \beta P_{\text{SLR3}} = & \beta P_{\text{SLR1}} + \beta P_{\text{SLR2}} \\ & + \frac{1}{6} \tilde{z}_{\gamma_1} \left(e^{\frac{e_{\gamma_1}^2 \beta \kappa}{2}} - 1 \right) \tilde{z}_{\gamma_2} \left(e^{\frac{e_{\gamma_2}^2 \beta \kappa}{2}} - 1 \right) \tilde{z}_{\gamma_3} \left(e^{\frac{e_{\gamma_3}^2 \beta \kappa}{2}} - 1 \right) \\ & \left(\frac{3\pi^2 e_{\gamma_1}^2 e_{\gamma_2}^2 e_{\gamma_3}^4 \beta^4}{\kappa^2} + \frac{8\pi^2 e_{\gamma_1}^2 e_{\gamma_2}^3 e_{\gamma_3}^3 \beta^4}{3\kappa^2} - \frac{4\pi^2 e_{\gamma_1}^2 e_{\gamma_2}^2 e_{\gamma_3}^2 \beta^3}{\kappa^3} - \frac{2\pi^2 e_{\gamma_1}^1 e_{\gamma_2}^2 e_{\gamma_3}^3 \beta^3}{\kappa^3} \right) \\ & + \frac{1}{6} \tilde{z}_{\gamma_1} \left(e^{\frac{e_{\gamma_1}^2 \beta \kappa}{2}} - 1 \right) \tilde{z}_{\gamma_2} \left(e^{\frac{e_{\gamma_2}^2 \beta \kappa}{2}} - 1 \right) \tilde{z}_{\gamma_3} \\ & \left(\frac{3\pi^2 e_{\gamma_1}^2 e_{\gamma_2}^2 e_{\gamma_3}^4 \beta^4}{\kappa^2} - \frac{2\pi^2 e_{\gamma_1}^1 e_{\gamma_2}^2 e_{\gamma_3}^3 \beta^3}{\kappa^3} \right) \\ & + \frac{1}{6} \tilde{z}_{\gamma_1} \left(e^{\frac{e_{\gamma_1}^2 \beta \kappa}{2}} - 1 \right) \tilde{z}_{\gamma_2} \tilde{z}_{\gamma_3} \frac{8\pi^2 e_{\gamma_1}^2 e_{\gamma_2}^3 e_{\gamma_3}^3 \beta^4}{3\kappa^2} \end{aligned} \quad (7.7)$$

Last two diagrams in equation (7.6) are allowed since the convolution point is not a bare node. The value of the diagrams can be conveniently inferred by the κ -dependence of the numerically calculated cluster functions

$$\begin{aligned} & \text{[Diagram: Triangle with 2 nodes]} + \text{[Diagram: Triangle with 2 nodes]} \\ & = \tilde{z}_{\gamma_1} \tilde{z}_{\gamma_2} e^{\frac{(e_{\gamma_1}^2 + e_{\gamma_2}^2) \beta \kappa}{2}} \sum_{\gamma} \tilde{z}_{\gamma} \left(e^{\frac{e_{\gamma}^2 \beta \kappa}{2}} - 1 \right) \frac{\partial}{\partial \tilde{z}_{\gamma}} \text{[Diagram: Triangle with 2 nodes]}. \end{aligned} \quad (7.8)$$

We will use these definitions of particle clusters throughout the following analysis. The SLR diagrams do not contain any exchange loops for the reason that these exchange terms are suppressed by an additional fugacity factor.

7.3 The equation of state of the pure Hydrogen system

The equation of state of a plasma for conditions, for example, found in the Sun is of major importance. We will gradually develop the model equation of state incorporating the Debye, two particle and three particle corrections to the Saha-equation. The present approach is tested and validated by comparing its predictions to those of the OPAL and of the SLT equations of state. The quantities are shown in the following figures as deviation $P - P_{\text{Saha}}$ from the Saha-prediction, due to the fact these corrections remain small.

In the SLT-approach, the full cluster function was split into two parts: one integrable in the limit $\kappa \rightarrow 0$ and one where this limit cannot be taken. The non-zero screening constant κ has only been considered for the parts of the cluster functions which are not integrable. This approximation is avoided when using the κ -dependent cluster functions. These functions are numerically calculated for several temperatures and simultaneously for appropriate values of the screening constant κ . Once these objects are known, the equation of state is a linear combination of them where the combinatorial prefactors are those deduced with the help of our Quantum-Mayer formalism (see equation (3.20) on page 26 and figure 3.4 on page 32).

The two particle equation of state for pure Hydrogen

In these terms the pressure involving all two-body clusters is given by the diagrams

$$\beta P_{\text{SCH2}} = \begin{array}{c} \textcircled{1e} \\ \textcircled{1p} \\ \textcircled{1p, 1e} \\ \textcircled{2e} \\ \textcircled{2p} \\ \textcircled{e^2} \end{array} . \quad (7.9)$$

This equation of the pressure defines the **Screened-Cluster-Hydrogen two-body model (SCH2)**. This dressing of the ‘‘internal’’ particles of a cluster is necessary to assure the correct compensation of first order corrections of the cluster ground state (see discussion in section §4.1). Notice that in these diagrams containing two electrons, exchange contributions are taken into account via the introduction of loops made with two particles ($q = 2$ in the last diagram in equation (7.9)).

The three particle equation of state of pure Hydrogen

With the above definition of the screened cluster functions, the inclusion of the three particle cluster functions in the equation of state model is straightforward. The **Screened-Cluster-Hydrogen three-body (SCH3)** approximation for the pressure is given by

$$\begin{aligned} \beta P_{\text{SCH3}} = & \begin{array}{c} \textcircled{1e} \\ \textcircled{1p} \\ \textcircled{1p, 1e} \\ \textcircled{2e} \\ \textcircled{2p} \\ \textcircled{e^2} \\ \textcircled{2p, 1e} \\ \textcircled{1p, 2e} \\ \textcircled{1p, e^2} \\ \textcircled{3e} \\ \textcircled{1e, e^2} \\ \textcircled{e^3} \\ \textcircled{3p} \end{array} . \end{aligned} \quad (7.10)$$

This model includes all three body effects, and all exchange effects, which crucially intervene in recombined entities like H^- .

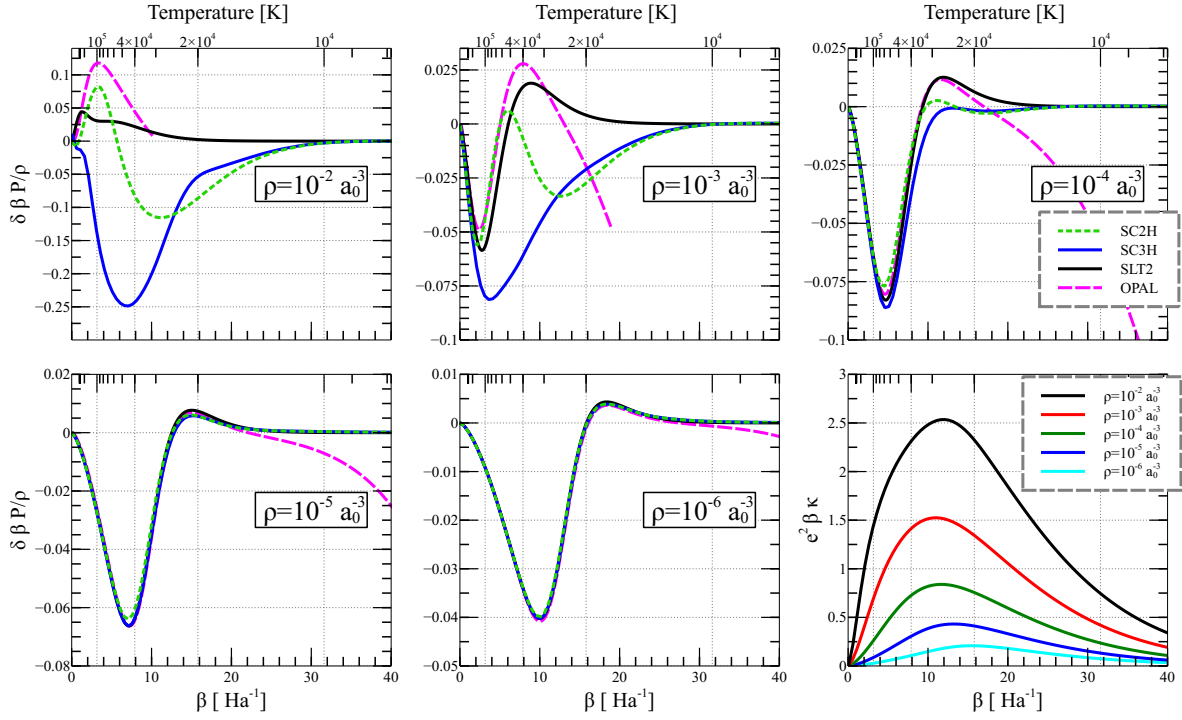


Figure 7.1: The results of the two models SCH2 and SCH3 in comparison with the SLT and the OPAL predictions for several isochores. For low densities the four models are indistinguishable apart from the low-temperature regime (H_2 is currently not modeled in our approaches). For higher densities the effects of the κ -dependence of the cluster functions is clearly visible.

Results

We examine the predictions of the above defined models (SCH2 and SCH3) along several isochores and along the adiabat of the Sun. After the deduction of the densities by differentiation³, we numerically invert the resulting equations to find the fugacities and together with them the pressure as a function of the density. We remind the reader that the value of κ is determined by the densities of the free particles $\rho_{\gamma, \text{free}} = \tilde{z}_\gamma$. In this way, the screening constant is consistent with the diminishing fraction of free particles when bound entities are formed.

The results of this procedure for our two models are shown in figure 7.1 for several isochores $10^{-2} \geq \rho a_0^3 \geq 10^{-6}$. For comparison the OPAL and the SLT-prediction for the pressure is shown alongside. For low densities the deviation of the pressure with respect to either the SLT or the OPAL prediction is small. Only in the intermediate-temperature regime, where the particles are neither forming Hydrogen atoms nor the temperature is so high that the free terms are dominating, deviations from the SLT-equation of state are visible. The OPAL-model also contains contributions of H_2 molecules, which is indicated by the descent of the pressure at low temperatures. Since the models studied here do not contain contributions of four-particle clusters, we can only compare with the OPAL-tables in regions where the H_2 abundances are negligible.

For low-density isochores the impact of the κ -dependence of the cluster functions is almost negligible

³In practice the derivatives are taken internally by Mathematica, which returns an interpolating function representing this derivative and thereby the density. The diagrammatic rules corresponding to the differentiation are summarized in figure 3.5 and we could use these rules to determine the density series, too. We have deliberately chosen not to do so due to the sheer complexity of the diagrammatic density series.

and, thus, the accordance of either the SCH2 or the SCH3-model with the SLT prediction is very good. When increasing the density, on the other hand, the κ -dependence of the cluster functions give important corrections (see for example $\rho = 10^{-3} a_0^{-3}$ in figure 7.1). As expected, the effect of the three-body terms is attractive most of the time, as the combination of cluster function appearing in the third virial coefficient is positive in most cases (see figure 5.10 on page 65). This can be seen best by comparing the SLT-prediction and the SCH2-model since the models take the same particle clusters into account, apart from the SLR-diagrams⁴.

We have seen that we were not able to calculate the three particle cluster function very reliably for low temperatures. Retrospectively, this does not pose a problem since the three particle terms are only giving vanishingly small contributions for these temperatures. The difference between the two models SCH2 and SCH3 becomes smaller with decreasing density, due to the suppression of the three-body diagrams by fugacity factors. The strength of coupling between ionized charges is determined by the quantity $e^2\beta\kappa$ which is shown alongside.

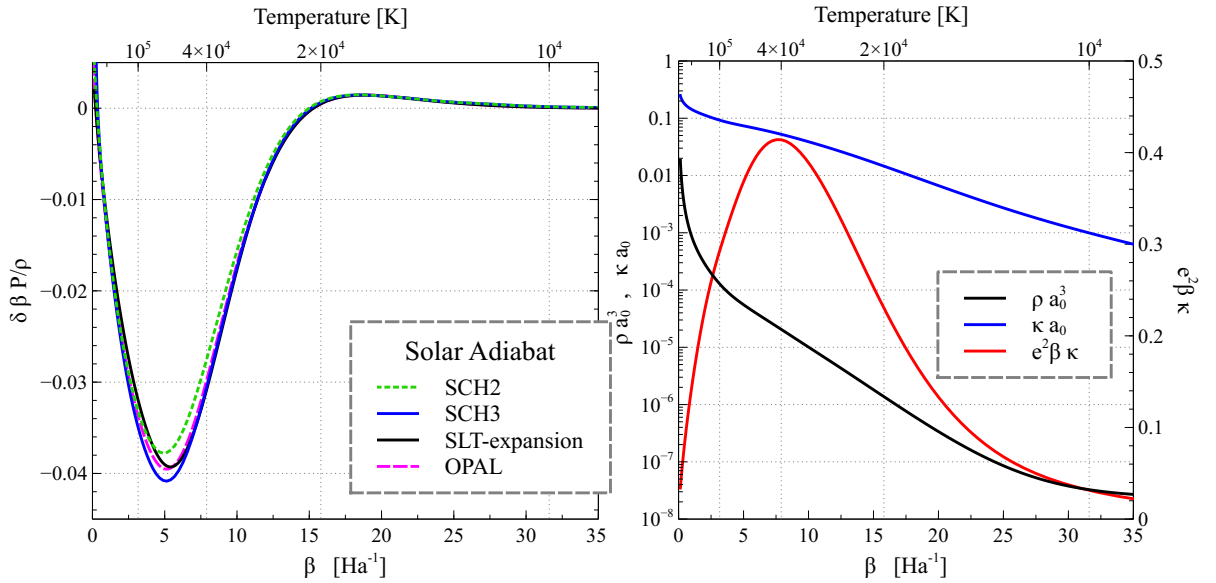


Figure 7.2: The predictions of the different pure Hydrogen models along the adiabat of the Sun. As input data we used the GONG solar model [70], where we assumed that only Hydrogen is present. To give the reader an impression of the parameter range, alongside the temperature-density profile as well as the screening constant κ and the Debye-parameter $e^2\beta\kappa$ is shown.

In figure 7.2 the results along the adiabat of the Sun are shown [70], where we assumed that the whole density is made up of Hydrogen and no α -particles are present. The differences between the reference models and our predictions are very small, and again deviations are only found in the intermediate-temperature regime. This can be attributed to the fact that the plasma under solar condition is a relatively diluted and an almost ideal mixture of free particles and Hydrogen atoms. Alongside the temperature-density profile of the adiabat, screening parameter κa_0 , controlling the importance of the κ -dependence of the cluster functions, and the “Debye”-parameter $e^2\beta\kappa$ are shown. The fact that κa_0 is small along the adiabat leads to the accordance of the SLT-expansion, which is valid in the limit $\kappa \rightarrow 0$, and our models.

⁴We have verified that the source of the deviation is not the difference of the SLR-diagrams these models take into account.

In conclusion, by using the κ -dependent cluster functions, we were first of all able to reproduce the results of the SLT-expansion and the OPAL-tables in the low-density regime. In this regime the equation of state of the plasma can very accurately be described by an ideal mixture e, p and Hydrogen atoms, where the only non-ideality present are the SLR-diagrams (essentially the Debye-correction). For higher densities we have seen what kind of effects the κ -dependence of the cluster functions on the equation of state have. The contribution of some clusters can be negligible in the low-temperature regime, due to the lack of bound states (for example the 3e-cluster), but it can be essential at higher temperatures. In the intermediate-temperature regime our models predict in general a smaller pressure than the two references.

There has been a long debate of how to implement **pressure ionization** in the equation of state (see Ref. [20] for example). It is usually assumed that the pressure of the system increases when the ground state is destroyed due to the screening process. The Saha equation of state neglects the screening process completely and, therefore, assumes that the atomic ground state is unaffected by the screening constant. Thus, pressure ionization would manifest itself in a larger pressure than the “ideal” Saha pressure. For the here studied conditions where the screening length can be as large as $\kappa^{-1} \sim 6a_0$, we do not see such an effect. It is remarkable that even for high densities ($\rho = 10^{-2}a_0^{-3}$) the pressure predicted by our models is smaller than the “ideal” Saha pressure. When their fugacity factors are not dressed by attached “rings”, the κ -dependent cluster functions are actually tending to zero with increasing screening parameter κ . These attached rings compensate for the decrease of the bare cluster functions and, therefore, the overall contribution of a certain particle cluster to the equation of state remains stable. We conclude that, even though states of the particle clusters are destroyed by a large screening constant κ , the contribution to the pressure of the cluster functions is only slightly affected and, for our parameter regime, no pressure ionization is found. To make more precise statements we would need to probe the equation of state at even higher densities, for which higher few-body clusters would have a crucial importance. Furthermore, we used a semi-classical approximation for the inter-particle potential (see equation (4.24) on page 46) in our calculations of the cluster functions. This approximation is questionable in the regime where $\kappa\lambda$ is not a small quantity, so that we cannot draw definite conclusions.

After this first study involving the κ -dependent cluster functions we will in the following apply the same approach to the Hydrogen-Helium mixture.

7.4 The equation of state of the Hydrogen-Helium mixture

7.4.1 General considerations

The presence of the α -particles breaks the symmetry of the charges. Cancellations between diagrams involving different species will be less efficient and the equation of state will show more features than in the pure Hydrogen case. In particular, the equation of state will be influenced by the two additional recombination channels, $e + \alpha \rightarrow \text{He}^+$ and $e + \text{He}^+ \rightarrow \text{He}$. It is useful to consider a generalization of the Saha-equation, which allows for the formation of these bound states, as a reference model. This generalization of the Saha-pressure is given by

$$\begin{aligned} \beta P_{\text{Saha}} = & \tilde{z}_e + \tilde{z}_p + \tilde{z}_\alpha + \tilde{z}_e \tilde{z}_p (2\pi\lambda_{\text{H}}^2)^{3/2} e^{-\beta E_{\text{H}}} \\ & + \tilde{z}_e \tilde{z}_\alpha (2\pi\lambda_{\text{He}^+}^2)^{3/2} e^{-\beta E_{\text{He}^+}} + \frac{1}{4} \tilde{z}_e^2 \tilde{z}_\alpha (2\pi\lambda_e^2)^{3/2} (2\pi\lambda_{\text{He}}^2)^{3/2} e^{-\beta E_{\text{He}}}. \end{aligned} \quad (7.11)$$

The first terms represent the ionized charges e, p and α , whereas the following terms allow for the ideal recombination to Hydrogen, He^+ and Helium. The symmetry factor of the Mayer-diagram representing Helium is given by $1/2$, but due to the anti-symmetry of the ground state in spin-space an additional factor of $1/2$ is present, yielding a prefactor of $1/4^5$. We will refer to this model in the following still as the Saha-equation of state as for the pure Hydrogen case, due to their similarity. As the usual Saha-equation only the ideal recombination processes are modeled.

The neutrality of the plasma imposes a condition on the densities of the different species

$$\rho_e - \rho_p - 2\rho_\alpha = 0. \quad (7.12)$$

In the pure Hydrogen case the neutrality of the system implied that both, the electron density ρ_e and the proton density ρ_p , are equal. For the Hydrogen-Helium mixture, the neutrality of the system together with the total density ρ is not sufficient to determine the number densities of the three elementary particles. Therefore, the Hydrogen-Helium mixture needs to be characterized by an additional parameter, which can be chosen freely. We have chosen the parameters

$$\rho = 2\rho_p + 3\rho_\alpha \quad (7.13)$$

$$\alpha = \frac{\rho_\alpha}{\rho_\alpha + \rho_p}. \quad (7.14)$$

where ρ_γ is the number density of species γ measured in units of the Bohr radius a_0 ($\rho_\gamma [a_0^{-3}]$) and ρ is the total particle number density $\rho = \rho_e + \rho_p + \rho_\alpha$.

In figure 7.3 we show the prediction for the pressure of the ‘‘Saha’’-equation for $\alpha = 1/2$ (same number of protons and α -particles) and $\rho = 10^{-6} a_0^{-3}$ together with the ‘‘generalized’’ abundances⁶

$$\rho_{C_{\{\gamma\}}} = \tilde{z}_e \frac{\partial \beta P_{C_{\{\gamma\}}}}{\partial \tilde{z}_e} + \tilde{z}_p \frac{\partial \beta P_{C_{\{\gamma\}}}}{\partial \tilde{z}_p} + \tilde{z}_\alpha \frac{\partial \beta P_{C_{\{\gamma\}}}}{\partial \tilde{z}_\alpha}. \quad (7.15)$$

This quantity can be seen as the overall density created by the presence of the particle cluster $C_{\{\gamma\}}$ in the pressure model. It is in sharp contrast to the usual abundances which are directly related to the number density of a certain chemical species. The reason why we called the abundances ‘‘generalized’’ is indicated by the red question mark. At first glance it seems that at temperatures of around $\beta \sim 5 \text{ Ha}^{-1}$, the beforehand fixed number of free protons increases. This is a consequence of the dressing of each of the diagrams with the neutrality bond (see equation (3.67) on page 37) to be able to impose the neutrality of the system on the level of fugacities. The neutrality bonds lead, for example, to the appearance of the He^+ cluster in the equation of the proton density ρ_p , even though the He^+ cluster contains no proton (it there appears with a minus sign). We assure the reader that the number density ρ_γ of each of the fundamental species is constant.

In figure 7.3 the three recombination stages can be clearly identified: First the α -particles recombine with a free electron to form He^+ . At lower temperatures these He^+ particles attract another electron and recombine to He. At last, the free protons recombine with the remaining free electrons to form Hydrogen atoms.

The here presented simple ‘‘Saha’’-model contains only ideal recombination. Many-particle effects, for example, present in the SLR-diagrams (essentially the famous Debye-correction) or the κ -dependent

⁵The Helium ground state is an anti-symmetric singlet in the electron spin space $\psi_0 \sim \frac{1}{\sqrt{2}} (|\downarrow\uparrow\rangle - |\uparrow\downarrow\rangle)$ and, therefore, the spins are not independent.

⁶Remember that all fugacities are dressed with neutrality bonds.

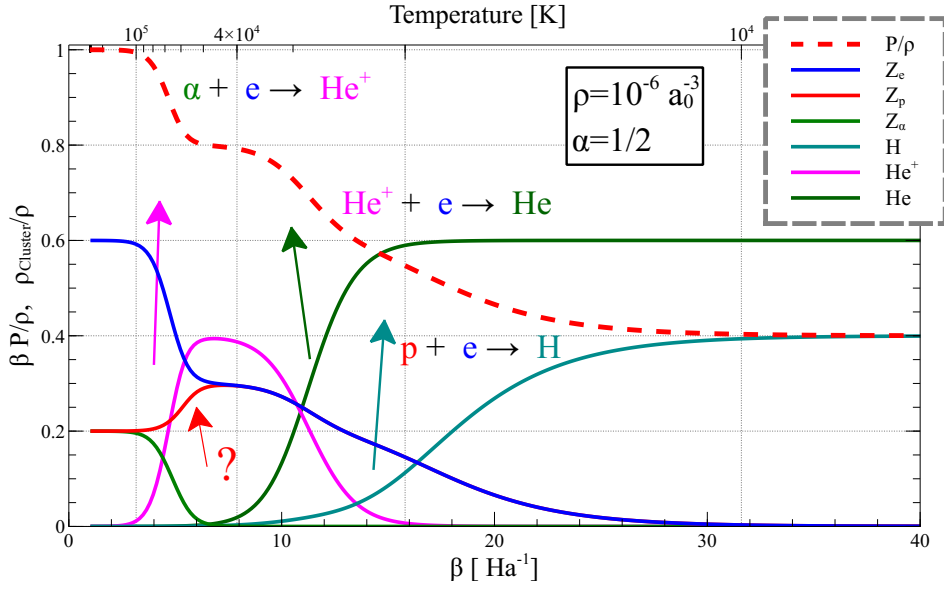


Figure 7.3: The “generalized” abundances for the different clusters present in the Saha equation are shown along with the equation of state for $\rho = 10^{-6} a_0$ and $\alpha = 1/2$. The three recombination stages can be clearly seen in the curve for the pressure as well as in the curves of the abundances. These abundances cannot be interpreted as the actual number of chemical species but rather tell us the fraction of the total densities created due to the presence of a certain chemical species. Since our system is neutral a He^+ particle cannot exist on its own but has to be accompanied by either an electron or a “negatively counted” proton. This leads to the fact that the density related to the bare proton cluster increases in the high-temperature region, even though the overall number of protons is fixed. A neutral cluster has not to be accompanied by any other particle, and thus their abundances are the actual particle density fractions. The origin of this peculiarity is the dressing of the fugacities by the neutrality bond.

cluster functions, are neglected. In the following, we will first present and then study our model, which incorporates these effects, and compare its predictions to the OPAL-tables.

7.4.2 The Hydrogen-Helium model with three-body interactions

The Screened-cluster-Hydrogen-Helium-model is given by the pressure model

$$\begin{aligned}
 \beta P_{\text{SCHHE}} = & \begin{pmatrix} 1e \end{pmatrix} + \begin{pmatrix} 1p \end{pmatrix} + \begin{pmatrix} 1\alpha \end{pmatrix} + \begin{pmatrix} 1p, 1e \end{pmatrix} + \begin{pmatrix} 1e, 1\alpha \end{pmatrix} + \begin{pmatrix} 1p, 1\alpha \end{pmatrix} \\
 & + \begin{pmatrix} 2e \end{pmatrix} + \begin{pmatrix} 2p \end{pmatrix} + \begin{pmatrix} 2\alpha \end{pmatrix} + \begin{pmatrix} e^2 \end{pmatrix} \\
 & + \begin{pmatrix} 1p, 2e \end{pmatrix} + \begin{pmatrix} 2p, 1e \end{pmatrix} + \begin{pmatrix} 1\alpha, 2e \end{pmatrix} + \begin{pmatrix} 1\alpha, 2p \end{pmatrix} + \begin{pmatrix} 2\alpha, 1e \end{pmatrix} + \begin{pmatrix} 2\alpha, 1p \end{pmatrix} \\
 & + \begin{pmatrix} e, p, \alpha \end{pmatrix} + \begin{pmatrix} 3e \end{pmatrix} + \begin{pmatrix} 3p \end{pmatrix} + \begin{pmatrix} 3\alpha \end{pmatrix} \\
 & + \begin{pmatrix} 1p, e^2 \end{pmatrix} + \begin{pmatrix} 1\alpha, e^2 \end{pmatrix} + \begin{pmatrix} e^3 \end{pmatrix} .
 \end{aligned} \tag{7.16}$$

This approximation of the pressure takes all three-body cluster functions, but those related to the exchange of protons or α -particles, into account. As before, all fugacity factors of the cluster functions are dressed by attached loops to account for the compensation of first order corrections in κ (see discussion in chapter 4). The related equations for the densities ρ_γ are again deduced by differentiation **after** each fugacity factor has been dressed by the neutrality bond (see equation (3.67)). At this point, the reader might understand why we have first of all decided only to give the expressions for the pressure of a model and, secondly, why we use Mathematica to derive the density equations.

7.4.3 The reduced Hydrogen-Helium model

We compare our full-model, where all 21 numerically calculated cluster functions are taken into account, with a minimal model, containing only a modest number of clusters. This will enable us to specify the importance of non-ideal contributions and, due to the fact that we also include a phenomenological model for the Hydrogen-molecule cluster, give insights in the content of the OPAL-tables. This reduced model $\text{SCHHE}_{\text{red}}$ is given by the pressure:

$$\beta P_{\text{SCHHE}_{\text{red}}} = \begin{array}{ccccccc} \bullet & + & \bullet & + & \bullet & & \\ e & & p & & \alpha & & \\ & + & \textcircled{1e, 1p} & + & \textcircled{1e, 1\alpha} & + & \textcircled{2e, \alpha} & + & \textcircled{2e, 2p} & + \beta P_{\text{SLR3}}, \end{array} \quad (7.17)$$

where the H_2 -cluster function is approximated by a vibrator rotator model [14]. The essential Debye-term is present in this model through the SLR3-diagrams. For the remaining cluster functions, we use the ground state partition functions, which is indicated by the lighter color of the clusters. This will enable us to examine the importance of the “non-ideal” behavior of the particle clusters. We will see that this simple model captures already most of the corrections to the “Saha”-equation of state and is in good accordance with the OPAL-tables.

7.4.4 Results

The results for $\alpha = 1/4$, three times more protons than α -particles, are shown in figure 7.4 for several total densities ρ .

The equation of state of the Hydrogen-Helium mixture shows three recombination stages (see figure 7.4 and figure 7.5): First, electrons and α -particles recombine to He^+ -particles, afterwards the Hydrogen recombination process starts. The He^+ particles attract part of the remaining free electrons to form Helium atoms. The actual order of the two processes $e + p \rightarrow \text{H}$ and $e + \text{He}^+ \rightarrow \text{He}$ depends on the specific configuration of the plasma ρ, α . This cascade can be clearly seen in the plots of the pressure for low densities, but is smeared out for large densities. With increasing density, the suppression of the Helium diagram due to an additional fugacity factor becomes less severe, and, therefore, the Helium recombination process can start already at relatively high temperatures. The He^+ recombination process can also be seen in the plot of the screening parameter κa_0 , where it leads to the “kink” at high temperatures. As is shown by figure 7.5, the presence of other clusters than the ideal ones (z_γ , He , He^+ , H and the Debye terms) is only of importance for high densities.

For a better examination of the differences between the OPAL-equation of state and our results, the difference with respect to the Saha pressure $\beta \delta P$ is shown in figure 7.6. Both curves show in general similar behavior, apart from the low-temperature region where the contribution of H_2 -molecules becomes

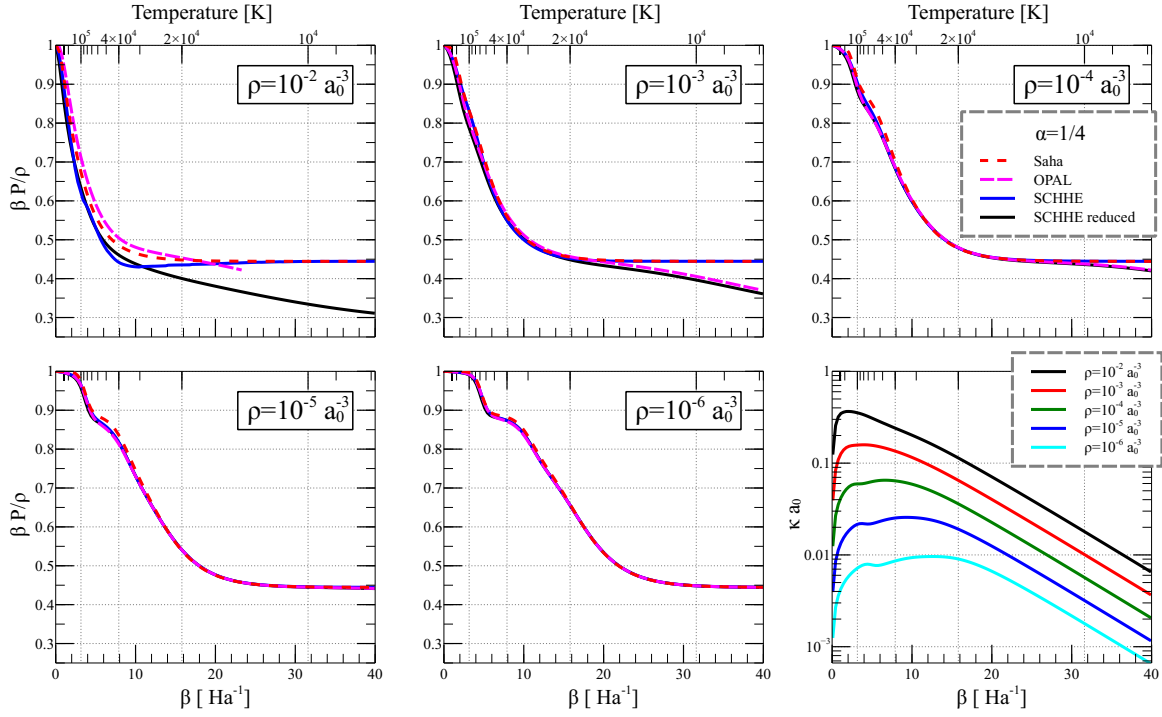


Figure 7.4: Several isochores of the equation of state of the Hydrogen-Helium mixture for the models SCHHE and SCHHE_{red} in comparison with the Saha equation and the OPAL-prediction. In the plot of the screening parameter κa_0 , we can see a “kink” at about $\beta = 5 \text{ Ha}^{-1}$, which is related to recombination $e + \alpha \rightarrow \text{He}^+$.

relevant. In this regime the reduced model SCHHE_{red} is in good accordance with the OPAL-prediction. Two “kinks” are present in the high-temperature regime which mark the recombination stages.

For low densities and high temperatures both models are fairly equivalent ($\rho < 10^{-4} a_0^{-3}$, $\beta < 2 \text{ Ha}$). Due to the charge $e_\alpha = 2e$ of the α -particles their contribution to the screening constant is important. Nevertheless, the parameters κa_0 and $e^2 \beta \kappa$ are smaller than for a pure Hydrogen gas with the same number density. This is a consequence of the free electrons recombining with the α -particles to form He^+ already at high temperatures. A lower value of the screening constant κ does not necessarily mean a larger pressure since the particles either recombine or contribute to a Debye diagram. For low densities the three models predict globally the same deviations from the ideal Saha pressure. This deviation is mostly given by the SLR-terms (Debye-terms): These clusters are absent in the Saha-equation and, as can be seen in figure 7.5, a relatively large fraction of particles is counted in these “SLR-clusters“. At high densities, on the other hand, deviations become large as the few-body clusters gain importance.

For high temperatures and high densities our model predicts a larger pressure than the OPAL-equation of state and the reduced model. An exception is the $\rho = 10^{-2} a_0^{-3}$, where the density is so large that the Debye-parameter $e^2 \beta \kappa \gg 1$ is not small (see figure 7.6). For these densities the prediction of our models are not reliable since they are based on an expansion in the particle number.

In summary, the difference of the cluster function-model and the OPAL-equation of state is never larger than 2%, at least for reasonable densities $\rho < 10^{-3} a_0^{-3}$.

Increasing the fraction of α -particles to $\rho_\alpha = \rho_p$ ($\alpha = 1/2$), the contribution of He and He^+ becomes more important and the pressure decreases faster than for $\alpha = 1/4$ (see figure 7.7). For these conditions the recombination cascade is more pronounced. In figure 7.8 we examine again the differences of the

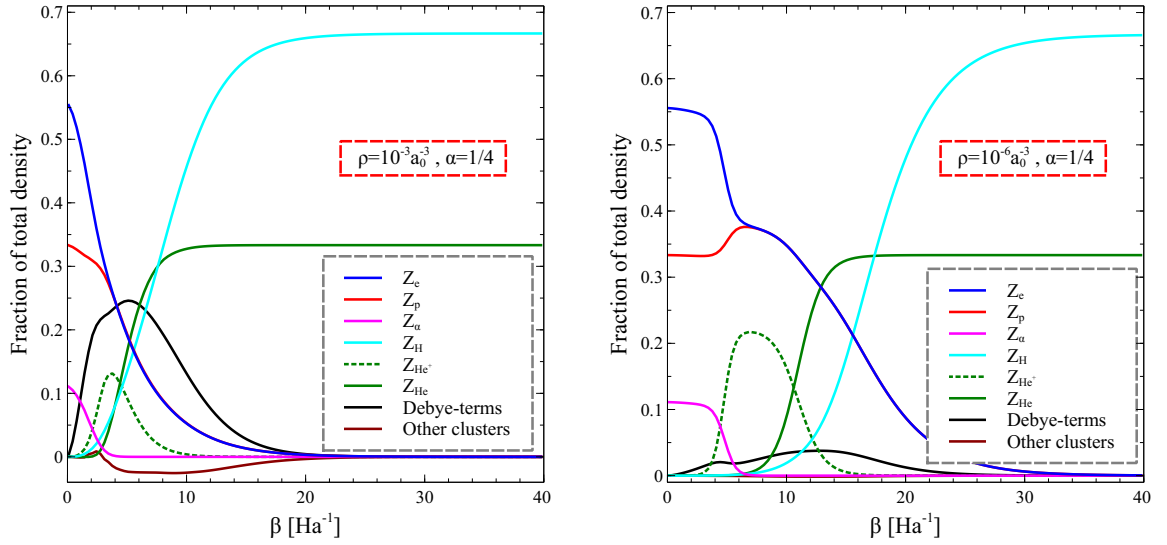


Figure 7.5: The “generalized” abundances for $\alpha = 1/4$ along two adiabats. We recognize that three particle clusters beyond the explicitly shown are completely negligible at low densities. For higher densities their contribution is only of importance for rather high temperatures. We remark again the “kink” due to the He^+ recombination process in the abundances of the Debye terms (SLR-diagrams). In general the recombination processes are shifted to higher temperature when the density is increased.

three models with respect to the ideal Saha-pressure. For low densities and low temperatures where the cluster functions are dominated by their ground states the results of the three models coincide. This is also true for high temperatures as three particle clusters are for these conditions negligible as well. In the intermediate-temperature regime our model equation of state predicts a larger pressure than the reduced cluster function-model. This is an indicator for the importance of the three-body cluster functions beyond Helium.

To conclude this section we present the results along the solar adiabat in figure 7.9. The OPAL and the reduced model prediction of the pressure are in good accordance. The fact that the complete cluster function model predicts a larger pressure can be traced back to the importance of three particle clusters. In general the full cluster function predicts a larger pressure in the intermediate-temperature regime than the reference models.

In the temperature regime where He^+ recombines with free electrons to form Helium, our SCHHE model has shown unnatural “kinks” in the plots of screening constant κ as well as in the Debye abundances (see for example figures 7.4 and 7.5). This is a strong indicator that the screening provided by He^+ particles is of importance in these parameter regimes. In the next subsection, therefore, we explain how we can account for screening by the charged He^+ -particles and examine the so generated model.

7.4.5 Contribution of He^+ ions to screening

One drawback of the SCHHE-model we explored in the previous section is that, even though He^+ atoms are charged and present at intermediate temperatures (see figure 7.5), we completely neglected their contribution to screening. The He^+ contribution to the screening constant can be accounted for during the chain-resummation, which leads to the screened loop-loop potential (see section §3.4.1). In the long wavelength limit the separation between the α -particle and the electron is negligible. The He^+ -particles, therefore, can be identified with an effective particle to which we can assign a fugacity during the chain

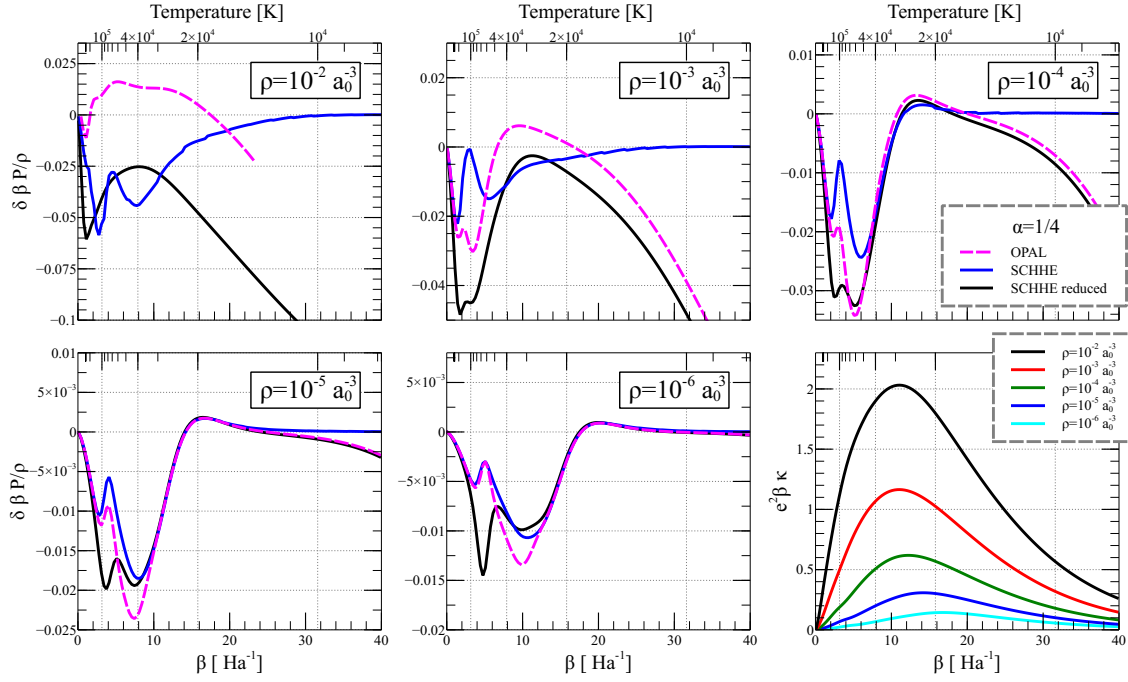


Figure 7.6: For better comparison of our results and the OPAL-predictions the difference with respect to the Saha equation is shown. We recognize that differences of our models and the OPAL-tables are confined to the intermediate-density regime, where the actual recombination processes take place. In this regime, the models show in general the same features but with different intensity. We will see that for low densities ($\rho \leq 10^{-4} a_0^{-3}$) the differences of the SCHHE-model and the OPAL-tables can mainly be attributed to the fact that we have not taken He^+ into account in the screening parameter κ . For higher densities the three particle clusters and the κ -dependence of the cluster function become important.

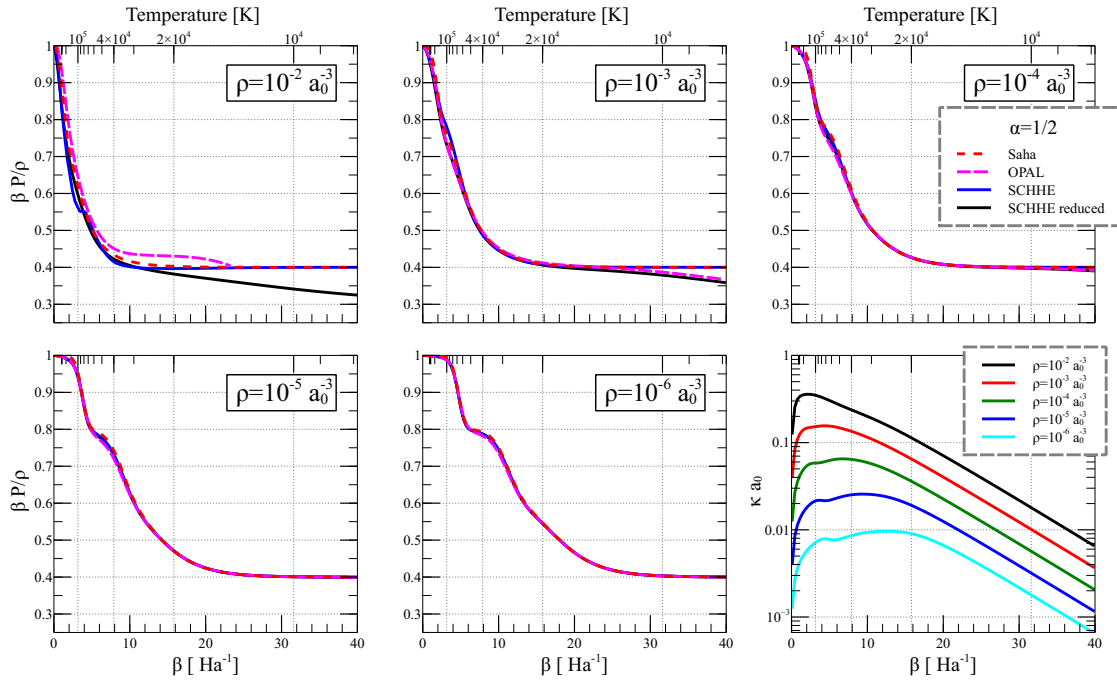


Figure 7.7: The pressure along selected isochores for $\alpha = 1/2$, an equal number of proton and α -particles.

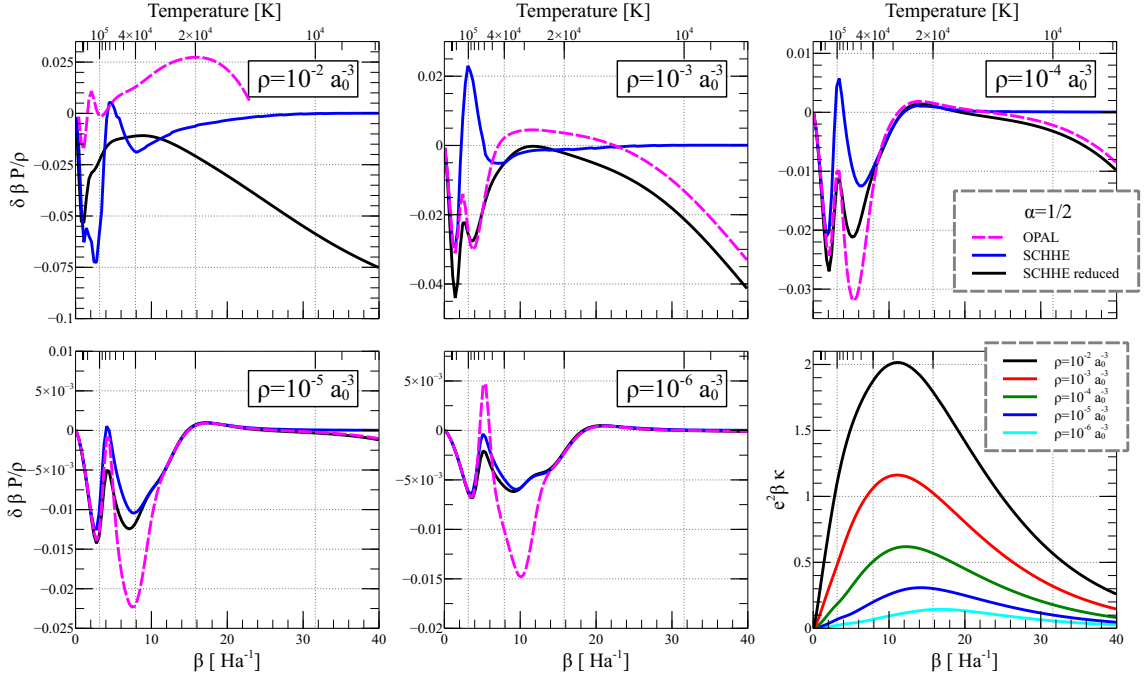


Figure 7.8: The differences with respect to the Saha equation are shown for the three equations of state. For $\rho = 10^{-6} a_0^{-3}$ the OPAL-prediction shows a large variation around $\beta = 8 \text{Ha}^{-1}$. Since for low densities long-range effect reduce essentially to the Debye correction and the κ -dependence of the cluster functions is less important, we believe that, again the He^+ contribution to screening can be responsible for the deviation for $\beta > 8 \text{Ha}^{-1}$. The larger pressure predicted by the OPAL-table for $\beta < 8 \text{Ha}^{-1}$ cannot be related to this He^+ screening since it will lower the pressure. For reasonable densities the models are indistinguishable in the low and high-temperature regime.

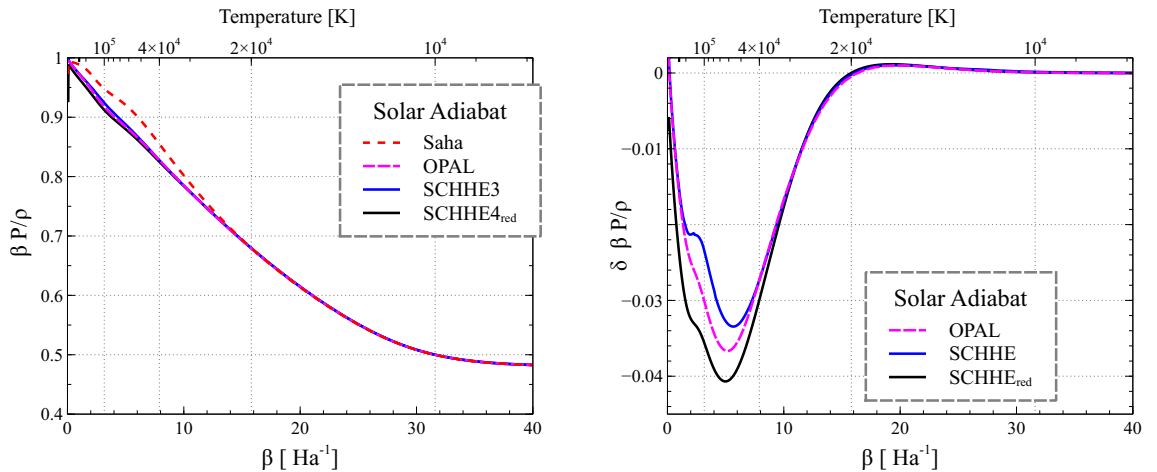


Figure 7.9: Our prediction along the adiabat of the Sun. The differences of our full model SCHHE and the OPAL-tables are always smaller than 0.1%. Only in the intermediate-temperature regime differences of the three models can be found. We will see in the following chapter that part of the deviation is related to the He^+ -contribution to the screening process.

resummation process $\tilde{z}_{\text{He}^+} = \tilde{z}_e \tilde{z}_\alpha C_{\text{He}^+}(\beta, \kappa)$. The effective charge of this “particle” can be determined by summing up all fundamental diagrams arising during the chain resummation

He^+ He^+ He^+ He^+

α α α α

e e e e

e^2 $-2e^2$ $-2e^2$ $4e^2$

(7.18)

which leads to an effective charge $e_{\text{He}^+} = 4e - 2e - 2e + 1e = 1e$ equal to the overall charge of He^+ , as expected. The screening constant, therefore, fulfills through

$$\kappa = \sqrt{4\pi\beta \sum_{\gamma=\{e,p,\alpha,\text{He}^+\}} e_\gamma^2 z_\gamma}. \quad (7.19)$$

a self-consistency equation due to the κ -dependence of the effective fugacity $z_{\text{He}^+} = z_e z_\alpha C_{\text{He}^+}(\beta, \kappa)$ of the He^+ -cluster⁷. The inclusion of the He^+ cluster in the screening process gives also rise to changed diagrammatic rules: The He^+ cluster is treated like an additional fundamental particle and, thus, no convolutions involving this cluster are present in the new diagrammatic.

We have decided not to solve the self-consistency equation (7.20), but to iterate it to first order in z_{He^+}

$$\kappa = \sqrt{4\pi\beta \left(\sum_{\gamma=\{e,p,\alpha\}} e_\gamma^2 z_\gamma \right) + e^2 z_e z_\alpha C_{\text{He}^+}(\beta, \kappa_0)}, \quad (7.20)$$

where $\kappa_0 = \sqrt{4\pi\beta(z_e + z_p + 4z_\alpha)}$ is the screening constant for which the He^+ -cluster has not been taken into account. This approximation is justified due to the weak dependence of the cluster functions on the screening constant⁸.

The results of this model involving He^+ -screening are shown in figure 7.10 for $\alpha = 1/4$. For comparison we show again the OPAL-prediction as well as our results where the He^+ -cluster has not been taken into account during the screening process. Alongside the difference of the charge-charge coupling $e^2\beta(\kappa_{\text{He}^+} - \kappa_0)$ is shown. As expected the screening constant κ_{He^+} became larger by taking the He^+ -particles into consideration. By taking the He^+ screening into account the accordance with the OPAL-tables is even better, at least for low densities. The screening provided by the He^+ -particles slightly reduced the pressure in the recombination domain $\beta < 10\text{Ha}^{-1}$. To round up our study, we present our last plot where the predictions of the SCHHE_{He⁺} model for the pressure along the adiabat of the Sun are shown again.

The inclusion of the He^+ particles in the screening process leads to a better accordance with the OPAL-predictions and a small pressure decrease in the intermediate-temperature regime. All three models are showing for about $\beta = 2\text{Ha}^{-1}$ a change of behavior. The “unnatural” behavior of the SCHHE model is partly cured when allowing for screening by He^+ -particles. For temperatures of about $\beta = 7\text{Ha}^{-1}$ our SCHHE_{He⁺} model recovers the OPAL prediction, whereas this happens only at about $\beta = 8\text{Ha}^{-1}$

⁷The cluster function is given by $C_{\text{He}^+} = \textcircled{e, \alpha}$ where the internal fugacity factors are dressed by attached rings.

⁸We have verified that the next order iteration of the self-consistency equation (equation (7.20)) does not change the results for the equation of state for the parameter range of ρ, α we are interested in.

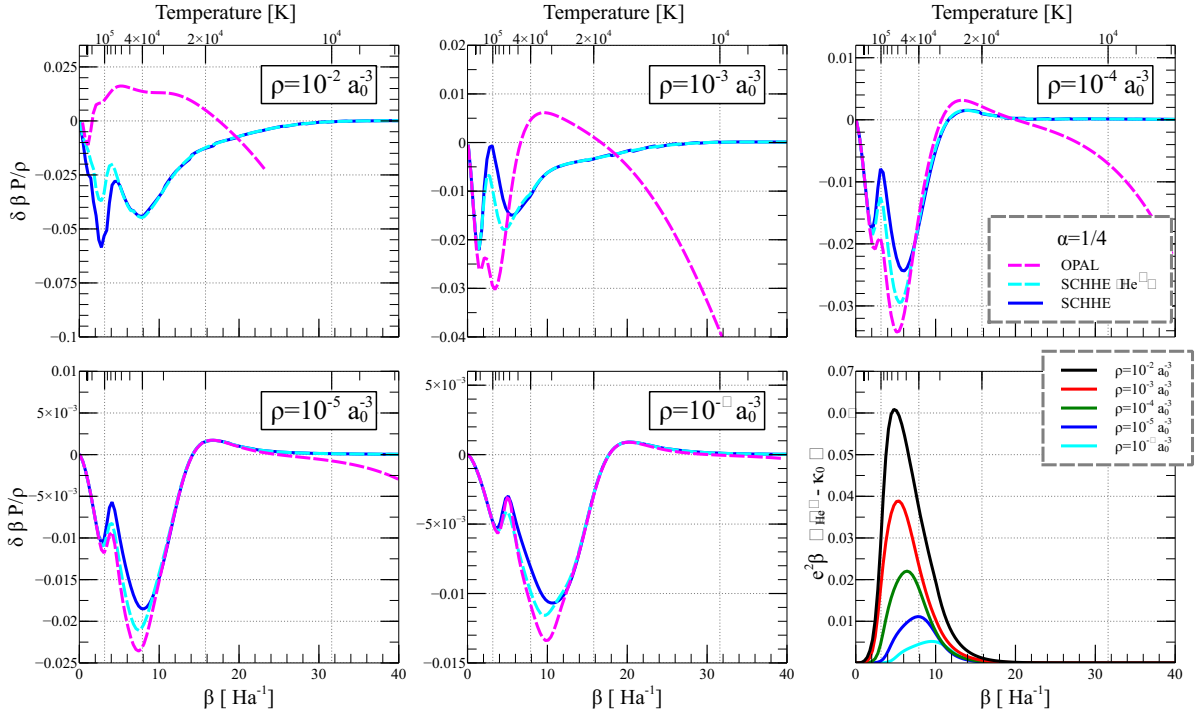


Figure 7.10: The prediction of our He^+ screening model in comparison to the one without He^+ screening and the OPAL-tables. Alongside the difference of the bare screening constant κ_0 and the He^+ version κ_{He^+} is shown. As expected the screening constant $\kappa_{\text{He}^+} > \kappa_0$ and thereby the weight of the Debye-type SLR-diagrams has increased, which leads to a pressure decrease, so that our predictions become closer to the OPAL-predictions. Again, for high densities the κ -dependence of the cluster functions gains importance and we attribute the differences to this.

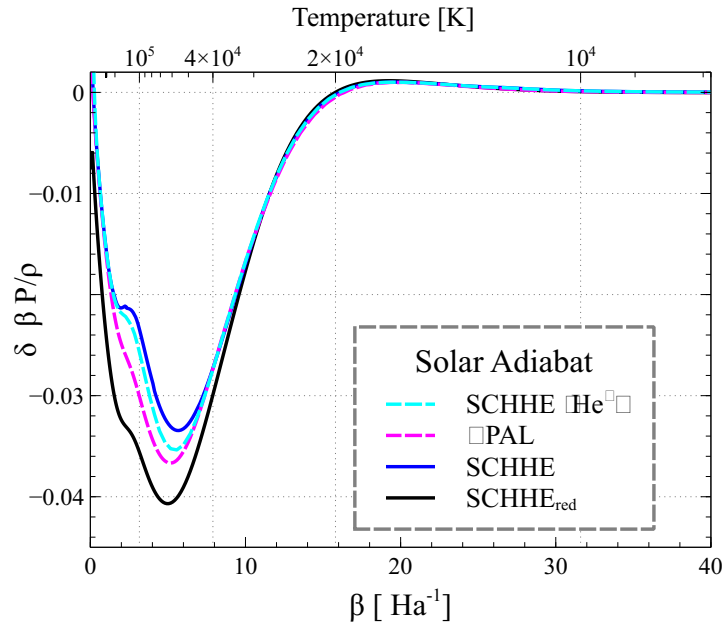


Figure 7.11: Our predictions along the solar adiabat. The He^+ screening leads to a small decrease of the pressure (in the direction of the OPAL prediction) in the intermediate-temperature regime. For higher or smaller temperatures the models are indistinguishable.

for the SCHHE model. We insist on the fact that our $\text{SCHHE}_{\text{He}^+}$ model consistently accounts for the screening effects of the He^+ -particles, due to the fact that we derived the model by exact diagrammatic considerations.

7.5 Conclusion

In this chapter we have in depth analyzed the pure Hydrogen system as well as the Hydrogen-Helium mixture using our numerically calculated cluster functions. The accordance with the OPAL-tables is striking for a very large parameter regime. Differences are confined to intermediate temperatures, where the particles recombine as well as to high densities. For the considered densities ($\rho^{-2}a_0^{-3} < 10^{-2}$), we found no sign of pressure ionization. Our numerically calculated cluster function indeed tend to zero if the screening constant becomes large⁹. This decrease of the cluster function is, on the other hand, canceled by the growing weight of the attached loops, so that the overall contribution of a certain particle cluster even increases (see the plots of the κ -dependent cluster functions in section §5.4). Therefore, we argue that even though the ground state of the particle cluster is destroyed for large densities, this does not necessarily mean that the pressure increases. We remark that the here shown approach to the partially ionized gas is in principle well suited to study the problem of pressure ionization, but such a study would require the inclusion of far more terms in the diagrammatic series.

We have implemented the He^+ screening process on the level of diagrams, where we assumed a scale separation $\kappa a^{\text{He}^+} < 1$ of the screening length scale and the natural length scale a^{He^+} of the He^+ cluster (for low temperatures $a^{\text{He}^+} \rightarrow a_0^{\text{He}^+}$ this scale becomes the scale of the ground state). Our models predicted in most of the cases a larger pressure than the OPAL-tables. A conclusion of the here presented analysis is that the Sun is an almost ideal system. For solar conditions, deviations from the Saha equation are small and mostly given by the famous Debye term. Three particle clusters and the κ -dependence of the cluster functions only lead to a small change of the pressure. Nevertheless, helioseismic observations claim are said to be sensitive to such small deviations [72]. A comparison with experimental data would be very interesting and could give further insights about the “physics” of the Sun.

⁹The cluster functions shown in section §5.4 were dressed by attached rings, the bare cluster functions tend to zero as κ increases

Chapter 8

Conclusions

In this thesis we have considered the Hydrogen-Helium mixture in the physical picture. Our results confirm the predictions of the OPAL-tables for a large range of parameters and especially for the adiabat of the Sun. Nevertheless, our precise formulation of the equation of state, where all approximations are visible and controlled, is a major advance with respect to the phenomenological proprietary OPAL-code. The high precision currently achievable by helioseismic measurements would presumably make it possible to discriminate between these two models, but for the lack of time we were not able to carry out this analysis. This comparison to experimental data is one of the first future prospects and important to quantify the quality of our equation of state. Furthermore, for high densities $10^{-2} < \rho a_0^3 < 10^{-4}$ and intermediate temperature $T \sim 4 \cdot 10^4 K$ deviations between the two models have actually an important magnitude. These differences can be traced back to the dependence of the cluster functions on the screening constant κ , a physical feature which is correctly taken into account within our formalism.

During the preparation of this thesis we tackled and overcame various numerical and analytical problems. On the analytical side, we first have shown that the Screened Cluster Representation (SCR) for the particle densities [34] can be reformulated for the pressure. This new diagrammatic series for the pressure recovers the SCR for the densities by applying standard thermodynamical identities, as it should. This formulation simplifies the calculations and directly provides the equation of state. As quoted in Ref. [34] the contributions of the chemical species can be naturally associated with diagrams involving particle clusters. The new diagrammatic series for the pressure achieved a transparent, numerically exploitable, “modularization” of the equation of state, a feature that is often attributed to the chemical picture. We have used the new formulation in combination with the numerically calculated cluster functions to take all chemical species with up to three particles into account in a consistent manner. Furthermore, this work showed how the contribution of ions, in particular He^+ , can be implemented consistently on the level of diagrams.

The central object in the resummed diagrammatic is the screened loop-loop potential, which turns out to be a rather complicated object. At the pragmatic level, we derived a very simple semi-classical approximation of this potential, which is sufficiently accurate at low temperatures. This simplified screened potential properly accounts for the collective effects in the internal partition functions of the particle clusters. We stress that the ad-hoc inclusion of such effects within the chemical picture is plagued with ambiguities and double-counting problems. Furthermore, we have opened up a way to take the full time dependence of the resummed loop-loop potential into account. This can be achieved by solving a self-consistency equation and will be of importance for the equation of state if the screening length becomes

comparable to the thermal wavelength $\kappa \lambda \sim 1$. The self-consistency equation is easily exploitable numerically and will, in contrast to our simple approximation, provide a more reliable inter-loop potential for dense conditions.

As far as the numerical difficulties we were facing are concerned, two important obstacles have to be mentioned: The singularity of the Coulomb potential at the origin and the formation of bound states at low temperatures. The first point gave rise to an adaptive discretization algorithm that does neither rely on the commonly used pair-action approximation nor on the exact two-body density matrix. This approach takes all correlations between the paths into account in a coherent way, and enables us to carry out “discretization independent” path integral calculations. The Importance sampling function introduced to capture the formation of bound states at low temperature has proven to be very appropriate. Usually such a direct sampling approach is not necessary. We have directly calculated partition functions involving a complicated truncation originating from the resummation of chain-diagrams. The Metropolis-Hastings algorithm was not applicable to this problem without major complications. After the preparation of this thesis we became aware of the work of Ref. [60], which uses a very similar approach for the calculation of real-time matrix elements. The Monte-Carlo techniques developed in this thesis should enable us to calculate the internal partition function of four particle cluster, so that the way for a coherent implementation of Hydrogen molecules in the equation of state of the Hydrogen-Helium mixture is paved.

In retrospective, we believe that we have concentrated too much of our effort to low temperatures. From almost all of our plots of the equation of state the reader will quickly recognize that the “physics”, beyond the mixture of ideal gases, actually take place at about $\beta < 15 \text{ Ha}^{-1}$ ($T > 2 \cdot 10^4 \text{ K}$) and $\rho a_0 > 10^{-4}$. For these temperatures our algorithm gives very precise results and the incorporation of the time-resolved loop-loop potential would have been in reach. It is also in this temperature regime that the three-body cluster functions that we have calculated numerically gives at least some significant contribution. We believe, therefore, that the study of this intermediate temperature-density regime will be most fruitful for further research. In this region the partially ionized plasma is far from ideal and charge-charge, charge-atom, and higher order clusters are of paramount importance, since the screening constant κ is not small and the intermediate temperature β does neither favor free particles nor atoms.

We hope that the work presented in this thesis will stimulate further research in the various related fields.

Bibliography

- [1] I. Newton. *Philosophiae naturalis principia mathematica*. J. Societatis Regiae ac Typis J. Streater, 1687.
- [2] D. Walsh, R. F. Carswell, and R. J. Weymann. 0957 + 561 a, b: twin quasistellar objects or gravitational lens? *Nature*, 279(5712):381–384, May 1979.
- [3] Bruce T. Cleveland et al. Measurement of the solar electron neutrino flux with the homestake chlorine detector. *Astrophys. J.*, 496:505–526, 1998.
- [4] V. Gribov and B. Pontecorvo. Neutrino astronomy and lepton charge. *Physics Letters B*, 28(7):493–496, 1969.
- [5] C. W. Walter. The Super-Kamiokande Experiment. *ArXiv e-prints*, February 2008.
- [6] L. D. Landau and E.M. Lifshitz. *Quantum Mechanics: Non-Relativistic Theory*, volume 3. Pergamon Press, 1958.
- [7] M. N. Saha. Liii. ionization in the solar chromosphere. *Philosophical Magazine Series 6*, 40(238):472–488, 1920.
- [8] M. N. Saha. On a physical theory of stellar spectra. *Proceedings of the Royal Society of London A: Mathematical, Physical and Engineering Sciences*, 99(697):135–153, 1921.
- [9] V. Ballenegger. The divergent atomic partition function or how to assign correct statistical weights to bound states. *Ann. Phys.*, 524(6-7):103–105, Jul 2012.
- [10] C. Fefferman. The atomic and molecular nature of matter. *Rev. Math. Iberoamericana 1:1-44*, (1985).
- [11] J. L. Lebowitz and Elliott H. Lieb. Existence of thermodynamics for real matter with coulomb forces. *Phys. Rev. Lett.*, 22:631–634, Mar 1969.
- [12] D. Wendland, V. Ballenegger, and A. Alastuey. Quantum partition functions of composite particles in a hydrogen-helium plasma via path integral monte carlo. *The Journal of Chemical Physics*, 141(18), 2014.
- [13] A. Alastuey, V. Ballenegger, F. Cornu, and P. A. Martin. Exact results for thermodynamics of the hydrogen plasma: Low-temperature expansions beyond saha theory. *J. Stat. Phys.*, 130(6):1119–1176, Mar 2008.
- [14] A. Alastuey and V. Ballenegger. Thermodynamics of atomic and ionized hydrogen: Analytical results versus equation-of-state tables and monte carlo data. *Phys. Rev. E*, 86(5):066402, Dec 2012.

- [15] G. M. Harris, J. E. Roberts, and J. G. Trulio. Equilibrium Properties of a Partially Ionized Plasma. *Physical Review*, 119:1832–1841, September 1960.
- [16] H. C. Graboske, D. J. Harwood, and F. J. Rogers. Thermodynamic properties of nonideal gases. i. free-energy minimization method. *Phys. Rev.*, 186:210–225, Oct 1969.
- [17] A. I. Larkin. *Sov. Phys. - JETP*, 11:1363, 1960.
- [18] D. Mihalas, W. Däppen, and D. G. Hummer. The equation of state for stellar envelopes. II - Algorithm and selected results. *The Astrophysical Journal*, 331:815–825, August 1988.
- [19] Didier Saumon and Gilles Chabrier. Fluid hydrogen at high density: Pressure dissociation. *Phys. Rev. A*, 44:5122–5141, Oct 1991.
- [20] Didier Saumon and Gilles Chabrier. Fluid hydrogen at high density: Pressure ionization. *Phys. Rev. A*, 46:2084–2100, Aug 1992.
- [21] C. A. Rouse. Comments on the Planck-Larkin partition function. *The Astrophysical Journal*.
- [22] F. J. Rogers. Equation of state of dense, partially degenerate, reacting plasmas. *Phys. Rev. A*, 24:1531–1543, Sep 1981.
- [23] F. J. Rogers and A. Nayfonov. Updated and expanded opal equation-of-state tables: Implications for helioseismology. *The Astrophysical Journal*, 576(2):1064, 2002.
- [24] W. Ebeling. Statistische Thermodynamik der gebundenen Zustände in Plasmen. *Ann. Phys.*, 19:104, 1967.
- [25] A Alastuey and A Perez. Virial expansion of the equation of state of a quantum plasma. *Europhys. Lett.*, 20(1):19–24, 1992.
- [26] Angel Alastuey, Françoise Cornu, and Asher Perez. Virial expansions for quantum plasmas: Diagrammatic resummations. *Phys. Rev. E*, 49:1077–1093, Feb 1994.
- [27] A Alastuey and A Perez. Virial expansions for quantum plasmas: Fermi-Bose statistics. *Phys. Rev. E*, 53(6, Part a):5714–5728, 1996.
- [28] T. Kahlbaum. The quantum-diffraction term in the free energy for Coulomb plasma and the effective-potential approach. *J. Phys. IV*, 10(P5):455–459, 2000. International Conference on Strongly Coupled Coulomb Systems, ST MALO, FRANCE, SEP 04-10, 1999.
- [29] Lowell S. Brown and Laurence G. Yaffe. Effective field theory for highly ionized plasmas. *Physics Reports*, 340(12):1 – 164, 2001.
- [30] T. Morita. Equation of state of high temperature plasma. *Prog. Theor. Phys*, 22:757, 1959.
- [31] F. J. Rogers, F. J. Swenson, and C. A. Iglesias. OPAL Equation-of-State Tables for Astrophysical Applications. *The Astrophysical Journal*, 456:902, January 1996.
- [32] Hsiao-Hsuan Lin and Werner Däppen. Emulating the opal equation of state. *Astrophysics and Space Science*, 328(1-2):175–178, 2010.
- [33] Hsiao-Hsuan Lin. *Modeling the hot-dense plasma of the solar interior in and out of thermal equilibrium*. PhD thesis, Faculty of the USC graduate school university of Southern California, 2012.

-
- [34] A. Alastuey, V. Ballenegger, F. Cornu, and P. A. Martin. Screened cluster expansions for partially ionized gases. *J. Stat. Phys.*, 113(3-4):455–503, Nov 2003.
- [35] Joseph E. Mayer. The theory of ionic solutions. *The Journal of Chemical Physics*, 18(11):1426–1436, 1950.
- [36] N. Macris and Ph.A. Martin. Ionization equilibrium in the electron-proton gas. *Journal of Statistical Physics*, 60(5-6):619–637, 1990.
- [37] A. Alastuey and V. Ballenegger. Pressure of a partially ionized hydrogen gas: Numerical results from exact low temperature expansions. *Contrib. Plasm. Phys.*, 50(1):46–53, Jan 2010.
- [38] D. M. Ceperley. Path-integrals in the theory of condensed helium. *Rev. Mod. Phys.*, 67(2):279–355, 1995.
- [39] C. Pierleoni, D. M. Ceperley, B. Bernu, and W. R. Magro. Equation of state of the hydrogen plasma by path integral monte carlo simulation. *Phys. Rev. Lett.*, 73:2145–2149, Oct 1994.
- [40] B. Militzer and D. M. Ceperley. Path integral monte carlo simulation of the low-density hydrogen plasma. *Phys. Rev. E*, 63:066404, May 2001.
- [41] B. Militzer, W. Magro, and D. Ceperley. Characterization of the state of hydrogen at high temperature and density. *Contributions to Plasma Physics*, 39(1-2):151–154, 1999.
- [42] François Soubiran. *Dense plasma physics: The hydrogen-helium mixtures in planetary interiors*. Theses, Ecole normale supérieure de lyon - ENS LYON, October 2012.
- [43] RP Feynman and AR Hibbs. *Quantum mechanics and path integration*. McGraw–Hill, 1965.
- [44] E. L. Pollock and D. M. Ceperley. Path-integral computation of superfluid densities. *Phys. Rev. B*, 36:8343–8352, Dec 1987.
- [45] D. M. Ceperley and E. L. Pollock. Path-integral computation techniques for superfluid 4he. In *Proceedings of the Elba Conference on Monte Carlo Methods in Theoretical Physics*, page 35, 1990.
- [46] D. C. Brydges and P. A. Martin. Coulomb systems at low density: A review. *J. Stat. Phys.*, 96(5-6):1163–1330, 1999.
- [47] F. Cornu. Correlations in quantum plasmas. i. resummations in mayer-like diagrammatics. *Phys. Rev. E*, 53:4562–4594, May 1996.
- [48] E. E. Salpeter. On Mayer’s theory of cluster expansions. *Annals of Physics*, 5:183–223, November 1958.
- [49] Ian R. McDonald Jean-Pierre Hansen. *Theory of Simple Liquids*. Academic Press, 2006.
- [50] V. Ballenegger, P. A. Martin, and A. Alastuey. Quantum mayer graphs for coulomb systems and the analog of the debye potential. *J. Stat. Phys.*, 108(1-2):169–211, Jul 2002.
- [51] D. G. Hummer and D. Mihalas. The equation of state for stellar envelopes. I - an occupation probability formalism for the truncation of internal partition functions. *The Astrophysical Journal*, 331:794–814, August 1988.

- [52] A. Alastuey and Ph A. Martin. Absence of exponential clustering for the static quantum correlations and the time-displaced correlations in charged fluids. *EPL (Europhysics Letters)*, 6(5):385, 1988.
- [53] A. Alastuey and Ph. A. Martin. Absence of exponential clustering in quantum coulomb fluids. *Phys. Rev. A*, 40:6485–6520, Dec 1989.
- [54] W. Ebeling. Zur Quantenstatistik der Bindungszustände in Plasmen. I Cluster-Entwicklungen. *Annalen der Physik*, 477(7-8):383–391, 1969.
- [55] W. Ebeling. Zur Quantenstatistik der Bindungszustände in Plasmen. II Berechnung der Cluster-Integrale. *Ann. Phys.*, 22:392, 1969.
- [56] M. Takahashi and M. Imada. Monte Carlo Calculation of Quantum Systems. II. Higher Order Correction. *Journal of the Physical Society of Japan*, 53:3765, November 1984.
- [57] J. S. Kole and H. De Raedt. Quantum Monte Carlo method for attractive Coulomb potentials. *Phys. Rev. E*, 64(1, 2), JUL 2001.
- [58] C. Predescu. Highly optimized fourth-order short-time approximation for path integrals. *J. Phys. Chem. B*, 110:667, 2006.
- [59] N. Metropolis, A. W. Rosenbluth, M. N. Rosenbluth, A. H. Teller, and E. Teller. Equation of State Calculations by Fast Computing Machines. *The Journal of Chemical Physics*, 21:1087–1092, June 1953.
- [60] Ilkka Ruokosenmki and Tapio T. Rantala. Numerical path integral approach to quantum dynamics and stationary quantum states. *Communications in Computational Physics*, 18:91–103, 7 2015.
- [61] H. Kleinert. *Path Integrals in Quantum Mechanics, Statistics, Polymer Physics, and Financial Markets*. World Scientific, Singapore, 5th ed. edition, 2009.
- [62] W. Krauth. *Statistical Mechanics: algorithms and computations*. Oxford University Press, 2006.
- [63] Antonín Slavík. *Product integration, its history and applications*. Matfyzpress Prague, 2007.
- [64] I.H. Duru and H. Kleinert. Solution of the path integral for the H-atom. *Physics Letters B*, 84(2):185 – 188, 1979.
- [65] S. M. Blinder. Canonical partition function for the hydrogen atom via the coulomb propagator. *Journal of Mathematical Physics*, 36(3):1208–1216, 1995.
- [66] E.L. Pollock. Properties and computation of the coulomb pair density matrix. *Computer Physics Communications*, 52(1):49 – 60, 1988.
- [67] P. Vieillefosse. Coulomb pair density matrix i. *Journal of Statistical Physics*, 74(5-6):1195–1209, 1994.
- [68] P. Vieillefosse. Coulomb pair density matrix. ii. *Journal of Statistical Physics*, 80(1-2):461–479, 1995.
- [69] P. C. Stancil. Partition functions and dissociation equilibrium constants for H_2^+ and He_2^+ . *J. Quant. Spectrosc. Radiat. Transfer*, 51:655–658, 1994.

- [70] J. Christensen-Dalsgaard, W. Däppen, S. V. Ajukov, E. R. Anderson, H. M. Antia, S. Basu, V. A. Baturin, G. Berthomieu, B. Chaboyer, S. M. Chitre, A. N. Cox, P. Demarque, J. Donatowicz, W. A. Dziembowski, M. Gabriel, D. O. Gough, D. B. Guenther, J. A. Guzik, J. W. Harvey, F. Hill, G. Houdek, C. A. Iglesias, A. G. Kosovichev, J. W. Leibacher, P. Morel, C. R. Proffitt, J. Provost, J. Reiter, E. J. Rhodes, F. J. Rogers, I. W. Roxburgh, M. J. Thompson, and R. K. Ulrich. The current state of solar modeling. *Science*, 272(5266):1286–1292, 1996.
- [71] S. Basu and J. Christensen-Dalsgaard. Equation of state and helioseismic inversions. *Astronomy and Astrophysics*, 322:L5–L8, June 1997.
- [72] MariaPia Di Mauro. Helioseismology: A fantastic tool to probe the interior of the sun. In JeanPierre Rozelot, editor, *The Suns Surface and Subsurface*, volume 599 of *Lecture Notes in Physics*, pages 31–67. Springer Berlin Heidelberg, 2003.